ANALYTICAL AND EXPERIMENTAL STUDIES OF THERMIONICALLY EMITTING ELECTRODES IN CONTACT WITH DENSE, SEEDED PLASMAS

Thesis by

John Kent Koester

In Partial Fulfillment of the Requirements
For the Degree of
Doctor of Philosophy

California Institute of Technology
Pasadena, California
1970

(Submitted December 4, 1969)

ACKNOWLEDGMENTS

The author wishes to express his sincere appreciation to his thesis advisor, Professor E. E. Zukoski, for his guidance and encouragement during the course of this investigation. Special thanks are also extended to Professor M. Sajben for his enlightening discussions concerning this work.

Appreciation is expressed to Drs. A. C. Pinchak, T. A. Cool, and R. R. Gilpin for their previous work on the plasma-arc facility which provided many techniques and results used here.

My sincerest thanks to Mr. Frank T. Linton for his work in the fabrication of the test equipment and in the drawing of the figures for this thesis. The author also thanks Mrs. Roberta Duffy for her assistance in preparing the typed manuscript.

The National Science Foundation is acknowledged for their financial assistance to the author while at this Institute.

Finally, the author expresses his deep gratitude to his parents, Mr. and Mrs. John Ross Koester, for their constant moral and financial support of this long collegiate career.

ABSTRACT

The electrode current-voltage characteristics and the limiting cathode current density for thermionically emitting electrodes in contact with high-pressure, seeded, non-equilibrium MHD plasmas were determined analytically and experimentally. The theoretical model was based on the coupling of the adsorption phenomena of alkali metal seed particles onto electrode surfaces with that behavior due to the plasma in the electric boundary layer adjacent to the electrode surface. The desorption rates of electrons and seed atoms and ions (which were given by quoted functions of the surface temperature, the surface degree of coverage, and the electric field at the surface) were related to the appropriate boundary conditions for the governing continuum-type plasma equations in the electric boundary layer.

An algorithm was given for the simultaneous solutions of both the surface state and the electric boundary layer. Machine computed results were presented for a potassium-seeded argon plasma (at 2000^{o}K and one atmosphere pressure) in axially-symmetric stagnation flow over a tungsten electrode and displayed the effects of varying the parameters: surface temperature and seed fraction. These results indicated an order of magnitude increase in the thermionic limiting current density due to coupling effects.

Experimentally, the electrode phenomena were studied in a non-equilibrium discharge produced in the same plasma-electrode system as used for the machine computations. The electrode behavior was determined from voltage probes, photomultiplier measurements, and photographs. As the thermionic limit was approached, a transition to an arc mode of cathode operation occurred at some breakdown voltage drop. The experimental current-voltage characteristics for the cathode agreed with the machine results,and the predicted enhancement of the thermionic limiting current density was observed experimentally.

TABLE OF CONTENTS

I. INTRODUCTION

High pressure (atmospheric), alkali metal-seeded plasmas are of considerable engineering importance, since the low ionization potential of the alkali seed enables a reasonably high electrical conductivity to be attained at modest gas temperatures. These modest gas temperatures allow the containment of the plasma in a device that is either cooled externally or constructed from refractory materials. Possible practical applications of this type of plasma include the direct conversion of heat into electrical energy by a magnetohydrodynamic (MHD) generator and the MHD accelerator which transforms electrical energy into kinetic energy.

Since direct current MHD devices are connected to external circuits which conduct electricity by an electron current, one electrode (the cathode) must liberate this electron current while the other (the anode) collects it in order to complete the circuit through the plasma. Usually, the electron current liberated at the cathode is limited, and when this limit is attained, a voltage increase across the device cannot increase the current through the system: the extra voltage appears as a voltage drop in a region adjacent to the cathode.

The electrons are liberated at the cathode by 1) emission by some process (thermionic, field, photoelectric, etc.) as a free electron, and 2) by recombination with an ion at the cathode surface. As the mobility of electrons is far greater than that of the ions in the bulk plasma (on the order of $\sqrt{m_i/m_e}$), the emission mechanism dominates the recombination mechanism unless there is substantial ionization adjacent to the cathode. It is well known(6) that the alkali metal seed material reacts chemically with the cathode surface to form an adsorbed layer. This layer reduces the effective work function of the surface, which allows electrons to escape through the surface barrier by thermionic emission at a greatly enhanced rate. This effect allows the possibility of operating MHD electrodes in a thermionic mode as opposed to some arc type of mode. The thermionic mode of operation allows lower cathode voltage drops than the arc mode does because the extra energy for the increased ionization and the greater local heating required to maintain an arcspot is not necessary for the thermionic mode. The low electrode drops are important to many MHD devices,for this increases the electrical efficiency, reduces the heat loss to the walls, and slows down the erosion of the walls of such devices.

The purpose of this investigation is to study the thermionic mode of electrode operation to determine what electrode voltage drops occur and the limiting electrode current densities that take place in the thermionic mode. The first part of this work is analytical and provides a theoretical model with no adjustable parameters that describes the thermionic mode. This model treats the ionized gas as a continuum, due to its high pressure. One of the major accomplishments of the present model is the integration of the adsorption phenomena with the plasma. This integration is executed by accounting for the fluxes of seed atoms and ions and by relating these fluxes to the state of the electrode surface. The integrated theory relies on the earlier work of Levine and Gyftopoulos(7-10) on the adsorption process to connect the state of the electrode surface to the emitted fluxes of electrons, ions, and atoms. These emitted fluxes are related to the number densities of the various species at the surface so that the appropriate continuum boundary conditions for the plasma problem are specified.

The plasma problem is solved by asymptotic techniques developed for continuum probe theory by Cohen(18), Lam(19), Bienkowski(12), and others. This technique is extended in the present work to include the effects of production, large rates of surface emission, and variable transport coefficients. An iterative method is developed for solving the coupled surface - plasma problem.

The important regions of the problem are sketched in Figure 1. Between the flowing bulk plasma and the electrode surface is an electric boundary layer across which the electrode voltage drop occurs. The thickness of this region depends on the scaling parameter, δ, defined in Section 2.5. Immediately adjacent to the electrode surface is a thin Knudsen layer on the order of a mean free path in thickness. The non-continuum effects which occur across this layer relax the two-sided nature of the distribution function of the emitted particles to a near-equilibrium type in the continuum region. At the electrode edge of the continuum region lies an electrostatic sheath of thickness related to the Debye length.

The large electric fields that build up in the sheath region, due to charge separation, affect the emission of charged particles from the surface. This electric field influence is accounted for by the Schottky correction term to the work function of the surface.

The present model includes non-equilibrium effects by treating the bulk plasma region by the two-temperature model studied by Kerrebrock(2) and Cool(1). Suggestions for important future extensions of the present theory include the effect of magnetic field, the variation of electron temperature in the electric boundary layer, and non-continuum sheath effects.

The second part of this work is experimental, and verifies the predictions of the model that surprisingly large thermionic currents are possible under certain conditions on electrode surface temperature and seed fraction.

II. THEORY OF ELECTRODE - SEEDED PLASMA INTERACTION

In this part of the thesis, the theory of the electrode - seeded plasma interaction will be developed. First, the basic assumptions will be listed and the basic equations that describe the plasma in continuum terms will be presented, along with the kinetic theory expression for the transport coefficients. Next, the basic surface physics of a refractory metal electrode covered by monatomic metallic particles will be discussed. Then, the surface conditions will be related to the number densities of various particles at the electrode and the state of the surface will be connected to the plasma problem.

The asymptotic method of solving the plasma equations will be presented. Finally, the theory will be applied to an electrode in stagnation flow, and computer solutions for a potassium-seeded argon plasma with a tungsten electrode will be discussed.

2.1 Basic Assumptions

The present theory is formulated under the following assumptions:

1) The charged-neutral mean free paths are assumed small compared to the characteristic electrode dimension (L), and also small compared to the thickness of the sheath adjacent to the electrode. The Debye length is small compared to L. This is the continuum assumption, which restricts any non-continuum effects to a thin Knudsen-like layer immediately next to the electrode surface.

2) The ions and neutrals are assumed to be in translational equilibrium at the neutral temperature, T_n, and the electrons and

excited states are in thermal equilibrium at a different temperature, the electron temperature, T_e. This two-temperature model has been found(1, 2) to adequately describe the type of plasma considered here. The energy equation is only used in the bulk plasma, and the resulting electron temperature is assumed constant throughout the bulk plasma and the electric boundary layer; this assumption is justified in Appendix A.

3) The degree of ionization is small, so that electrohydrodynamic interactions are neglected. This assumption allows us to assume that the neutral velocity field is known. The Mach number of the flow is small, so that the flow can be assumed incompressible.

4) The electric fields are assumed moderate, so that ion and electron particle fluxes can be described in terms of field-independent transport coefficients and the corresponding gradients.

5) The plasma is in steady state. There is no applied magnetic field, and induced magnetic fields are neglected.

6) Three-body recombination is assumed to be the dominant recombination mechanism. Only thermal ionization is included, and ionization due to electrons accelerated by the high voltage sheath is not considered.

7) The presence of an inert carrier gas is assumed not to affect the surface physics of the alkali seed - electrode interaction. The surface diffusion flux of adsorbed particles is negligible compared to their evaporation rate.

2. 2 Basic Plasma Equations

The equations that govern the ionized gas phase throughout the bulk plasma and the electric boundary layer are the following (expressed in the charge-rationalized MKS system of units):

Poisson's Equation

$$\epsilon_o \nabla^2 \phi = -e(n_i - n_e) \tag{1}$$

where we consider the positive ions to be singly ionized.

Conservation of Species

$$\vec{u} \cdot \nabla n_s + \nabla \cdot \vec{\Gamma}_s = \dot{n}_s \qquad s = i, e, a \tag{2}$$

where $\vec{u}$ is the known viscous, incompressible, neutral flow field, $\vec{\Gamma}_s$ is the flux of the s species, and $\dot{n}_s$ is the net production rate.

Particle Flux Equation. Conservation of momentum is accounted for by the particle flux equation:

$$\vec{\Gamma}_s = -D_s \left(\nabla n_s + \frac{q_s}{kT_s} n_s \nabla \phi \right) \tag{3}$$

where $q_i = e$, $q_e = -e$, and $q_a = 0$. The mobilities have been related to the diffusion coefficients by Einstein's relation.

Electron Energy Equation. The energy balance equation for electrons is$^{(2)}$:

$$\vec{u} \cdot \nabla \left[n_e \left(\frac{3}{2} kT_e + V_i \right) \right] + \nabla \cdot \vec{q}_e - \vec{j}_e \cdot \vec{E} = -\dot{\Omega} - \dot{R} \tag{4}$$

where $\dot{\Omega}$ is the rate of elastic energy loss per unit volume from free electrons, $\dot{R}$ is the radiation loss per unit volume due to inelastic electronic collisions; $\vec{E} = -\nabla\phi$, $\vec{j}_e = -e\vec{\Gamma}_e$, $\vec{q}_e = -\lambda \nabla T_e - \frac{\vec{j}_e}{e}\left[\frac{5}{2}kT_e + V_i\right]$, and the convention of measuring the energy of the free electrons relative to the ground electronic state of the seed atom is used.

The number density of electrons is related to the electron temperature by the Saha equation, in the regions where the assumption of local thermodynamic equilibrium holds.

Saha Equation

$$n_e^2 = \left(\frac{g_e g_i}{g_a}\right)\left(\frac{2\pi m_e kT_e}{h^2}\right)^{\frac{3}{2}} n_a \exp\left(-\frac{V_i}{kT_e}\right) , \qquad (5)$$

where n_a is the number density of seed atoms. This approximate form of the Saha equation holds for $kT_e < .4$ ev.

The net volumetric production term for ions, $\dot{n}_i$, is equal to $\dot{n}_e$ since for singly ionized ions, the electrons and ions are produced or destroyed in pairs. Also, $\dot{n}_a$ is equal to $-\dot{n}_e$. For three-body recombination and electron ionization, the production term takes the form:

$$\dot{n}_e = \beta n_e - \gamma n_e^2 n_i \quad . \qquad (6)$$

The recombination coefficient, γ, is a function of the electron temperature and is evaluated theoretically by Curry (3); Cool(1) gives experimental values of γ for a potassium-seeded plasma. For thermal ionization, the ionization coefficient β is found by applying the condition of detailed balancing to equation (6), namely, setting $\dot{n}_e$ equal to zero, and relating the number densities to the electron temperature by the Saha equation. This enables the elimination of β from equation (6),and the production term becomes:

$$\dot{n}_e = \gamma(T_e) n_e [n_{Saha}^2(T_e) - n_e n_i] \quad . \qquad (7)$$

The transport coefficients are calculated as follows:

$$D_s = \frac{kT_s}{m_s \sum_{s \neq j} \nu_{sj}} \quad . \qquad (8)$$

The collision frequency for momentum transfer is evaluated for charged-neutral collisions as follows:

$$\nu_{sn} = \frac{3\pi\bar{C}_s \overline{\Sigma_n n_n Q_n^{\,s}}}{8[1 + (\sqrt{2} - 1)\delta_{si}]} \quad , \tag{9}$$

where $\delta_{ii} = 1$, $\delta_{ei} = 0$ accounts for the heavy particle persistence effect as in Cobine(4). $\bar{C}_s = 2/\sqrt{\pi}\ \sqrt{(2kT_s)/m_s}$ is the mean molecular speed, and

$$\frac{1}{\overline{\Sigma_n n_n Q_n^{\,s}}} = \int_0^\infty \frac{\xi \exp(-\xi)d\xi}{\Sigma_n n_n Q_n^{\,s}(\xi)} \quad ,$$

where $\xi = \frac{1}{2}(m_s c^2)/kT_s$. This is the same averaging method for the collision cross section as used by Cool(1).

The Spitzer collision frequencies for momentum transfer in Coulomb interactions are given below, using

$$\Lambda = \frac{12\pi(\varepsilon_o kT_e/e^2)^{3/2}}{\sqrt{n_e}} \quad :$$

$$\nu_{ei} = \frac{e^4 n_i \,\ell n\, \Lambda}{.582 \times 64 \times \sqrt{2\pi}\,\varepsilon_o^{\,2}\sqrt{m_e}\,(kT_e)^{3/2}} \tag{10}$$

$$\nu_{ee} = \frac{e^4 n_e \,\ell n\, \Lambda}{25.8\sqrt{\pi}\,\varepsilon_o^{\,2}\sqrt{m_e}\,(kT_e)^{3/2}} \tag{11}$$

$$\nu_{ie} = \frac{n_e}{n_i}\left(\frac{m_e T_i}{m_i T_e}\right)^{\frac{1}{2}} \nu_{ei} \quad . \tag{12}$$

Since $m_e/m_i << 1$, ν_{ie} is not considered in the calculation of D_i. However, ν_{ei} becomes important at the larger electron temperatures considered and is incorporated in the calculation of D_e by the following widely used(1, 2) approximate method:

$$\sum_{e \neq j} \nu_{ej} = \nu_{en} + \nu_{ei} \quad . \tag{13}$$

This gives values for D_e within 20 per cent of more elaborate techniques which are based on cross-section data which have uncertainties greater than 20 per cent.

The electronic thermal conductivity is given as in Kerrebrock(2) by:

$$\lambda = \frac{9}{4} \frac{k^2 T_e n_e}{m_e \nu_{ee}} . \tag{14}$$

2.3 Basic Surface Physics

The alkali seed particles interact strongly with the electrode because of the large affinity between the alkali metal and the electrode surface. The adsorbed alkali particles are held to the surface by partially covalent and partially ionic bonds; they can be emitted (desorbed) as ions or atoms. It is known(5) that nearly all incident seed particles are adsorbed to the surface. The adsorption of seed particles results in partial or complete coverage of the surface, even if the partial pressure of the seed is below the saturation pressure.

Since the alkali adatoms have a low electronegativity, they become positively charged with respect to the substrate (electrode) surface. This dipole field makes it easier for electrons to escape from the surface. Also, at greater than monolayer coverage, the electron emission rate becomes equal to the value for pure seed material. These two effects make the rate of electron emission strongly dependent on the degree of coverage (θ).

The above effects have been studied extensively since the pioneering work of Langmuir(6). Most of the experimental work has been done with cesium. However, a theoretical correlation by Levine and Gyftopoulos(7-10) predicts the behavior of any refractory metal partially covered by monatomic metallic particles. This theory is not derived from basic quantum mechanics principles; it is a collection of analogies with molecular physics and various models arranged to fit limiting cases of the adsorption problem. However, their theory is practical in the sense that it contains no adjustable parameters and it correlates electron emission S-curve[†] data for cesium within a factor of five over fifteen orders of magnitude of electron current density.

The necessary algebraic expressions to predict the desorption rates are quoted from the Levine and Gyftopoulos papers with the original notation usually retained. The following expressions are for a homogeneous composite surface and predict the overall effective behavior of the surface.

The effective thermionic work function (ϕ_e^*) depends on θ and the substrate-adsorbate combination. As θ varies from zero (bare substrate) to one (monolayer coverage), ϕ_e^* changes from ϕ_m (substrate work function) to ϕ_f (work function for pure adsorbate metal). The expression for ϕ_e^* is (in c. g. s. units):

$$\phi_e^*(\theta) = \phi_f + (\phi_m - \phi_f) G(\theta) \left[1 - \frac{.765 \times 10^{-14} \sigma_f \theta \cos \beta}{(1 + \alpha/R^3)(1 + 9\alpha \sigma_f^{3/2} \theta^{3/2})} \right] \qquad (15)$$

where subscript m refers to the substrate (electrode) metal and subscript f refers to the adsorbate (seed) material; $G(\theta) = 1 - 3\theta^2 + 2\theta^3$

[†] Electron emission S-curves are plots of saturated, field free electron emission versus 1000/T with the atom evaporation rate as a running parameter.

is a shape factor; $\cos\beta = \left(1 - 1/(2\sigma_m R^2)\right)^{\frac{1}{2}}$; $R = r_m + r_f$ is the sum of the covalent radii; α is the electronic polarizability of the adsorbate-substrate molecules; σ_f is the number of sites available for adsorbed particle occupancy per unit substrate area and is related to the surface density σ_m by a constant ratio for each adsorbate-substrate combination. σ_m varies among samples of the same substrate metal depending on the surface preparation.

The rate of electron emission from the surface is given by the well-known Richardson-Dushman equation:

$$\nu_e = g_e \frac{2\pi m_e (kT_w)^2}{h^3} \exp\left(- e \frac{\phi_e}{kT_w}\right) , \qquad (16)$$

where g_e is the electron degeneracy (= 2).

The desorption energy of an atom (ϕ_a) or an ion (ϕ_i^*) is defined as the potential energy difference required to remove an adsorbed particle from the surface in the form of a free atom or free ion, respectively.

$$\phi_a = \phi_e^* F(1+\delta) + (\phi_f' \phi_m')^{\frac{1}{2}} S_{fm} Q_{fm} \qquad (17)$$

where the charge function

$$F = \frac{.422(\phi_m - \phi_f) G(\theta)}{R(1 + \alpha/R^3)}$$

with $(\phi_m - \phi_f)$ in eV, R in angstroms, and α in cubic angstroms; $\delta = \frac{F}{\phi_e^*}\left(\frac{e^2}{4\pi\varepsilon_o R} - V_f\right)$ with the adsorbate ionization potential (V_f) and $(e^2/4\pi\varepsilon_o R)$ in the same unit of energy as ϕ_e^*; the heats of sublimation (ϕ_f', ϕ_m') have the same unit of energy as ϕ_e^* and ϕ_a; $S_{fm} = 2/(S_f/S_m + S_m/S_f)$ where S_f and S_m are orbital strengths;

the charge efficiency $Q_{fm} = (1 - F^2/v^2)^{\frac{1}{2}}$ where v is the number of valence electrons in a free adsorbate particle.

The ion desorption energy is found by the relation:

$$\phi_i^* = \phi_a + V_f - \phi_e^* \ . \tag{18}$$

Typical values for ϕ_a and ϕ_i^* are of the order of two eV, so that the inert carrier gas with a thermal energy of the order of two-tenths eV should not affect the adsorption process of the alkali seed.

The rate at which the atom or ion specie desorbs (evaporates) from the surface is given in Arrhenius form by (c. g. s. units):

$$\nu_s = g_s \sigma_f \theta \nu \psi(\theta) \exp\left(- \frac{e\phi_s}{kT_w}\right), \tag{19}$$

where g_s is the statistical weight of the ground electronic state; ψ is related to the configuration entropy difference and is estimated as:

$$\psi = \frac{1}{\sqrt{1-\theta}\,(1 - \sqrt{\theta}\,)} \exp\left(\frac{1}{2}\left[\frac{\sqrt{\theta}}{1 - \sqrt{\theta}} + \frac{\theta}{1-\theta}\right]\right) \ .$$

This is not valid as $\theta \to 1$ because the build-up of the second layer is not accounted for. ν is the characteristic frequency of vibration of the adsorbed particles, and is approximately:

$$\nu = \frac{1}{2\pi R \cos\beta} \sqrt{\phi_a (m_f + 4m_m)/2m_f m_m} \ .$$

Table 1 is a list of physical constants needed to apply the above expressions for an alkali metal adsorbed on a molybdenum, tantalum, or tungsten surface. A list for additional metals may be found in reference 8.

Calculated desorption rate isotherms for the potassium-tungsten system are displayed in Figure 2 for atoms, ions, and

TABLE 1a. Physical Constants* of Some Refractory Metals

Metal		Mo	Ta	W
ϕ'_m (eV)	heat of sublimation	6.84	8.11	8.68
ϕ_m (eV)	electron work function	4.38	4.19	4.62
r_m (Å)	covalent radius	1.29	1.34	1.30
S_m	orbital strength	2.31	2.62	2.62

TABLE 1b. Physical Constants* of Alkali Metal Adsorbates

Film		Cs	Rb	K	Na	Li
ϕ'_f (eV)	heat of sublimation	0.80	0.84	0.92	1.12	1.66
ϕ_f (eV)	electron work function	1.81	2.09	2.22†	2.28	2.49
r_f (Å)	covalent radius	2.35	2.16	2.02	1.57	1.22
S_f	orbital strength	1.00	1.00	1.00	1.00	1.00
α (Å^3)	polarizability	13.0	10.1	8.2	3.9	1.8
V_f†† (eV)	ionization potential	3.89	4.18	4.34	5.14	5.39
v	valence	1	1	1	1	1
g_a	atomic statistical weight	2	2	2	2	2
g_i	ion statistical weight	1	1	1	1	1

For alkali metal adsorbates on Mo, Ta, or W substrates:

$$\sigma_f/\sigma_m = 1/4 .$$

*Except where noted, data are taken from Levine and Gyftopoulos(8).

†Taken from Samsonov(29).

††Taken from reference 30.

electrons and for three surface temperatures. A comparison of electron emission S-curves computed from these results with experiments is made later in Part IV. Note the strong dependence of the desorption rates of all species on T_w and θ. The electron emission rate reaches a maximum at $\theta \approx .65$ and then decreases to the value for pure potassium at a monolayer coverage. Since second layer effects are not accounted for, the atom and ion desorption rates diverge near $\theta = 1$.

If large electric fields exist near the electrode surface, the emission rates of ions and electrons will be affected. For moderately large electric fields ($< 10^5$ volts/cm), the Schottky effect accounts for this. The Schottky effect is the effective reduction of the thermionic work function by the field's modification of the mirror-image force on a charged particle leaving a conducting surface. Since this reduction occurs within a distance of about 10^{-6} cm from the surface(11) (smaller than any characteristic plasma length considered here), the Schottky effect is evaluated by the electric field at the surface (E_w). The Schottky reduction is:

$$\Delta\phi = \left(\frac{e|E_w|}{4\pi\epsilon_o}\right)^{\frac{1}{2}} . \tag{20}$$

If the electric field retards the type of charged particles leaving the surface, the Schottky correction is zero for that type, since in a monotonically changing potential from solid into plasma there is no barrier whose magnitude would control the emitted flux.

Defining E_w positive if directed away from the surface, the corrected work functions are:

$$\phi_e = \begin{cases} \phi_e^* - \Delta\phi & E_w < 0 \\ \phi_e^* & E_w \geq 0 \end{cases}$$
$$\phi_i = \begin{cases} \phi_i^* & E_w \leq 0 \\ \phi_i^* - \Delta\phi & E_w > 0 \end{cases} \tag{21}$$

Substituting ϕ_e into equation (16) and ϕ_i into equation (19) gives the corrected emission rates.

2. 4 Plasma - Surface Coupling

The basic differential equations which govern the plasma behavior are continuum relations which require continuum boundary conditions. These boundary conditions are the limits of the number densities within the continuum formalism as the surface is approached. The plasma solution depends on the surface conditions via the boundary conditions, while the solution for the surface coverage (θ) and the emission rates depend on the plasma problem. Thus, the plasma problem and the surface problem must be solved simultaneously. This section presents a method for coupling the plasma to the surface.

Since the surface temperature (T_w) is arbitrarily specifiable, the surface conditions depend on θ and E_w. First, the connection of boundary conditions to θ and E_w will be established. Immediately adjacent to the electrode surface, there must be a thin molecular layer of thickness on the order of a mean free path (Knudsen layer). At the outer edge of this layer, continuum relations hold with fluxes given by equation (3), while at the surface the distribution function must change to a strongly non-continuum type. Since only the number densities at the edge of the Knudsen layer are required, the approximate method of Bienkowski$^{(12)}$ is used to find them. This method assumes that the distribution function of the particles arriving at the surface is a displaced Maxwellian. Since the Knudsen layer is thin compared to the curvature of the electrode surface, and neglecting any chemical reactions in the layer, the continuity equation requires that the flux be constant across this layer. Thus, the continuum expression for Γ_s can be equated to the balance of fluxes at the surface.

Consider a Maxwellian distribution function, $f(\vec{v})$, displaced by the drift velocity, v_d. Near the electrode surface, the flux of particles hitting the control surface on the negative side is:

$$\mu_s = - \int_{-\infty}^{0} \int_{-\infty}^{\infty} \int_{-\infty}^{\infty} v_1 f(\vec{v}) d\bar{v} \quad ,$$

where the integration gives:

$$\mu_s = -n_{sw} \frac{v_d}{2} + n_{sw} \frac{v_d}{2} \operatorname{erf}\left(\frac{v_d}{\bar{C}_s} \frac{2}{\sqrt{\pi}} \right) + n_{sw} \frac{\bar{C}_s}{4} \exp\left[- \frac{4}{\pi} \left(\frac{v_d}{\bar{C}_s} \right)^2 \right] .$$

Since $\Gamma_s \equiv n_{sw} v_d$ and the continuity relation is $(\Gamma_{sw} = \nu_s - \mu_s)$, we have:

$$\nu_s = \frac{\Gamma_{sw}}{2} \left(1 + \operatorname{erf}\left\{ \frac{2}{\sqrt{\pi}} \frac{\Gamma_{sw}}{n_{sw} \bar{C}_s} \right\} \right) + \frac{n_{sw} \bar{C}_s}{4} \exp\left[- \frac{4}{\pi} \left(\frac{\Gamma_{sw}}{n_{sw} \bar{C}_s} \right)^2 \right] .$$

Dividing the above equation by $n_{sw} \bar{C}_s$ and defining $f \equiv (n_{sw} \bar{C}_s)/\nu_s$, $\xi \equiv (2\Gamma_{sw})/(\sqrt{\pi}\, n_{sw} \bar{C}_s)$, and $P_s \equiv \Gamma_{sw}/\nu_s$, we have

$$\frac{1}{f} = \frac{\sqrt{\pi}}{4} \xi [1 + \operatorname{erf}(\xi)] + \frac{1}{4} \exp(-\xi^2) ,$$

$$P_s = \frac{\sqrt{\pi}}{2} \xi f(\xi) .$$

From the expressions, we can find numerically a function $f(P_s)$

(displayed in Figure 3). The boundary conditions are easily computed from this function by

$$n_{sw} = \frac{\nu_s}{\bar{C}_s} f\left(\frac{\Gamma_{sw}}{\nu_s}\right) \qquad s = i, e, a \quad . \tag{22}$$

For $P_s << 0$, a convenient asymptotic form for computation is:

$$f \simeq \frac{-2P_s}{\sqrt{\pi}\left[\ell n\left(\frac{-P_s}{4\sqrt{\pi}}\right) - \frac{3}{2}\left(1 - \frac{293}{P_s}\right)\ell n\left(\ell n\left\{\frac{-P_s}{4\sqrt{\pi}}\right\}\right)\right]^{\frac{1}{2}}} \quad , \tag{23}$$

accurate to 4 percent for $P_s < -1000$. For $|P_s| << 1$, an approximate form is

$$n_{sw} \simeq \frac{2}{\bar{C}_s}(2\nu_s - \Gamma_{sw}) \ . \tag{24}$$

Hence, we have relationships of the form: $n_{sw} = \mathrm{fn}\,[\nu_s(\theta, E_w), \Gamma_{sw}]$, which are used later.

An additional condition is obtained, following Sajben(13), by considering the conservation of heavy seed particles at the wall. For a surface - plasma system in steady state, there is no net accumulation of seed particles at the wall. Neglecting any surface diffusion fluxes of adatoms compared to their desorption rate $(\nu_a+\nu_i)$, the net flux of heavy particles to the wall is equal to the net flux of heavies away from it:

$$\nu_a + \nu_i = \mu_a + \mu_i$$

or

$$\nu_a - \mu_a = -(\nu_i - \mu_i) \ ,$$

which gives:

$$\Gamma_{aw} = -\Gamma_{iw} \ . \tag{25}$$

This means that there is, in general, a neutral seed atom density gradient near the wall, and the atom diffusion equation must be solved, simultaneously with the plasma and the surface problem, subject to the boundary conditions at infinity and the conditions at the surface given by equations (22) and (25).

2.5 Solution Method

It is quite difficult to solve (even numerically) the continuum equations of section 2.2 as they presently stand. However, for the plasma conditions of interest here, it will be shown that the effects of number density gradients and charge separation are restricted to an electric boundary layer that is thin compared to the characteristic length of the plasma. Outside this electric boundary layer is a large outer region called the bulk plasma, where the current density is the governing parameter.

The bulk plasma region has been studied extensively to elucidate the physical processes occurring$^{(1, 2)}$, and to predict current distributions due to complicated geometries$^{(14, 15)}$. Since the main purpose here is to study the interaction of electrodes with the plasma, only simple outer solutions (constant electron temperature) are considered here. For this case, the electron number density is uniform in the bulk plasma, since it is evaluated by Saha's equation. The technique of solving the bulk plasma problem is to assume a value for T_e and use equation (4) in the form $+J_{e\infty}^2/\sigma_e(T_e) = +\dot{\Omega}+\dot{R}$ to find $J_{e\infty}$. Since $J_{i\infty} << J_{e\infty}$, $J_{e\infty}$ is usually taken equal to J_t (the total current density). The details of evaluating $\dot{\Omega}$ and $\dot{R}$ can be found in references 1, 2, and 16. This provides for each J_t the proper values of T_e, $n_{a\infty}$, $n_{e\infty}$, and E_∞ with which to match the electric boundary layer solution.

In recent years, the technique of asymptotic analysis has been used by several authors(12, 17-20) to develop a continuum probe theory. The method developed by Lam(19) for a slightly ionized gas flowing around a solid body with perfectly absorbing surfaces is extended here to include production, variable transport coefficients, and large rates of surface emission.

We non-dimensionalize the variables:

$$\begin{array}{lll} \vec{u} = u_\infty \vec{V} & \psi = \dfrac{-e\phi}{kT_e} & \dot{N} = \dfrac{\epsilon L^2}{D_{io} n_{e\infty}} \dot{n} \\[2ex] N_i = \dfrac{n_i}{n_{e\infty}} & N_e = \dfrac{n_e}{n_{e\infty}} & N_a = \dfrac{n_a}{n_{a\infty}} \\[2ex] \vec{\Gamma}_i = \vec{\gamma}_i \dfrac{D_{io} n_{e\infty}}{\epsilon L} & \vec{\Gamma}_e = \vec{\gamma}_e \dfrac{D_{eo} n_{e\infty}}{L} & \vec{\Gamma}_a = \vec{\gamma}_a \dfrac{D_{ao} n_{a\infty}}{\epsilon L} \end{array}$$

$$\tilde{D}_s = \frac{D_s}{D_{so}} \qquad \tilde{T}_i = \frac{T_i}{T_{io}} \tag{26}$$

where u_∞ is a characteristic free-stream velocity, L is a characteristic electrode length with respect to which all spatial variables are non-dimensionalized, and the subscripts o and ∞ refer to values in the sheath and the bulk plasma, respectively.

The following parameters arise naturally after the above non-dimensionalization:

$$\alpha = \frac{h_{e\infty}}{L}$$

where $h_{e\infty} = \left[(\epsilon_o kT_e)/(e^2 n_{e\infty})\right]^{\frac{1}{2}}$ is the bulk plasma Debye length,

$$\epsilon = \frac{T_{io}}{T_e} \qquad \beta = \frac{D_{io}}{\epsilon D_{eo}} \qquad R = \frac{\epsilon u_\infty L}{D_{io}}$$
$$\omega = \frac{\epsilon L^2 n_{e\infty}^2 \gamma}{D_{io}} \qquad \tau = \frac{D_{io}}{D_{ao}} \qquad \sigma = \frac{n_{e\infty}}{n_{a\infty}} \tag{27}$$

The governing plasma equations now become:

$$\alpha^2 \nabla^2 \psi = N_i - N_e \tag{28}$$

$$R\vec{V} \cdot \nabla N_i + \nabla \cdot \vec{\gamma}_i = \dot{N} \tag{29}$$

$$\beta R \vec{V} \cdot \nabla N_e + \nabla \cdot \vec{\gamma}_e = \beta \dot{N} \tag{30}$$

$$\tau R \vec{V} \cdot \nabla N_a + \nabla \cdot \vec{\gamma}_a = -\tau\sigma\dot{N} \tag{31}$$

$$\dot{N} = \omega N_e (N_a - N_e N_i) \tag{32}$$

$$\vec{\gamma}_i = \widetilde{D}_i \left[-\epsilon \nabla N_i + \frac{N_i}{\widetilde{T}_i} \nabla \psi \right] \tag{33}$$

$$\vec{\gamma}_e = \widetilde{D}_e [-\nabla N_e - N_e \nabla \psi] \tag{34}$$

$$\vec{\gamma}_a = -\widetilde{D}_a \epsilon \nabla N_a \tag{35}$$

where $\vec{V}$, $\widetilde{D}_i$, $\widetilde{D}_e$, and $\widetilde{D}_a$ are known functions of the spatial variables $\vec{r}$ and of the dependent variables N_i and N_e.

The boundary conditions are:

$$N_e = N_i = N_a \to 1 \qquad \text{and} \qquad \vec{n} \cdot \nabla \psi \to (eL/kT_e) E_\infty$$

at infinity, where $\vec{n}$ is the unit outward normal to the electrode surface, while on the surface,

$$\psi = \psi_w, \quad N_e = N_{ew}(\theta, E_w), \quad N_i = N_{iw}(\theta, E_w), \quad \vec{n} \cdot \nabla N_a \big|_w = \frac{\sigma\tau}{\epsilon} \gamma_{iw},$$
$$N_a = N_{aw}(\theta) \tag{36}$$

where $E_w \equiv \vec{n}\cdot\vec{E}|_w$ and $\gamma_{iw} \equiv \vec{n}\cdot\vec{\gamma}_i|_w$. The extra boundary condition is needed to solve for θ, which determines the state of the surface.

By suitably combining equations (28) - (35) and neglecting terms of $O(\alpha^4)$, we arrive at the following three coupled, non-linear differential equations for N_i, N_a, and ψ:

$$\nabla\cdot[(\tilde{D}_e+\epsilon\tilde{D}_i)\nabla N_i+(\tilde{D}_e-\tilde{D}_i/\tilde{T}_i)N_i\nabla\psi]-(1+\beta)R\vec{V}\cdot\nabla N_i+(1+\beta)\omega(N_iN_a-N_i^3) =$$
$$= \alpha^2\left[\nabla\cdot\{\tilde{D}_e(\nabla[\nabla^2\psi]+\nabla\psi\nabla^2\psi)\}-\beta R\vec{V}\cdot\nabla(\nabla^2\psi)\right]+\alpha^2(1+\beta)\omega[N_a\nabla^2\psi-2N_i^2\nabla^2\psi] \tag{37}$$

$$\nabla\cdot[(\tilde{D}_e+\beta\tilde{D}_i/\tilde{T}_i)N_i\nabla\psi+(\tilde{D}_e-\beta\epsilon\tilde{D}_i)\nabla N_i]$$
$$= \alpha^2\left[\nabla\cdot\{\tilde{D}_e(\nabla[\nabla^2\psi]+\nabla^2\psi\nabla^2\psi)\}-\beta R\vec{V}\cdot\nabla(\nabla^2\psi)\right] \tag{38}$$

$$\nabla\cdot(\epsilon\tilde{D}_a\nabla N_a)-\tau R\vec{V}\cdot\nabla N_a-\tau\sigma\omega(N_iN_a-N_i^3) = \alpha^2\tau\sigma\omega[N_a\nabla^2\psi-2N_i^2\nabla^2\psi] \tag{39}$$

To study the electric boundary layer, let y be a boundary layer coordinate normal to the electrode surface and denote the tangential boundary layer coordinates by a subscript t. Define $\delta \equiv 1/(R+\omega)^{\frac{1}{2}}$ and consider the case for $\delta \ll 1$. We introduce a scaled normal coordinate η by

$$\eta = y/\delta . \tag{40}$$

The continuity equation of neutral gas flow implies $\vec{V}_t = O(1)$ and V (normal velocity component) = $O(\delta)$. Considering that the convection and the production term may be of equal importance, ($R \simeq \omega$) implies that $R = O(\delta^{-2})$ and $\omega = O(\delta^{-2})$.

In terms of boundary layer coordinates and neglecting terms of $O(\delta)$ and higher, the above three governing equations and equation (28) give the following system of equations for N_i, N_e, N_a, and ψ:

$$\frac{\partial}{\partial\eta}\left[(\tilde{D}_e+\epsilon\tilde{D}_i)\frac{\partial N_i}{\partial\eta}+\left(\tilde{D}_e-\frac{\tilde{D}_i}{\tilde{T}_i}\right)N_i\frac{\partial\psi}{\partial\eta}\right]-(1+\beta)R\delta^2\left(V_t\cdot\nabla_t N_i+\frac{V}{\delta}\frac{\partial N_i}{\partial\eta}\right)+$$

$$+\;(1+\beta)\delta^2\omega(N_iN_a-N_i^3)$$

$$=\frac{\alpha^2}{\delta^2}\left[Q+(1+\beta)\delta^2\omega\left(N_a\frac{\partial^2\psi}{\partial\eta^2}-2N_i^2\frac{\partial^2\psi}{\partial\eta^2}\right)\right] \qquad (41)$$

$$\frac{\partial}{\partial\eta}\left[\left(\tilde{D}_e+\beta\frac{\tilde{D}_i}{\tilde{T}_i}\right)N_i\frac{\partial\psi}{\partial\eta}+(\tilde{D}_e-\beta\epsilon\tilde{D}_i)\frac{\partial N_i}{\partial\eta}\right]=\frac{\alpha^2}{\delta^2}Q \qquad (42)$$

$$N_e = N_i-\frac{\alpha^2}{\delta^2}\frac{\partial^2\psi}{\partial\eta^2}-\alpha^2\nabla_t^2\psi \qquad (43)$$

$$\frac{\partial}{\partial\eta}\left(\epsilon\tilde{D}_a\frac{\partial N_a}{\partial\eta}\right)-\tau R\delta^2\left[\vec{V}_t\cdot\nabla_t N_a+\frac{V}{\delta}\frac{\partial N_a}{\partial\eta}\right]-\tau\sigma\omega\delta^2(N_iN_a-N_i^3)=$$

$$=\alpha^2\tau\sigma\omega\left[\frac{\partial\psi}{\partial\eta}(N_a-2N_i^2)\right] \qquad (44)$$

where

$$Q\equiv\frac{\partial}{\partial\eta}\left[\tilde{D}_e\frac{\partial^3}{\partial\eta^3}\psi+\tilde{D}_e\frac{\partial\psi}{\partial\eta}\frac{\partial^2\psi}{\partial\eta^2}\right]-\beta R\delta^2\left[\vec{V}_t\cdot\nabla_t\left(\frac{\partial^2\psi}{\partial\eta^2}\right)+\frac{V}{\delta}\frac{\partial^3\psi}{\partial\eta^3}\right]. \qquad (45)$$

Ambipolar Diffusion. When $(\alpha/\delta)^2 \ll 1$, equation (43) implies $N_i \approx N_e \equiv N$. This region, where charge separation is negligible, is called the ambipolar diffusion region. Neglecting terms of $O(\alpha^2/\delta^2)$ in equation (42), we can integrate once to give

$$\frac{\partial\psi}{\partial\eta}=\frac{C_\infty-(\tilde{D}_e-\beta\epsilon\tilde{D}_i)\frac{\partial N}{\partial\eta}}{(\tilde{D}_e+\beta\,\tilde{D}_i/\tilde{T}_i)N}\;, \qquad (46)$$

where $C_\infty=(\tilde{D}_{e\infty}+\beta\,\tilde{D}_{i\infty}/\tilde{T}_{i\infty})\,\delta\,(eL/kT_e)E_\infty$ is found by fitting the boundary condition given by equation (36) at $\eta=\infty$.

Neglecting the right hand side of equation (41) and substituting equation (46) into the left hand side, we obtain:

$$-\frac{\partial^2 N}{\partial\eta^2} = \frac{\tilde{D}_e\tilde{T}_i+\beta\tilde{D}_i}{\tilde{D}_e\tilde{D}_i(1+\epsilon\tilde{T}i)}\Big[-\frac{\partial N}{\partial\eta}\left(\frac{\partial}{\partial\eta}\left\{\frac{\tilde{D}_e\tilde{D}_i(1+\epsilon\tilde{T}_i)}{\tilde{D}_e\tilde{T}_i+\beta\tilde{D}_i}\right\}+R\delta V\right) -$$

$$-R\delta^2\vec{V}_t\cdot\nabla_t N+\delta^2\omega(NN_a-N^3)+\frac{C_\infty}{(1+\beta)}\frac{\partial}{\partial\eta}\left\{\frac{\tilde{D}_e\tilde{T}_i-\tilde{D}_i}{\tilde{D}_e\tilde{T}_i+\beta\tilde{D}_i}\right\}\Big] \qquad (47)$$

Equation (47) with boundary conditions for N determines N for the ambipolar diffusion region. The outer boundary condition is: $N = 1$ as $\eta \rightarrow \infty$. Since equation (47) is parabolic, an appropriate upstream condition is also required. The inner boundary condition is found by matching to the inner solution. For an electrode, two matching possibilities exist:

$$\begin{array}{lll} \text{case (a)} & N = N_o(\vec{r}_t) > 0 & \text{at } \eta = 0 \\ \text{case (b)} & N = 0 & \text{at } \eta = \eta_o(\vec{r}_t) \geq 0 \end{array} \qquad (48)$$

where N_o or η_o is determined by the inner solution.

The ambipolar diffusion problem is governed by the solution for N, since the electric field terms can be eliminated (due to quasi-neutrality) to give a differential equation for N. The solution for N, however, is coupled to the atom diffusion problem by the production term (containing N_a) in equation (47) and is coupled to the sheath problem by the inner boundary conditions.

The variation in potential through the ambipolar region can be found (after N is solved for) by integrating equation (46). The first term in equation (46) depends on the total current density in the ambipolar region,and the potential change due to this term is just the change in mobility caused by N.

The extra term in equation (46) is explained as follows: since electrons diffuse faster than the massive ions, electric fields must exist to retard the electron motion and to speed up the ion transport in order to maintain quasi-neutrality. This electrostatic field causes the additional potential change in the ambipolar region and is accounted for by the second term in equation (47). The electrostatic field affects the electrons much more than it does the ions, which limits the diffusion rate of electrons to that of the ions. Since β is typically $O(10^{-3})$, the coefficient of the bracketed terms of equation (47) is nearly $\tilde{T}_i/[\tilde{D}_i(1+\epsilon\tilde{T}_i)]$, which demonstrates the insensitivity of ambipolar diffusion to the electron diffusion coefficient, D_e.

The normalized transport coefficients, $\tilde{D}_e$ and $\tilde{D}_i$, depend on T_i, N_i, and N_e. If the number densities are small, they have negligible effect on the transport coefficients. If the inner (sheath) region is much thinner than the thermal boundary layer, T_i changes by a small amount. If the number densities in the sheath are large, it will be noticed that their variation through the sheath is small. Therefore, we make the following approximation: the transport coefficients in the sheath are constant and evaluated at the surface temperature and by $N = N_o$ if case (a), or $N = 0$ if case (b). Since we normalized by these values, $\tilde{D}_e$, $\tilde{D}_i$, and $\tilde{T}_i$ are equal to unity in the sheath region.

For matching purposes, the ambipolar diffusion solution is represented near the surface by:

case (a)

$$N \simeq N_o + I\eta$$

$$\frac{\partial\psi}{\partial\eta} \simeq \frac{C_\infty - (1-\beta\epsilon)I}{(1+\beta)(N_o+I\eta)} \tag{49}$$

where $I \equiv \partial N/\partial\eta|_{\eta=0}$: this possibility was not considered by Lam$^{(19)}$.

case (b)
$$N \simeq I(\eta - \eta_o)$$
$$\frac{\partial\psi}{\partial\eta} \simeq \frac{C_\infty - (1-\beta\epsilon)I}{(1+\beta)I(\eta-\eta_o)} \tag{50}$$

where $I \equiv \partial N/\partial\eta|_{\eta=\eta_o}$.

In case (b), as $\eta \to \eta_o$, $\partial\psi/\partial\eta$ tends to infinity. This requires a thin sheath region (diffusion sheath) to exist adjacent to the surface. No such singularity occurs for case (a), but in general $N_{ew} \neq N_{iw}$. A thin sheath (relaxation sheath) must then exist to relax N_e and N_i to a common value (see Figure 4).

For $I > 0$, the sheath may be studied in the same way for both cases by the following artifice: by defining an effective $\eta_{o_{eff}} \equiv -N_o/I$, the case (a) representation takes on the same form as case (b).

Sheath Equations. To study the sheath, we must rescale the variables as follows:

$$\eta = \eta_o + \left(\frac{\alpha^2}{\delta^2 I}\right)^{1/3} t ,$$
$$N_i = \left(\frac{\alpha I}{\delta}\right)^{2/3} K(t) , \tag{51}$$
$$N_e = \left(\frac{\alpha I}{\delta}\right)^{2/3} G(t) .$$

We then transform equations (41) - (43) and set $\tilde{D}_e = \tilde{D}_i = \tilde{T}_i = 1$. Provided that I, η_o, and ∇_t terms are $O(1)$, and neglecting terms of order $(\alpha^2/\delta^2 I)^{1/3}$ and higher, we find a set of differential equations identical (save for one constant) to those of Lam's$^{(19)}$ continuum probe sheath. These sheath equations are one-dimensional (in t), and independent of production and convection terms. By manipulating these equations as in reference 19, the sheath problem is reduced to the solution of this differential equation:

$$\epsilon \frac{d^2W}{dt^2} = (\epsilon-1)W\frac{dW}{dt} + \frac{W}{2}[W^2+2(1+\epsilon)t] - (1+\epsilon)X \tag{52}$$

where $W = -d\psi/dt$ is the normalized field, and for our case $X = [(1-\beta\epsilon)I-C_\infty]/I(1+\beta)$.

The number densities $K(t)$ and $G(t)$ can be found from W by the following relations:

$$K = t + \frac{1}{1+\epsilon}\left(\frac{W^2}{2} - \frac{dW}{dt}\right) \tag{53}$$

$$G = K + \frac{dW}{dt} \tag{54}$$

The outer boundary condition for equation (52), provided by matching to the inner behavior of the ambipolar solution is:

$$W = X/t \qquad\qquad \text{as } t \to \infty \ . \tag{55}$$

The boundary conditions at the surface (denoted by t_w) are specified in a manner similar to Bienkowski(12), where now the surface conditions are functions of θ and W_w. Define

$$\left.\begin{aligned} A &\equiv G_w + \epsilon K_w \\ B &\equiv G_w - K_w \end{aligned}\right. \tag{56}$$

where

$$G_w = \left(\frac{\alpha I}{\delta}\right)^{-2/3} N_{ew}(\theta, W_w)$$

and

$$K_w = \left(\frac{\alpha I}{\delta}\right)^{-2/3} N_{iw}(\theta, W_w) \ .$$

Substitution of equations (53) - (54) into equations (56) specifies that the solution curve for W intersect a parabola

$$W_w^2 = -2(1+\epsilon)t_w + 2A \tag{57}$$

with the slope

$$dW/dt\big|_{t=t_w} = B \ . \tag{58}$$

The mathematical problem now is to find the proper value of t_w that enables the solution of the sheath equation (52) to satisfy the boundary conditions given by equations (58) and (55).

The fluxes are constant throughout the sheath and are related to X by:

$$\begin{aligned} \gamma_i &= \frac{I}{\delta}[-X-\epsilon] \\ \gamma_e &= \frac{I}{\delta}[X-1] \end{aligned} \tag{59}$$

This allows us to relate the surface condition on atom diffusion to the ambipolar diffusion problem:

$$\frac{\partial N_a}{\partial \eta}\bigg|_w = \frac{\sigma\tau}{\epsilon(1+\beta)}[C_\infty - (1+\epsilon)I] \ . \tag{60}$$

Unless $t_w << -1$, $\eta_{sh} = O\left((\alpha^2/\delta^2 I)^{1/3}\right)$ (reference 19), and this thinness of the sheath simplifies equation (44) to:

$$\epsilon \frac{\partial}{\partial \eta}\left(\tilde{D}_a \frac{\partial N_a}{\partial \eta}\right) = \tau R \delta^2\left[\vec{V}_t \cdot \nabla_t N_a + \frac{V}{\delta}\frac{\partial N_a}{\partial \eta}\right] + \sigma\tau\omega\delta^2(NN_a - N^3) \ . \tag{61}$$

For case (b), $\eta_o = \eta_{sh}$, so η_o can be set equal to zero in the solution of the ambipolar diffusion equation (47); this simplifies matters, for I does not depend on the sheath solution. For case (a), however, I depends on the sheath solution through $N_o = (\alpha I/\delta)^{2/3} t_w$.

Potential Drops. The potential drop through the electric boundary layer is found by integrating the composite electric field solution. The potential drop across the electric boundary layer,

$F_{b\ell} = F_{sh} + F_{am}$, is the drop computed by taking the potential at the outer edge of the electric boundary layer and extrapolating to the surface by the electric field in the bulk plasma, i.e.,

$$-F_{b\ell} = \psi(\delta_{b\ell}) - E_{\infty}\frac{eL}{kT_e}\delta_{b\ell} \ .$$

For case (b), the sheath region becomes spatially distinct from the ambipolar region, and it is useful to associate this potential drop with the sheath. We follow Lam's(19) convention of taking $t = 1$ as a dividing point between sheath and ambipolar regions for the purpose of defining potential drops. For case (a), the sheath solution completely overlaps the ambipolar solution; we can define a sheath potential drop that matches with Lam's(19) definition by using his definition for $t_w \leq 1$. For $t_w > 1$, we associate the sheath drop with the potential drop required to relax N_{iw} and N_{ew} to a common value in the ambipolar region.

The sheath potential drop is then defined as:

$$F_{sh} = \int_{t_w}^{C} W dt + \int_{C}^{\infty}\left(W - \frac{X}{t}\right)dt - X \ln C$$

for $t_w \leq 1$,

$$F_{sh} = \int_{t_w}^{C} W dt + \int_{C}^{\infty}\left(W - \frac{X}{t}\right)dt - X \ln \frac{C}{t_w} \qquad (62)$$

for $t_w > 1$,

where C is chosen for convenience. The ambipolar drop must then be:

$$F_{am} = -\int_{\left(\frac{\alpha^2}{\delta^2 I}\right)^{1/3}}^{C_{am}} \frac{\partial\psi}{\partial\eta} - \int_{C_{am}}^{\infty}\left(\frac{\partial\psi}{\partial\eta} - \frac{\delta e L}{kT_e}E_\infty\right)d\eta + \frac{\delta e L}{kT_e}E_\infty C_{am} \qquad \text{for } t_w \leq 1$$

where terms of order $(\alpha^2/\delta^2 I)^{1/3}$ are neglected; (63)

$$F_{am} = -\int_0^{C_{am}} \frac{\partial\psi}{\partial\eta}d\eta + \frac{\delta e L}{kT_e}E_\infty C_{am} - \int_{C_{am}}^{\infty}\left(\frac{\partial\psi}{\partial\eta} - \frac{\delta e L}{kT_e}E_\infty\right)d\eta \qquad \text{for } t_w > 1$$

where C_{am} is chosen for convenience.

Bienkowski$^{(12)}$ proves that the sheath solution cannot saturate ($|F_{sh}| \to \infty$) for any finite A and positive X if $B > 0$. However, one can see from his proof that if $B < 0$, the sheath solution can saturate for positive X, even if A is finite. Thus, a necessary condition for cathode saturation is:

$$N_{iw} > N_{ew} \ .$$

For $\delta << 1$, it is consistent to take the current flow inside the electric boundary layer as essentially normal to the electrode surface$^{(19)}$. C_∞ is then related to J_t by:

$$C_\infty = \frac{L\delta J_t}{D_{eo} n_{e\infty} e} \ .$$

Solution Algorithm. The surface - plasma problem can now be solved by the following procedure. For a given electrode-plasma system, we may independently choose T_w and J_t. First, specify J_t and solve the bulk plasma problem, which yields T_e, $n_{e\infty}$, $n_{a\infty}$, and E_∞. For case (a), we must find the value of N_o which matches the surface to the plasma. One method is to assume a value for N_o and proceed by an iteration process. Next, solve the ambipolar diffusion equation (47) and the atom diffusion equation (61) with the boundary conditions given by equations (48), (60), $N_a \to 1$ at infinity, and appropriate upstream conditions. This solution will give values for I and N_{aw}. Solve the transcendental relation:

$$N_{aw} = \frac{\nu_a(\theta)}{n_{a\infty}\bar{C}_a} f\left(\frac{-\Gamma_{iw}}{\nu_a(\theta)}\right)$$

for the degree of coverage (θ). With θ known, the surface conditions A and B depend on W_w. The sheath equation (52) is solved to satisfy the conditions given by equations (55), (57), and (58), which results in a value for W_w. From the sheath solution, a new value for N_o is calculated and the procedure is iterated until the two values for N_o are equal. For case (b), $N_o = 0$, and the sheath problem has to be calculated only once.

In the general case, J_t, T_w, I, N_o, θ, W_w, and $F_{b\ell}$ are functions of the transverse boundary layer coordinates. $J_t(\vec{r}_t)$ is then specified and the above procedure carried out point by point. The potential in the bulk plasma is then solved subject to the condition:

$$\vec{n} \cdot \nabla\psi = \frac{LJ_t}{D_{eo} n_{e\infty} e(\tilde{D}_{e\infty} + \beta \tilde{D}_{i\infty}/\tilde{T}_{i\infty})}$$

on the surface. This solution gives the potential distribution at the edge of the bulk plasma about the electrode surface; subtracting $\psi_{b\ell}$ from this gives the electrode potential distribution.

2.6 Stagnation Flow Solution

In this section, we carry out the program of section 2.5 for the axisymmetric system shown in Figure 5. Here, a seeded plasma flows down an non-conducting tube, of radius L, and impinges on a flat plate positioned perpendicular to the flow at a distance H from the tube. At the center of the flat plate is an electrode, of radius L, surrounded by an insulator.

We take the flow field inside the tube as uniform; the viscous boundary layer on the tube wall is thin in situations where 1) a settling chamber is placed upstream of a short tube, 2) the pipe flow is turbulent. The pipe flow becomes turbulent at $Re_L \cong 10^3$, whereas the flow over the electrode remains laminar up to $Re_L \cong 10^5$. (24)

The flow field of an axisymmetric jet impinging on a perpendicular flat plate has been studied by potential flow methods by references 21 - 23. Their results indicate that near the plate ($y < .1\ H/L$), the velocity field is approximated by stagnation flow with an error of less than 14 per cent for the region within the radius of the jet. The appropriate value for the stagnation flow constant (a) is: $a = 0.4$ for $H/L = 2.8$. The effect of viscosity is accounted for by using the laminar boundary layer solution for stagnation flow given by Froessling(24).

By neglecting field fringing at the electrode edge, the boundary conditions at infinity are uniform; for T_w uniform, the boundary conditions at the wall are uniform if the solution is independent of r. This is indeed the case, for V depends only on y, and by symmetry $\partial N_s / \partial r |_{r=0} = 0$ enables a one-dimensional (in y) solution to satisfy the differential equations and the boundary conditions of section 2.5. This geometry is then very useful both from the simplification in computation and for the comparison of the theory with experiment.

An analytical expression for V(y) is found by fitting a function to the stagnation boundary layer solution, which results in:

$$V(y) = -2\left(\frac{a\nu}{u_\infty L}\right)^{\frac{1}{2}}\left[\left(\frac{au_\infty L}{\nu}\right)^{\frac{1}{2}} y - .569 + .569\, \exp\left(-\left(\frac{au_\infty L}{\nu}\right)^{\frac{1}{2}} y\left\{1.757 + .41\left(\frac{au_\infty L}{\nu}\right)^{\frac{1}{2}} y\right\}\right)\right] \quad (64)$$

Since T_w is in general different from $T_{n\infty}$, there will also be a thermal boundary layer in front of the electrode. The velocity expression is approximately corrected for this by evaluating the viscosity at the mean film temperature, $\frac{1}{2}(T_w+T_{n\infty})$. To the same degree of approximation, the thermal boundary layer is similar to the viscous boundary layer, being stretched by $Pr^{-1/3}$.(25) The neutral temperature profile is expressed by:

$$T_n(y) = T_{n\infty}+(T_w-T_{n\infty})\exp\left[-\left(\frac{au_\infty L}{\nu}\right)^{\frac{1}{2}} y\, Pr^{\frac{1}{3}}\left(1.757+.41\left(\frac{au_\infty L}{\nu}\right)^{\frac{1}{2}} y\, Pr^{\frac{1}{3}}\right)\right] \quad (65)$$

The number density variation of the carrier gas, n_c, is accounted for by using the above expression for T_n with the perfect gas equation, $p_c = n_c k T_n$. p_c is taken as p_{atm} (the static pressure outside the jet boundary); this is a good approximation when $\frac{1}{2}m_c n_c u_\infty^2 \ll p_{atm}$ and $n_a \ll n_c$.

We now have expressions for the position-dependent coefficients in the differential equations required to solve the stagnation flow problem. In general, these must be handled numerically. However, in certain limiting cases, it is easy to find closed form analytical solutions to the atom diffusion equations and the ambipolar diffusion equations when the transport coefficients are constant. Since these solutions are useful in establishing trends, checking numerical work, and as approximations, we study them here.

Frozen Case. For $R \gg \omega$, the convection term dominates the production term. In this limiting case, $\omega \to 0$, and reactions cease. This results in the decoupling of the atom diffusion differential equation from the ambipolar diffusion equation, while the boundary conditions remain coupled. The simplified equations are:

$$\begin{aligned} \frac{d^2N}{d\eta^2} &= \frac{1+\beta}{1+\epsilon} R\delta V \frac{dN}{d\eta} \\ \frac{d^2N_a}{d\eta^2} &= \frac{\tau}{\epsilon} R\delta V \frac{dN_a}{d\eta} \end{aligned} \tag{66}$$

and have the same form. The velocity field, V, has two limiting forms, inviscid and very viscous.

Frozen Inviscid. For this case, $V(\eta) = -2a\delta\eta$, and the problem reduces to solving

$$\frac{d^2N}{d\eta^2} = -k_s \eta \frac{dN}{d\eta}$$

subject to $N = N_o$ at $\eta = 0$, $N \to 1$ at ∞ where k_s is a constant. The easily found solution is:

$$N = N_o + (1-N_o)\mathrm{erf}\left((k_s/2)^{\frac{1}{2}}\eta\right) \tag{67}$$

$$\left.\frac{dN}{d\eta}\right|_{\eta=0} = (1-N_o)(2k_s/\pi)^{\frac{1}{2}} \quad . \tag{68}$$

Applied to the ambipolar diffusion problem, the solution gives:

$$I = \delta(1-N_o)2\left(\frac{(1+\beta)\epsilon a u_\infty L}{(1+\epsilon)\pi D_{io}}\right)^{\frac{1}{2}} , \tag{69}$$

$$N(\eta) = N_o + (1-N_o)\,\mathrm{erf}\left[\left(aR\frac{1+\beta}{1+\epsilon}\right)^{\frac{1}{2}}\delta\eta\right] . \tag{70}$$

The ambipolar potential drop, F_{am}, requires a numerical integration of a function of the Error Function.

The solution applied to the atom diffusion problem gives an expression for N_{aw}:

$$N_{aw} = 1 - \left(\frac{\pi}{D_a a u_\infty L}\right)^{\frac{1}{2}}\frac{\sigma D_{io}}{2\epsilon(1+\beta)}\left[\frac{C_\infty}{\delta} - (1+\epsilon)\frac{I}{\delta}\right] \tag{71}$$

where I is determined from an ambipolar diffusion solution.

Frozen Viscous. When the atom or ambipolar diffusion takes place inside the viscous boundary layer, the flow field is approximated by taking the first term of an expansion of equation (64), which leads to:

$$V(\eta) = -2\left[.643\ \delta^2 a\left(\frac{a u_\infty L}{\nu}\right)^{\frac{1}{2}}\right]\eta^2 ,$$

and a differential equation of the form:

$$\frac{d^2N}{d\eta^2} = -k_s\eta^2\frac{dN}{d\eta} ,$$

which has the solution:

$$N = N_o + \left.\frac{dN}{d\eta}\right|_0\left(\frac{3}{k_s}\right)^{1/3}\Gamma(\tfrac{4}{3})P\left(\tfrac{1}{3}, \tfrac{k_s}{3}\eta^3\right) \tag{72}$$

where P is an Incomplete Gamma Function (displayed in Figure 6), and $\Gamma(4/3) \approx .893$.

$$\left.\frac{dN}{d\eta}\right|_{\eta=0} = (1-N_o)\left(\frac{k_s}{3}\right)^{1/3}\frac{1}{\Gamma(4/3)} \tag{73}$$

The solution for I in the ambipolar diffusion problem is:

$$I = \delta(1-N_o)\frac{(au_\infty L)^{\frac{1}{2}}}{\Gamma(4/3)}\left[.428\frac{(1+\beta)\epsilon}{(1+\epsilon)D_{io}(\nu)^{\frac{1}{2}}}\right]^{1/3} . \qquad (74)$$

The expression for N_{aw} from the atom diffusion problem is:

$$N_{aw} = 1 - \Gamma(\tfrac{4}{3})\left[2.335\frac{(\nu)^{\frac{1}{2}}}{D_a^2}\right]\frac{\sigma D_{io}}{(au_\infty L)^{\frac{1}{2}}\epsilon(1+\beta)}\left[\frac{C_\infty}{\delta} - (1+\epsilon)\frac{I}{\delta}\right] \qquad (75)$$

Stagnant Case. For $\sigma\omega >> R$, the production terms dominate, and the atom diffusion equation is strongly coupled to the ambipolar diffusion. The equations for $V \rightarrow 0$ simplify to:

$$\begin{aligned} \frac{d^2N_a}{d\eta^2} &= \frac{\sigma\tau\delta^2\omega}{\epsilon}[NN_a-N^3] \\ \frac{d^2N}{d\eta^2} &= -\frac{1+\beta}{1+\epsilon}\delta^2\omega[NN_a-N^3] \end{aligned} \qquad (76)$$

which become, on rearrangement,

$$\frac{d^2N_a}{d\eta^2} = -(\frac{1+\epsilon}{1+\beta})\frac{\sigma\tau}{\epsilon}\frac{d^2N}{d\eta^2} . \qquad (77)$$

Integrating twice gives:

$$N_a + C_1\eta + C_2 = -(\frac{1+\epsilon}{1+\beta})\frac{\sigma\tau}{\epsilon}N . \qquad (78)$$

Applying the condition given by equation (60) requires that C_1 is not equal to zero, so the conditions at infinity cannot be met. This means that both electrodes must be considered in the stagnant case. In the frozen case, the characteristic length entered via the flow field. For the stagnant case, there is no characteristic length unless the other electrode is included so that the electrode separation determines the length scale.

Hybrid Case. For $R \gg \sigma\omega$, but $\omega \gg R$, the atom diffusion equation is convection dominated, while the ambipolar equation is production dominated. For $(\omega/\tau R)^{\frac{1}{2}} \ll 1$, the atom diffusion layer is small compared to the ambipolar diffusion region. N_a is then equal to one throughout most of the ambipolar region. The simplified problem for ambipolar diffusion is:

$$\frac{d^2N}{d\eta^2} = -\frac{1+\beta}{1+\epsilon}\,\delta^2\omega N(1-N^2) \tag{79}$$

where boundary conditions are

$$N = N_o \quad \text{at} \quad \eta = 0 ,$$
$$N = 1 \quad \text{at} \quad \infty .$$

This non-linear differential equation is easily solved by interchanging the roles of the dependent and independent variables. This transformation gives:

$$\frac{1}{2}\frac{d}{dN}\left(\frac{d\eta}{dN}\right)^{-2} = -\left(\frac{1+\beta}{1+\epsilon}\right)\delta^2\omega N(1-N^2) ; \tag{80}$$

integrating once and using the condition $dN/d\eta \rightarrow 0$ as $N \rightarrow 1$ gives an expression for $I = dN/d\eta|_0$:

$$I = \delta\left(\frac{1+\beta}{2(1+\epsilon)}\,\omega\right)^{\frac{1}{2}}(1-N_o^{\,2}) ; \tag{81}$$

integrating twice and inverting the $\eta(N)$ solution results in:

$$N(\eta) = \frac{(1+N_o)/(1-N_o) - \exp\left(-\left(\frac{2(1+\beta)\omega}{1+\epsilon}\right)^{\frac{1}{2}}\eta\delta\right)}{(1+N_o)/(1-N_o) + \exp\left(-\left(\frac{2(1+\beta)\omega}{1+\epsilon}\right)^{\frac{1}{2}}\eta\delta\right)} \qquad N_o \neq 1 \tag{82}$$

For the special case $N_o = 1$, $N(\eta) \equiv 1$.

The ambipolar potential drop is found by using equation (63) for F_{am} and integrating the expression for $d\psi/d\eta$:

$$\frac{d\psi}{d\eta} = \frac{C_\infty}{(1+\beta)N(\eta)} - \left(\frac{1-\beta\varepsilon}{1+\beta}\right)\frac{1}{N}\frac{dN}{d\eta} \;;$$

this results in:

$$F_{am} = -\frac{C_\infty}{\delta}\left(\frac{2(1+\varepsilon)}{\omega(1+\beta)^3}\right)^{\frac{1}{2}} \ln\left(\frac{1}{2}\left(\frac{\delta}{\alpha I}\right)^{\frac{2}{3}}\right) + \frac{1-\beta\varepsilon}{1+\beta}\ln\left(\left(\frac{\delta}{\alpha I}\right)^{\frac{2}{3}}\right) \quad \text{if } t_w \leq 1$$

$$\text{to } O\left(\left(\frac{\alpha^2}{\delta^2 I}\right)^{\frac{1}{3}}\right) \;; \tag{83}$$

$$F_{am} = -\frac{C_\infty}{\delta}\left(\frac{2(1+\varepsilon)}{\omega(1+\beta)^3}\right)^{\frac{1}{2}} \ln\left(\frac{1+N_o}{2N_o}\right) + \frac{1-\beta\varepsilon}{1+\beta}\ln\left(\frac{1}{N_o}\right) \quad \text{if } t_w > 1 \;.$$

<u>Surface Solution.</u> For $\Gamma_{aw} \ll \nu_a$, the relationship between the surface state and the ambipolar and atom diffusion is:

$$\nu_a(\theta) = \frac{n_{a\infty}\bar{C}_a N_{aw}}{4} - \frac{\Gamma_{iw}}{2} \;. \tag{84}$$

Using the frozen viscous case atom solution for N_{aw} given by equation (75) and relating C_∞ to Γ_{iw}, the atom desorption rate is:

$$\nu_a(\theta) = \frac{n_{a\infty}\bar{C}_a}{4} - \Gamma_{iw}\left[\frac{\bar{C}_a}{4}\Gamma\left(\frac{4}{3}\right)\left(2.335\frac{\sqrt{\nu}}{D_a^2}\right)^{\frac{1}{3}}\left(\frac{L}{a u_\infty}\right)^{\frac{1}{2}} + \frac{1}{2}\right] \;. \tag{85}$$

In general, Γ_{iw} is given by:

$$\Gamma_{iw} = \frac{\beta J_t}{(1+\beta)e} - \frac{(1+\varepsilon)D_{io}n_{e\infty}}{(1+\beta)\varepsilon L}\,\frac{I}{\delta} \;; \tag{86}$$

the first term is the ion flux in the bulk plasma and the second term is the change in ion flux due to the source terms (convection and production) in the ambipolar diffusion equation. If the electric boundary layer is thin ($\delta/I \ll 1$), the ion flux to the surface can be much greater than that in the bulk plasma; this large ion flux at the surface causes a substantial increase in the degree of coverage (θ).

The surface state of a cathode ($J_t < 0$) operating near saturation is studied by applying the special case solutions for I/δ with $N_o = 0$. Neglecting the bulk plasma ion flux in equation (86), since $\beta = O(10^{-3})$ and substituting into equation (85) gives:

1) for the frozen inviscid case ambipolar solution,

$$\nu_a(\theta) = \frac{n_{a\infty}\bar{C}_a}{4} + n_{e\infty}\left(\frac{(1+\varepsilon)D_{io}}{\pi\varepsilon(1+\beta)}\right)^{\frac{1}{2}}\left[\frac{\bar{C}_a}{2}\Gamma\left(\frac{4}{3}\right)\left(2.335\frac{\sqrt{\nu}}{D_a^2}\right)^{\frac{1}{3}} + \left(\frac{au_\infty}{L}\right)^{\frac{1}{2}}\right] ; \tag{87}$$

the increase in ion flux due to a velocity rise is partially cancelled by the decrease in N_{aw} (for convection acts as a sink term for atoms) so that ν_a is not strongly dependent on u_∞ or L here.

2) for the hybrid case ambipolar solution,

$$\nu_a(\theta) = \frac{n_{a\infty}\bar{C}_a}{4} + n_{e\infty}^2\left(\frac{(1+\varepsilon)D_{io}\gamma}{2\varepsilon(1+\beta)}\right)^{\frac{1}{2}}\left[\frac{\bar{C}_a}{4}\Gamma\left(\frac{4}{3}\right)\left(2.335\frac{\sqrt{\nu}}{D_a^2}\right)^{\frac{1}{3}}\left(\frac{L}{au_\infty}\right)^{\frac{1}{2}} + \frac{1}{2}\right] . \tag{88}$$

The dependence of ν_a on u_∞ and L is now reversed from that of equation (87). ν_a is now strongly increased by a rise in electron temperature via $n_{e\infty}^2\sqrt{\gamma}$, whereas in equation (87) T_e only entered through $n_{e\infty}$. Since ν_a is a monotonically increasing function of θ, θ will have the same trends as ν_a. Since ν_e behaves similarly to ν_a for $\theta < .6$, the electron emission will also have similar trends.

2.7 Computation Scheme

A computation scheme for numerically solving the stagnation flow system is discussed here. The scheme is valid for $R \gg \sigma\omega$; for this condition, the production term in equation (61) is negligible, so that the atom diffusion differential equation is decoupled from the ambipolar diffusion solution. The surface, sheath, and atom diffusion solutions are then coupled to the ambipolar solution only through I, while the solution for I depends on N_o.

The iteration process is speeded up by the following device: approximately relate I to N_o by the quadratic $I = I_o - (I_o + K_1)N_o + K_1 N_o^2$; find I_o by solving the atom and the ambipolar diffusion problems for I at $N_o = 0$; find K_1 by solving for I at another value of N_o, say .4.

The numerical procedure of solution is outlined here in flow chart form, Figure 7, while a complete listing of the Fortran program is contained in Appendix C. The flow chart indicates the order in which segments are executed. Each segment (denoted by a letter) is described in the following table:

A. Define the transport coefficients as functions of T_n and N; define the velocity and temperature fields as functions of y.

B. Set $N_o = 0$.

C. Read T_w, T_e, J_t.

D. Compute the plasma properties. Assume a starting value for I.

E. Find $N_a(\eta)$ by integrating the atom diffusion equation:

$$\frac{d^2 N_a}{d\eta^2} = \frac{dN_a}{d\eta}\left(\frac{\tau R \delta V}{\epsilon \tilde{D}_a} - \epsilon \frac{d\tilde{D}_a}{d\eta}\right)$$

subject to the boundary conditions

$$\left.\frac{dN_a}{d\eta}\right|_{\eta=0} = \frac{\sigma\tau}{\epsilon(1+\beta)}\left[C_\infty - (1+\epsilon)I\right]$$

and $N_a \to 1$ at $\eta = \infty$.

F. Integrate the ambipolar diffusion equation:

$$\frac{d^2N}{d\eta^2} = \frac{\tilde{D}_e\tilde{T}_i+\beta\tilde{D}_i}{\tilde{D}_e\tilde{D}_i(1+\epsilon\tilde{T}_i)}\left[\frac{dN}{d\eta}\left(R\delta V+\frac{d}{d\eta}\left\{\frac{\tilde{D}_e\tilde{D}_i(1+\epsilon\tilde{T}_i)}{\tilde{D}_e\tilde{T}_i+\beta\tilde{D}_i}\right\}\right)-\omega\delta^2(NN_a-N^3)\right.$$
$$\left.+\frac{C_\infty}{(1+\beta)}\frac{d}{d\eta}\left\{\frac{\tilde{D}_e\tilde{T}_i-\tilde{D}_i}{\tilde{D}_e\tilde{T}_i+\beta\tilde{D}_i}\right\}\right],$$

with the initial conditions $N = N_o$ and $dN/d\eta = I$ at $\eta = 0$. Check convergence of $N \rightarrow 1$ while integrating towards infinity.

G. Compute the iterated value for I.

H. Set $I_o = I$ and $N_o = .4$.

I. Compute K_1.

J. Assume starting values for N_o and E_w.

K. Compute I from the quadratic

$$I = I_o + K_1N_o - (I_o + K_1)N_o^2 .$$

L. Solve the atom diffusion problem as in segment (E) to find N_{aw}. Assume a starting value for θ.

M. Compute $\nu_a(\theta)$.

N. Compute N_{aw} from the relation

$$N_{aw} = \frac{\nu_a}{n_{a\infty}\bar{c}_a}\, f\left(\frac{-\Gamma_{iw}}{\nu_a}\right),$$

and compare with the value determined in segment (L).

O. Calculate the iterated value for θ.

P. Compute N_{iw}, N_{ew}.

Q. Integrate the sheath equation (52) from the starting point, t_w, calculated by equation (57), with the starting slope given by equation (58). Check convergence to the outer boundary condition given by equation (55) while integrating towards infinity.

R. Compute the iterated value for E_w and the corresponding new value for N_o.

S. Calculate the sheath drop, F_{sh}.

T. Write the results of the final iteration: θ, F_{sh}, E_w, N_o, I, N_{ew}, N_{iw}, N_{aw}, ν_e, ν_i, ν_a.

U. Integrate equation (46) to find the ambipolar potential.

V. Compute the ambipolar drop, F_{am}.

W. Write F_{am}, I.

The values of I from segments (T) and (W) can be compared to check on the quadratic expression for I. If the values are too far off, K_1 can be updated and the program rerun.

For W_w large, the integration instability in segment (Q) becomes so severe that the sheath equation (52) cannot be integrated to the ambipolar solution. An approximate solution (described in Appendix B) for the sheath potential drop is used in this event.

2.8 Potassium-Argon-Tungsten System

The problem is now specialized to a potassium-seeded argon plasma with a tungsten electrode and solved numerically. The problem is studied as a function of current density where the main parameters are electrode temperature (T_w), and seed fraction ($\epsilon_K \equiv n_K/n_A$). Constant parameters are $T_{n\infty} = 2000^\circ K$, $u_\infty = 10^4$ cm. /sec., L = .58 cm., p = 1 atm. The electrode temperature is varied from $1200^\circ K$ to $2000^\circ K$, while the seed fraction is varied from .002 to .004.

Langmuir's(6) measured value for the surface density of a "rough" tungsten surface ($\sigma_m = 19.2 \times 10^{14}$ atoms/cm.^{2}) is used. The viscosity of argon, taken from Bird(26) and fitted to a power function, is:

$$\nu = 3.46\ (T_n/2000)^{1.72} \quad \text{cm.}^2/\text{sec.}$$

No data could be found for the mutual diffusion coefficient of potassium in argon. D_{AK} can be estimated by the methods of Bird(26) in terms of the collision cross section Q_A^K. The result is:

$$D_{AK} = \frac{35.7}{Q_A^K}\ (T_n/2000)^{1.65} \quad \text{cm.}^2/\text{sec.}\ ,$$

where Q_A^K is in squared angstroms.

Cool(1) found that the mean cross-sectional values of Q_A^e = 0.7 Å^2 for argon and Q_K^e = 400 Å^2 for potassium give good agreement with the rigorous averaging method for computing the electronic transport coefficients. The values for Q_A^K, Q_A^{K+}, Q_K^{K+} are not as well known. Using the empirical combination formula(26): $Q_C^B = \frac{1}{4}\left(\sqrt{Q_B} + \sqrt{Q_C}\right)^2$, the boiling point formula(26) for Q_B and high energy data (> 1 eV) from Brown(27) for Q_A^{K+}, the cross section estimates are: for Q_A^K, from 12.4 to 56.8 Å^2; for Q_A^{K+}, from 11.3 to 48.1 Å^2; and for Q_K^{K+}, from 16.2 to 133 Å^2. In view of this uncertainty in cross section values, numerical calculations are carried out for the following combinations of values:

<u>mixed combination:</u> $Q_A^K = 56.8$ Å^2, $Q_A^{K+} = 11.3$ Å^2, Q_K^{K+}, 16.2 Å^2.

<u>large combination:</u> $Q_A^K = 56.8$ Å^2, $Q_A^{K+} = 48.1$ Å^2, $Q_K^{K+} = 133$ Å^2.

<u>average combination:</u> $Q_A^K = 34.6$ Å^2, $Q_A^{K+} = 29.7$ Å^2, $Q_K^{K+} = 74.2$ Å^2.

The outer solution has been computed by Cool(1) for a tube with a radius of .58 cm. The corresponding values of $|J_t|$ and T_e

are given in Table 2.

With T_e known, the bulk plasma properties, $n_{e\infty}$, E_∞, $J_{i\infty}$, and $n_{a\infty}$ are easily computed and are shown in Figure 8 as functions of J_t for a seed fraction of .004.

TABLE 2.

Potassium - Argon

$T_{n\infty} = 2000^\circ K$ p = 1 atm. L = .58 cm.

$\epsilon_K = .004$		$\epsilon_K = .002$	
$\lvert J_t \rvert$ (amps/cm^2)	T_e ($^\circ$K)	$\lvert J_t \rvert$ (amps/cm^2)	T_e ($^\circ$K)
.42	2200	.5	2280
1.0	2400	1.0	2470
2.3	2600	2.0	2655
4.9	2800	4.0	2850
9.74	3000	10.0	3140
18.4	3200	20.0	3403
40.5	3500	40.0	3720
70.0	3835	70.0	4030

The three-body recombination coefficient, γ, for potassium is taken from Curry (3) and curve-fitted to give:

$$\gamma(T_e) = .2519 \times 10^{-20} \exp(-2.98 \times 10^{-3} T_e) + 1.256 \times 10^{-25} \text{ cm.}^6/\text{sec.} ,$$

valid for $1000 < T_e < 3500^\circ K$. This expression is compatible with the recombination experiments of Cool(1).

The coefficients in the differential equations are now computed so that the dominant term can be identified. For $|J_t| < 20$ amps/cm.^{2}, $R > \sigma\omega$, so the atom diffusion equation (61) is convection dominated for these current densities. For $|J_t| < 2$ amps/cm.^{2}, $R > \omega$, so the ambipolar diffusion equation (47) is convection dominated only below 2 amps/cm.^{2}.

Since the 0 - 20 amps/cm.^{2} current density range is of the most interest here, the $R > \sigma\omega$ restriction on the computation scheme is not severe. $\Gamma_{aw} << \nu_a$, so the simple form of the surface relationship given by equation (84) is used. Since $D_{AK}/\nu < 1$, the frozen viscous case atom diffusion solution for N_a (from Section 2.6) is incorporated into the numerical scheme by applying it at the wall temperature with the transport coefficients evaluated at a mean neutral temperature. Also, terms involving derivatives of transport coefficients are $O(1/T)$ compared to source terms of $O(1)$, so these are neglected.

2.9 Numerical Results and Discussion

Numerical solutions for a potassium-seeded argon plasma with a tungsten electrode in the stagnation flow geometry (Figure 5) are displayed in Figures 9 - 26. The more interesting case of the electrode operating as a cathode ($J_t < 0$ by the sign convention here) is presented first for several variations of the parameters: T_w, ϵ_K, and cross section values.

Cathode Operation. First, the solution for $T_w = 1500^\circ$K and $\epsilon_K = .004$ computed with the mixed combination of cross section values (see Section 2.8) is studied in detail. Then the dependence of the solution on cathode surface temperature is presented and the implications of the solutions for cathode operation are summarized by thermionic regime graphs (plots of the thermionic limiting current density versus the cathode surface temperature). The modification of the thermionic regime by using other cross section values is shown. Finally, the dependence of the thermionic regime on seed fraction is displayed.

Mixed Cross Sections. Figure 9 shows the current-voltage characteristic in the form of the sheath and the ambipolar voltage drop as a function of the total current density, $(-J_t)$. The sum of the voltage drops $(V_{sh} + V_{am})$ is called the total electrode voltage drop, V_t. Note that for low current densities, V_{sh} is small, O(.1 v), and that at higher current densities, V_{sh} increases sharply to high voltages (> 10 v). The sheath voltages become high when the electron current fraction $(P_e = \Gamma_{ew}/\nu_e)$ approaches a value of unity (see Figure 9). At $P_e = 1$, all the emitted electrons are used to maintain the electron current at the cathode $(\Gamma_{ew} = \nu_e)$; since Γ_{ew} cannot exceed ν_e, $P_e = 1$, is a necessary condition for cathode saturation. The current-voltage characteristic here cannot saturate in the strict sense of $V_{sh} \rightarrow \infty$ at some limiting current density. Saturation is delayed because the Shottky effect on electron emission is included and as V_{sh} becomes large, the electric field at the cathode surface shows a corresponding increase in magnitude, see Figure 9; this extra emission increases the limiting current density and destroys true saturation. However, the limiting current density is only a weak function of E_w, so that V_{sh} increases very rapidly on the steep part of the characteristic, and for practical purposes, we define a limiting current density, J_L, as the value of current density $(-J_t)$ at which $V_{sh} = 10$ v. We shall call J_L the thermionic limit for the cathode.

The ambipolar voltage drop slowly increases with current density until the knee of the V_{sh} versus J_t curve is reached, then slowly decreases. At low current densities, V_{am} dominates the electrode voltage drop, while near J_L, the sheath drop dominates.

Figure 10 displays the composite solutions for the electric field and the number densities (normalized by their values in the bulk plasma) of the charged species as a function of distance from the cathode (y_P) on a log-log plot at $(-J_t) = 8.4$ amps/cm.^{2}, a value on the knee of the V_{sh} versus J_t characteristic. The values at 10^{-5} cm are less than 6 per cent different from the values at the wall, so the sheath behavior is practically all shown. Note the great increase in electric field strength in going from the bulk plasma toward the cathode.

For reference, the value of the Debye length, $h_{e\infty}$, is shown on Figure 10. Note that it is almost two orders of magnitude smaller than the sheath region. This does not violate the use of Debye length as the characteristic length scale for charge separation because the number densities in the sheath are orders of magnitude smaller than in the bulk plasma,and a "local" Debye length based on some average value of number density in the sheath gives the correct order of magnitude for sheath thickness. However, several authors in the literature have justified the use of "free-fall" sheath models because $h_{e\infty}$ is much less than a mean free path, λ. For the type of plasma studied here, $h_{e\infty}$ is less than $\lambda \simeq 10^{-4}$ cm (for ions), but the sheath thickness is $O(10^{-3}$ cm) so that the sheath here is closer to the collision dominated limit than it is to the collisionless limit.

Figure 11 presents the atom and ambipolar diffusion solutions for N_a and N as a function of y_p with $(-J_t)$ as a running parameter. Note that as $(-J_t)$ rises, the ambipolar diffusion region becomes thinner. This occurs because the electron temperature rises with $(-J_t)$ and this change causes an increase in the magnitude of the production term in the ambipolar diffusion equation. This increase in production expands the region in which the number densities of charged particles are near their values in the bulk plasma. Thus, the region in which $N < 1$ shrinks.

The region of atom diffusion stays at about a constant thickness as $(-J_t)$ is varied. This lack of change occurs because the atom diffusion problem is convection dominated. However, the magnitude of N_a within the region rises rapidly with an increase in $(-J_t)$. This change occurs because the ion flux to the wall increases markedly due to the increase of ionization in the ambipolar diffusion region; the slope of N_a at the wall must become steeper due to its dependence on Γ_{iw} and this requires N_{aw} to increase.

Sheath Structure. Figures 12a - 12e display the structure of the sheath (N_i, N_e, and E as a function of y_p) for values of the parameter $(-J_t)$ extending from 1 to 11 amps/cm.^{2}. At low current densities, the electric field changes direction at some distance from the wall (see Figure 12a), while at higher $(-J_t)$ the electric field becomes large and negative throughout the sheath. In Figures 12a - 12c, $(-E)$ exhibits a maximum in the center of the sheath; this is due to the double-sheath nature with excess electrons near the cathode, while ions are in excess near the ambipolar limit. Poisson's equation requires that the maximum in (-E) occurs at the crossover point in the double sheath where $N_e = N_i$.

The sheaths in Figures 12a - 12c are relaxation-type sheaths, while the sheaths in Figures 12d and 12e are of the diffusion type and would occur even if $N_{iw} = N_{ew}$ (sheath types are discussed in Section 2.5).

If $(-J_t)$ is equal to or greater than the value at the knee of the V_{sh} versus J_t curve, the electrons are transported away from the cathode almost as fast as they are emitted from the cathode ($P_e \simeq 1$); here, ions are in excess throughout the sheath (see Figures 12d and 12e). As the thermionic limit is approached, the cathode voltage drop increases, and this excess voltage results in a thickening of the sheath region and a rapid increase in $(-E_w)$, see Figure 12e.

The boundary conditions on number densities for the sheath, the ambipolar, and the atom diffusion problems are presented in Figure 13 as a function of $(-J_t)$. For low values of $(-J_t)$, N_o (the inner boundary condition for the ambipolar problem) has a value about halfway between the values of N_{ew} and N_{iw}. As $(-J_t)$ becomes larger, N_o and N_{ew} decrease fairly quickly. As the thermionic limit is approached, N_o goes to zero followed by N_{ew} for the same reason given above that the sheath becomes of the ion type. As N_o goes to zero, the electric field in the ambipolar region becomes greater and hence V_{am} increases. However, after N_o has reached zero, the ambipolar electric field rises slower and the shrinkage of the ambipolar region (see Figure 11) dominates, so that V_{am} slowly decreases as the thermionic limit is attained. N_{aw} increases rapidly with $(-J_t)$ as expected from the discussion on the atom diffusion solutions.

To elucidate the effect of the surface-plasma interaction on the thermionic limit, we define a cathode augmentation ratio, $A_t \equiv \nu_e/\nu_{eZ}$, where ν_{eZ} is taken as the electron emission rate for zero electric field at the surface and zero ion flux to the cathode. Two effects operate to increase A_t: 1) the Schottky effect, which is due to large electric fields in the sheath; and 2) the increase in coverage due to the ion flux, which is controlled by the ambipolar region.

To separate these effects, a Schottky augmentation ratio, A_E, is defined as the increase in electron emission just due to the electric field effect, namely, $A_E = \exp\left(\frac{e\Delta\phi}{kT_w}\right)$, where $\Delta\phi$ is the Schottky correction given by equation (20).

These augmentation ratios are shown in Figure 14 as a function of $(-J_t)$. Note that at the thermionic limit, $J_L = 14$ amps/cm.^{2} for this case, A_t has grown to a value of 3.2. The Schottky effect only accounts for about 30 per cent of this 320 per cent increase, so the dominant effect here is the rise in coverage due to Γ_{iw}. The ion current density to the cathode, $(-J_{iw})$, and the degree of coverage, θ, are also displayed in Figure 14. Although $(-J_{iw})$ is small compared to $(-J_t)$, it is an order of magnitude greater than the ion current in the bulk plasma. This is due to convection and ionization effects in the ambipolar diffusion region. This increase in $(-J_{iw})$ causes the rise in θ which explains the large value for the cathode augmentation ratio.

The effect of cathode surface temperature on the thermionic limit is shown by displaying the augmentation ratios and the voltage drops as a function of $(-J_t)$ in Figures 15, 16, 17, and 18 for T_w = 1400, 1600, 1800, and 2000 °K. Note that for T_w = 1400 and 2000°K, the behavior is similar to that of the T_w = 1500°K case discussed above, i.e., a thermionic limit is reached where the Schottky augmentation is about 30 per cent.

However, for T_w = 1600 and 1800°K, V_{sh} increases, but instead of showing saturation behavior, V_{sh} then decreases at higher values of $(-J_t)$. At the top of the V_{sh} "hump," A_t rises so fast with $(-J_t)$ that the saturation behavior is destroyed. The electron current fraction, P_e, is also shown in Figure 16, and as expected does not come too close to the critical value of unity.

Thermionic Regime. A more lucid picture of the effect of T_w on the thermionic limit is given by Figure 19, where T_w is plotted as the independent variable. The reference electron current density, $J_{eZ} = e\nu_{eZ}$, lies toward the bottom of the graph. As T_w increases, J_{eZ} reaches a local maximum and then decreases because the rise in atom evaporation from the surface reduces θ, which decreases J_{eZ} even though T_w is increased. At large values of T_w (> 2200°K), θ is almost zero and J_{eZ} advances with T_w in the normal exponential manner characterized by the work function of pure tungsten. The J_{eZ} versus T_w curve is analogous to the electron emission S-curve (see Section 2.3), except that the seed fraction is the constant parameter on Figure 19 instead of the atom evaporation rate, since $\nu_a(\theta) = \epsilon_k n_c(T_w)\bar{C}_a(T_w)/4$ is the condition that specifies $J_{eZ}(T_w)$. The maximum possible thermionic electron current density (cathode about 65 per cent covered with seed) is also shown (as "K limit") on Figure 19.

Points for J_L (the thermionic limit) taken from current-voltage characteristics are shown on Figure 19 as triangles. These points account for both the sheath and the ambipolar effects in the proper manner. The exact points for J_L are compared in Figure 19 with curves for J_L^* (the thermionic limit without the Schottky effect) and for $J_L^{30\%}$ (the thermionic limit obtained by setting $A_E \equiv 0.3$). As expected from the above discussion on Schottky augmentation, the exact points for J_L fall very nearly on the $J_L^{30\%}$ curve.

Since the ion flux through the sheath region is constant (see Section 2.5), the coverage of the electrode is independent of the sheath solution (unless the sheath is very thick). Hence, J_L^* and $J_L^{30\%}$ can be found, without the rather lengthy (and expensive) sheath calculations, by the following procedure. We set $N_o = 0$, since we are looking for saturation solutions (see Figure 13), and solve the ambipolar, atom, and surface problems. For each value of $(-J_t)$, we can compute a value for P_e^* (the electron current fraction without the Schottky effect). A value for J_L^* is found when the saturation criterion, $P_e^* = 1$, is satisfied, while the proper criterion for $J_L^{30\%}$ is $P_e^* = 1.3$. A typical example of a P_e^* versus $(-J_t)$ plot with T_w as a running parameter is shown in Figure 21. Note that for certain values of T_w (such as 1900°K) the saturation criteria are satisfied by more than one value of $(-J_t)$. For these temperatures, the thermionic regime is divided into a high current density and a low current density region. Figure 21 indicates that the greater the difference in the critical current densities, the larger P_e^* becomes, and hence the greater the sheath drop must become to surmount this barrier.

The thermionic regime is delineated (economically) by solving J_L exactly at a few values of T_w from which a mean value of the Schottky effect is found (30% in this example). The approximate thermionic limit ($J_L^{30\%}$ here) is then found at a large number of values for T_w. This procedure is insensitive to the deviations from the mean Schottky effect if $(-J_t) > 1$ amp/cm.^{2},for the coverage effect then dominates the Schottky effect.

The significance of the thermionic regime graph, Figure 19, for cathode operation is the following: a cathode can be operated with a sheath voltage drop on the order of one tenth of a volt if its surface temperature and current density define a point between the J_L^* versus T_w curves of Figure 19; if the (J, T_w) point lies between the J_L^* versus T_w curve and the neighboring $J_L^{30\%}$ versus T_w curve, V_{sh} is $O(1$ volt); if the (J, T_w) operating point is on the outside of the $J_L^{30\%}$ versus T_w curves (designated by cross-hatching), V_{sh} is around 10 volts (since the J_L points are close to the $J_L^{30\%}$ versus T_w curves). The current-voltage characteristics show that for a J versus T_w curve extending into cross-hatched regions, V_{sh} rapidly increases to hundreds of volts. These large voltage drops might not actually occur in an experiment,for physical processes such as large electron heating and non-thermal ionization become important at high voltages.

Cross Section Dependence. The modification of the thermionic limit (which is approximately given by $J_L^{30\%}$ versus T_w curves) is indicated in Figure 20 by comparing the $J_L^{30\%}$ versus T_w curves calculated for the different combinations of cross section values specified in Section 2. 8. The greatest change occurs around J = 9 amps/cm.^{2} , where the $J_L^{30\%}$ versus T_w curves "neck together." For the average combination, the $J_L^{30\%}$ versus T_w curves coalesce to split the thermionic regime into a high current density and a low current density region at all values for surface temperature.

D_i for the large combination is about one fourth of the value for the mixed combination, while D_a remains the same; since D_i controls ambipolar diffusion, the decrease in D_i reduces the ion flux to the cathode, which results in a smaller electron emission rate. This lowered emission explains the extra necking in of the large combination thermionic limit curves. D_i for the average combination is only decreased to 0. 4 of the value for the mixed combination, but D_a is increased by 60 per cent, and since the atoms can diffuse away from the surface faster with a higher D_a, the coverage effect becomes smaller; this reduction causes the merging of the $J_L^{30\%}$ - T_w curves for the average combination. From the discussion in Section 2. 6 and equation (88), the electron emission rate is roughly proportional to $\sqrt{D_i}/D_a^{2/3}$.

Seed Fraction Effect. A thermionic regime graph calculated under the same conditions as the one in Figure 19 except that ϵ_k = .002 is displayed in Figure 22. The J_{eZ} versus T_w curve for

$\epsilon_k = .002$ is more than halved, around its hump, from the $\epsilon_k = .004$ case. The lower boundaries of the $J_L^{30\%}$ versus T_w curves are decreased by about the same amount as the reference current density curve is, while the upper boundaries are just slightly altered from the $\epsilon_k = .004$ case. The channel region where the thermionic limit curves "neck together" is considerably decreased in width from the higher seed fraction case.

The current-voltage characteristic for $T_w = 1600^oK$ and $\epsilon_k = .002$ is shown in Figure 23. This case corresponds to a T_w just within the narrow channel of the thermionic regime graph of Figure 22. The ambipolar voltage drop has about the same value and behavior as the cases presented above. As for $\epsilon_k = .004$, the sheath drop is small when the current density is not close to a saturating value. For values of current density in the channel region of Figure 22, saturation is approached as V_{sh} increases to a maximum of about 20 volts and the Schottky effect to 26 per cent. V_{sh} then decreases to a low value as the high current density thermionic region is entered.

The calculation of $J_L^{30\%}$ with $\epsilon_k = .002$ and large cross section values is compared with the mixed combination in Figure 24. The large combination closes the channel dividing the thermionic regime into high and low current density regions. The boundaries away from the channel region are similar for the two cases.

Ambipolar Limiting Solutions. The ambipolar diffusion solution is characterized by I/δ, and the ambipolar region is coupled to the sheath and the surface problems through I. The closed form expressions of Section 2.6 for I/δ are compared with machine computed results in Figure 25. The comparison is made by using the value of N_o found by the sheath matching and by evaluating the closed form solutions at the mean film temperature. As expected from the discussion in Section 2.6 on dominant terms, the hybrid case solution has the same trend as the machine solution (for $N_a \equiv 1$) at high values of $(-J_t)$ while the frozen inviscid case solution has the correct trend at low values of $(-J_t)$. The agreement of the hybrid case solution with the ($N_a \equiv 1$) machine solution is within 3 per cent, which shows that the variation in transport coefficients through the ambipolar region has a small effect on I/δ. The agreement of the frozen inviscid case solution at small $(-J_t)$ is only within 20 per cent because the velocity profile is approximated here as well as the transport coefficients. The viscous velocity profile does not improve the agreement at small $(-J_t)$, for the ambipolar region is thicker than the viscous boundary layer at low current densities. The extra ionization due to the additional atoms near the cathode causes I/δ to increase, a fact accounted for by the exact machine solution. Figure 25 indicates that the N_a term becomes important for $(-J_t) > 6$ amps/cm.^{2}. Below this value, the ambipolar diffusion region is much thicker than the atom diffusion region (see Figure 11), so that $N_a \approx 1$ throughout most of the ambipolar region. For the other cross section combinations (large and average), D_a and D_i are nearly equal, which implies that the ambipolar region is of the same thickness or thinner than the atom diffusion region, so that the N_a term is more important for these cases than for the mixed combination.

When $R = \omega$, then $(-J_t) = 2$ amps/cm.^{2} and the frozen case underestimates I/δ by about 40 per cent. A similar error occurs in the frozen atom diffusion solution for N_{aw} when $R = \sigma\omega$, which occurs at $(-J_t) = 20$ amps/cm.^{2}. The effect of the production term on atom diffusion is as a sink for atoms,and the number density of atoms near the wall will decrease. Hence, the solution for I/δ will not in-increase as rapidly above $(-J_t) = 20$ amps/cm.^{2} as the exact machine solution of Figure 25 suggests. For $(-J_t) >> 20$ amps/cm.^{2}, the behavior approaches that of the stagnant case discussed in Section 2. 6, in which the finiteness of the cathode-anode spacing distance becomes important.

The curves for P_e^* in Figure 21 do not account for the production term on atom diffusion and show no trend toward saturating at higher current densities for surface temperatures greater than 1500°K. The ionization at the larger values of $(-J_t)$ becomes so great that the ion flux to the cathode accounts for a substantial portion of the total current density. This effect is only limited by complete ionization of the seed (which does not occur until $(-J_t) > 100$ amps/cm.^{2}).

Whether the high current density region of the thermionic regime is limited by complete seed ionization or nearly complete coverage of the cathode with seed will have to be determined by including the production term for atom diffusion.

Anode-Cathode Characteristic. A current-voltage characteristic for $T_w = 1500^\circ$K and $\epsilon_k = .004$, computed with the large combination of cross section values for both positive and negative values of J_t, is shown in Figure 26. The ambipolar voltage drop, V_{am}, dips to a low value near $J_t = 0$. This dip occurs because N_o rises sharply near $J_t = 0$, decreasing the electric fields in the ambipolar region, and hence V_{am} is reduced. The sheath voltage drop on the anode side of the current-voltage characteristic does not show saturation behavior to large negative voltages; the anode voltage drop becomes positive and remains nearly constant for large values of J_t. This anomalous behavior occurs because of the rise in ionization as $|J_t|$ increases. The extra ionization augments the ion flux near the anode so that saturation for this electrode does not occur over the current density range considered here. Since the ion emission rate has about the same or larger values at surface temperatures other than the one used for this calculation ($T_w = 1500^oK$), the anode behavior is of secondary interest here.

The cathode part of the current-voltage characteristic exhibits peculiar behavior, as this value of T_w is near the channel region of the thermionic regime (see Figure 20). The Schottky effect is 34 per cent at a sheath voltage drop of 10 volts, and this justifies the use of the $J_L^{30\%}$-T_w curves to approximate the thermionic limit for the large combination of cross section values. As J_t becomes more negative, the sheath voltage drop rises to about 21 volts, then decreases and levels out to a value around 10 volts. This behavior is required to produce the Schottky effect implied by the P_e^* curve for $T_w = 1500^oK$ in Figure 21.

The ambipolar voltage drop behaves similarly with the above cases for the mixed combination of cross section values, but at values about 30 per cent smaller. This reduction in V_{am} is due to the "shrinkage" effect discussed earlier in this section. Since the ambipolar region scales as $(D_i^{-\frac{1}{2}})$ and D_i is now one fourth of the mixed combination value, the ambipolar region extends only about 50 per cent of the value for the mixed combination. V_{am} is not decreased the full 50 per cent because of the slow rise of the electric fields in a thinner ambipolar region.

Conclusions. The interaction of a seeded plasma with a cathode can augment by an order of magnitude the thermionic limit computed from the high density S-curves (J_{eZ} - T_w curves). Cathodes can be operated in the thermionic mode in a low current density region of the thermionic regime which is sensitive to the J_{eZ}-T_w curve, or a high current density region which starts at around $T_w = 1500^\circ K$ and $(-J_t) = 10$ amps/cm.^{2}. Depending on the parameters, a channel for thermionic operation connecting the high and low current density regions may exist at around $T_w = 1600^\circ K$; the existence and width of the channel are sensitive to the seed fraction and the diffusion coefficients for ions and atoms.

For $(-J_t) < 1$ amps/cm.^{2}, the Schottky effect (due to large sheath electric fields) is the dominant cause of augmentation and increases the electron emission from the cathode by about 30 per cent. Above $(-J_t) = 1$ amps/cm.^{2}, the dominant effect is the rise in coverage of the cathode with seed particles. The coverage effect can augment the cathode electron emission by over a factor of ten. The coverage effect becomes important at large current densities here because in this type of non-equilibrium plasma, the electron temperature rises significantly with an increase in current density: this increased electron temperature speeds up the rate of ionization of seed particles which produces an enlarged ion flux to the cathode, thus coating it with seed particles.

For the same reasons, a large ion flux is produced at the anode which delays any saturation effect for this electrode in the current density range considered here.

The trends of the solutions found here imply that the high current density region is only limited by nearly complete coverage of the cathode or by total seed ionization.

III. EXPERIMENTAL APPARATUS AND TECHNIQUES

The basic apparatus used to supply a seeded plasma of uniform properties to a test section is illustrated schematically in Figures 27 and 28. This apparatus was described in detail in reference 28, and only the essential features and modifications will be discussed here. The primary flow of argon, 2.0 gm/sec, was heated by a 10 kilowatt arc-jet heater which could be adjusted to give gas temperatures at the test section from 1250 to 2250°K. The arc-jet heater was water-cooled and made of copper, except for a tungsten insert which acted as the cathode. No sputtering of either material was observed.

A smaller (<.15 gm/sec) secondary flow of argon was saturated with potassium vapor by bubbling it through a potassium bath regulated at a temperature of 810°K; this flow was injected into the main flow just after the arc jet. By adjusting the secondary gas flow rate, the fraction of potassium atoms to the number of argon atoms, n_K/n_A, in the combined flow was varied from .0005 to .006.

The two streams were allowed to come to equilibrium in a mixing chamber which consisted of a 2.2-cm I.D. by 20-cm long alumina tube encased in a stainless steel jacket and surrounded by a radiation shield. The uniform seeded plasma was then passed through the test section and exhausted at one atmosphere into an exhaust duct system.

The two types of test section used are shown in Figures 29 and 30. The test sections were fabricated from boron nitride pieces held together by pins and close fits. The working section was 1.16 cm in diameter by about 9.5 cm in length in both types. Voltage probes were made from tungsten rod .0635 cm in diameter and connected externally through thin copper strips silver-soldered to the tungsten. In each type of test section, the voltage probes were separated by 1.9 cm and usually positioned 1.9 cm from the cathode. An annular stainless steel anode was placed upstream in both types. The spiral cathodes in Figure 29 were made from rods of diameter from .051 to .152 cm and spot-welded to a bracket. The spiral cathode surface was viewed through the exhaust.

The stagnation flow plate cathode of Figure 30 was fabricated by a spark cutter and the surface was finished with a surface grinder and by mechanical polishing. It had the same diameter as the working section, 1.16 cm. This cathode surface was viewed through quartz windows set in cells made of alumina tubes which were purged with a small flow of argon. The disc cathode (also shown in Figure 30) was spot-welded together.

Total pressure surveys were made across a test section diameter with a micro-manometer and indicated a flat profile over about 80 per cent of the diameter. At a measured gas temperature of $2000^{\circ}K$, the velocity at the flat part (reduced from the total pressure) was about equal to 10^4 cm/sec. The flat profile was due to the converging section just upstream of the test section.

The discharge circuit (shown in Figure 31) consisted of a 4.6 kilowatt constant current generator connected in series with a small (.022 ohm) resistor and the test section electrodes. For currents above 40 amperes, capacitors were discharged for several milliseconds, as by Cool(28).

3.1 Measurement Techniques

The gas temperature was measured by correcting the output of a small (.0635 cm bead diameter) tungsten-tungsten rhenium thermocouple for heat transfer. The gas temperature obtained by this method agreed to within 5 per cent of the value obtained by the thin wire technique of Cool(28).

The potassium seeding system was calibrated by passing the secondary flow through a condensation tube and weighing the condensed potassium at set time intervals. The average weight of the condensate was about 10 per cent higher than the value predicted by equilibrium with the potassium vapor pressure at the potassium bath temperature. The condensate weight varied from the average weight by ± 15 per cent due to the high sensitivity of potassium vapor pressure to bath temperature. The sporadic appearance of a black contaminate in the potassium system was eliminated by a procedure discussed in Appendix D.

Voltage Probes. The mean electric field was obtained by measuring voltage differences between floating voltage probes. This method will give the correct electric field if the probes are operated in the same environment so that the probe voltage drops are equal. Cool(12) established that the electric field along the duct was constant by using six voltage probes. The uniformity of the electric field was monitored here by using three probes. Since the electric field in the plasma column was uniform, the cathode voltage drop was found by measuring the voltage at a probe and extrapolating by the electric field to the cathode surface. The simple analog computer circuit, shown in Figure 31, allowed the direct recording of the cathode voltage drop. The recorded cathode drop did not account for field fringing or the floating probe voltage drop. The measured cathode drop was corrected for the probe drop by the following approximate analysis.

The rigorous solution of a cylindrical probe (by the techniques of Part II) for the floating potential involves a complicated current density pattern as current may flow through the probe even though it is floating. If the sheath voltage at some point on the probe surface tends to rise, the current flow will readjust to decrease the current flowing at that point so that the probe surface will remain an equipotential surface. The probe voltage drop associated with the current density pattern in the outer solution is on the order of $E_\infty D_p$, where D_p is the probe diameter. The ambipolar voltage drop contains a term that does not depend on the current density; this is the second term in equation (46) and can be integrated directly, to $O(10^{-3})$, to give for the current density independent component of the ambipolar drop: $V_{amZ} = kT_e \ell n \frac{n_{e\infty}}{n_o}$. Within an error on the order of $E_\infty D_p$, the probe voltage drop is given by the zero current density ambipolar drop, since the current density pattern can readjust in order to maintain the current density dependent component of the probe drop below $E_\infty D_p$. Rigorously, n_o is found by matching to the sheath solution, but the numerical results in Section 2.9 indicated that $n_o \approx \frac{1}{2}(n_{ew}+n_{iw})$ for low current densities; the error in the coefficient, $\frac{1}{2}$, for the n_o calculation is not important, as V_{amZ} only depends on it logarithmically. The increase in coverage due to ion flux to the surface is only one tenth as important for the probe as it is for the cathode because of the smallness of the probes considered here (see equation (88)). Thus, it is consistent to evaluate n_{ew} and n_{iw} by the approximation that the fluxes to the surface are zero. The probe correction voltage, V_{amZ}, calculated by the above method, is presented in Figure 31 as a function of $|J_t|$ for various values of the parameters ε_k and T_p. The measure, $E_{\infty}D_p$, of the error in the voltage correction is also shown in Figure 32. The voltage correction increases with $|J_t|$ because $n_{e\infty}$ rises rapidly with current density. V_{amZ} for $T_p = 2000^\circ K$ is well below the values for lower probe temperatures because the probe surface is only slightly covered with seed and acts as a strong surface ionizer of seed particles. This ionization increases n_{iw} considerably, which causes the reduction in V_{amZ}. For $V_{amZ} > 0$, the probe is at a lower potential than the adjacent plasma so that the corrected cathode drop is found by adding V_{amZ} to the measured cathode drop.

Surface Temperature. The surface temperature of the cathode was measured by the optical system illustrated in Figure 33. Radiation emitted from a portion of the cathode surface was selected by a collimating tube and conducted through a light pipe made of plastic optical fibers to a photomultiplier tube. The plasma radiation was eliminated by a Kodak Wratten 87C filter which transmitted only the infrared radiation from the cathode. The photomultiplier tube was cooled to dry-ice temperatures to remove thermal noise from the tube output, and condensation in the optical system was prevented by purging with dry, high-purity nitrogen. The optical system was calibrated by measuring the brightness temperature (at 6500 Å) of a tungsten surface with a conventional optical pyrometer (calibrated against a NBS standard lamp). The true temperature was found from the brightness temperature by using the emissivity values for tungsten. The change in emissivity due to a partial coverage of the tungsten surface with potassium was neglected, as this correction would alter the true temperature by less than 5 per cent.

Photography. Close-up photographs of the cathode surface were taken with a Graphic View camera at a shutter speed of 1/400 second.

Surface Preparation. The cathode surface was cleaned by washing it in a hot potassium hydroxide solution followed by a methanol rinse. The arc-jet system was run for thirty minutes before data were taken, so that surface layers of impurities were removed by the hot argon environment surrounding the cathode surface.

IV. EXPERIMENTAL RESULTS AND COMPARISON WITH THEORY

In this part of the thesis, the experimental results are presented and then compared with the above theory. First, the general characteristics of the observed electrode phenomena will be presented. Next, experimental data for the limiting cathode voltage drop and cathode current density at which the thermionic mode of cathode operations is no longer possible will be displayed. Finally, the experimental data will be compared with the theory developed in Part II and the validity of the Levine and Gyftopoulos surface adsorption and emission correlation will be discussed.

4.1 Typical Characteristics of the Electrode Phenomena

The experiments were performed by setting the seed fraction (ϵ_K) and the gas temperature ($T_{n\infty}$), which determined the velocity (u_∞), since the mass flow rate was held constant; the current through the discharge was adjusted by the constant current generator, and the cathode voltage drop (V_c), the cathode surface temperature (T_w), the average electric field (E_∞), and the current were recorded on strip chart recorders as functions of time. The current was varied slower than 10 amperes per second, which allowed all processes to reach quasi-equilibrium except for heat transfer. In practice, the cathode surface temperature was controlled by the current sweeping time, the dimensions of the cathode support rod, and the gas temperature.

Typical strip chart data are displayed in Figures 34a and 34b. In Figure 34a, the cathode surface temperature rises as the current increases in time, while the measured cathode voltage drop slowly advances to about six volts, then falls off at the higher currents. The fluctuations in the data are small throughout the current sweep. From the strip chart data, the average values of temperature and voltage were reduced (V_{cath} was corrected for probe error, but not field fringing) and plotted versus the cathode current density (J_{cath}), which is defined as the current divided by the total wetted surface area of the cathode; this type of plot for the data in Figure 34a is shown in Figure 35a.

A visual observation of the cathode during the experiment shown in Figure 34a revealed a uniform radiation pattern at the surface and the surface appeared fuzzy.

The behavior exhibited by the recordings shown in Figure 34b is quite different. As the current increases, the voltage drop continues to increase until a critical value is reached at which it jumps to a lower value. The fluctuations in voltage drop become large, and there are corresponding fluctuations in the current and temperature recordings. At higher currents, the fluctuations suddenly cease and the voltage drop decreases, as in Figure 34a. The current-voltage characteristic with the surface temperature also for this experiment is shown in Figure 35b.

A visual observation of the cathode during the experiment shown in Figure 34b disclosed the presence of a small arc (arclet) during the highly fluctuating portion of the recordings in Figure 34b. The arclet extended for about 0. 04 centimeters from a small spot on the cathode surface into the bulk plasma. The rest of the cathode surface appeared in great detail, as if it had been lit up by a flashbulb. When the arclet first formed, the cathode voltage drop showed a sudden dip, and a loud popping noise was heard.

At the beginning of an experiment with a new cathode, an arclet would form at random positions on the cathode, exist on the order of a second, die out, and reappear at a new position. The appearance of the arclet was accompanied by the popping noise and large recorder fluctuations. As the experiment progressed, the arclet or arclets would remain at preferred locations (usually a sharp edge or some imperfection such as a crack) for an indefinite period of time. An examination of the cathode after the experiment disclosed that the preferred location for the arclet had a very shiny, silvery appearance, while the remainder of the cathode surface was discolored to a dull light grey. This indicates that the arc spot has a temperature of at least 2400°K, for it is well known that a tungsten surface "flows" above this temperature to produce a shiny surface(31).

Arclet Photographs. The close-up photographs of the 0.152 centimeter spiral cathode displayed in Figure 36 were taken during the arclet mode of operation. The relationship of the photographs to the current-voltage characteristic is indicated on Figure 37. The arclets are clearly visible on the photographs as bright regions adjacent to the cathode surface. As the current through the cathode was increased, the photographs show that the arclets enlarged in surface area, but not in distance from the surface.

The experiments on the 0.076 centimeter spiral cathode revealed that the arclets were smaller and more numerous than for the above case. A typical voltage-current characteristic for this cathode is shown in Figure 38.

Arclet Effect on Bulk Plasma. By changing the surface temperature and the area ratio of the cathode to the duct cross-sectional area, the arclet mode occurred at a wide range of values of bulk plasma current density. The bulk plasma electric field was independent of the cathode type or mode of operation.

In general, the arclet mode (when steady) is characterized by a decreasing voltage drop (but always higher than 4 volts) with increasing current and by much larger heat transfer rates,as indicated by the large temperature rises in the arclet mode. This change in heat transfer rate produces a hysteresis effect when current is decreased from a value in the arclet mode.

A typical hysteresis loop is shown in Figure 39 for a disk cathode. The hysteresis in temperature caused the cathode to operate in the arclet mode (as the current was reduced) to a smaller value of J_{cath} than the value at which the arclet mode started for increasing current. This mode change delay causes a corresponding hysteresis loop for the voltage drop.

The experimental curves shown in Figure 40 were constructed by applying a step function in voltage (from zero) point by point for a 0.051 centimeter spiral cathode. The scatter bars (shown on Figure 40) indicate the increase in scatter near the transition point. Also shown on Figure 40 is the voltage drop at the cylindrical anode. Note that the scatter in the V_{anode} data was constant and small for all values of current, and that V_{anode} behaved regularly even while the cathode was making the transition from the thermionic mode to the arclet mode.

4. 2 Experimental Transition Data

The experimental data for transition between the thermionic and the arclet modes of cathode operation are presented in Figures 41 to 45. A legend for the symbols used on these figures is given by Table 3 in front of Figure 41.

The values for the cathode voltage drop at which the thermionic mode changes to the arclet mode, called the breakdown voltage (V_{bk}), are given in Figure 41 for various seed fractions and cathode types as a function of the cathode current density at breakdown, J_{bk}. Also shown on Figure 41 is a straight line fitted using all the data. Note that as J_{cath} increases, the breakdown voltage is reduced, but that V_{bk} was always greater than the ionization potential for potassium (4. 3 volts).

The values of the cathode current density at breakdown (J_{bk}) are plotted in Figure 42 versus the corresponding cathode surface temperature at breakdown for the seed fraction of . 001 and for other seed fractions and cathode geometries except for the stagnation plate cathode. For reference, the "K limit" current density curve and the reference thermionic electron current density (J_{eZ}) for various values of seed fraction are shown on Figure 42. The values of J_{bk} at which the arclet mode reverts to the thermionic mode, both for current increasing and decreasing, are shown on Figure 42, and the point at which each case originally changed from the thermionic mode to the arclet mode is indicated by a connecting straight line.

All the low temperature ($< 1400^\circ$K) data for J_{bk} are displayed in Figure 43 as a function of T_w. For comparison, J_{eZ} is shown for $\epsilon_K = .001$, $.002$, and $.004$. Note that all the data (regardless of the seed fraction value) fall very nearly on the same curve (indicated on Figure 43). The J_{eZ} curves for all values of seed fraction also merge at low temperatures, and the data curve has very nearly the same slope as the merged J_{eZ} curve although the two curves are separated by about 100 Kelvin degrees. This comparison will be discussed in Section 4. 3.

The stagnation plate data for J_{bk} at a seed fraction of .002 are displayed in Figure 44. For the current sweeps that did not result in a transition out of the thermionic mode, the value of J_{cath} at which V_{cath} attained its maximum value is shown on Figure 44 with the maximum V_{cath} value written out next to this type of data point. The data points are superimposed on Figure 24, the theoretical curves for the thermionic limit at $\epsilon_K = .002$. The data points for transition from the arclet mode back to the thermionic mode for increasing current are also shown on Figure 44 and connected to the first transition point by a straight line.

The stagnation plate data for J_{bk} at $\epsilon_K = .004$ are displayed in Figure 45 in a manner similar to the above data presentation for $\epsilon_K = .002$. For comparison, the data are combined with Figure 20, the theoretical curves for the thermionic limit at $\epsilon_K = .004$. Also shown on Figure 45 are the temperature histories of two current sweeps with the voltage levels written out along the $J_{cath} - T_w$ curves. Note that for the lower temperature current sweep the cathode voltage drop was low at first, rose to a maximum of 5.2 volts, then decreased as the current was increased, staying in the thermionic mode up to $J_{cath} = 30$ amps/cm^2. The higher temperature current sweep, however, resulted in high cathode drops and a corresponding transition to the arclet mode, then a transition back to the thermionic mode as the current was advanced.

4.3 Comparison of Experiment with Theory

Although the theoretical model of Part II predicts large cathode voltage drops, O(1000 volts), as the thermionic limit is approached, the experiments reveal the formation of arclets at a voltage drop on the order of 10 volts (see Figure 41). The analytical solutions of Part II are only possible solutions, not necessarily stable ones, and three-dimensional solutions with a non-uniform surface temperature distribution might exist. Also, non-thermal ionization due to the large sheath drops are not accounted for in the present model. Recently, models using a heat transfer balance at the arc spot on the cathode surface have been proposed by Adams(32) and by Nichols(33). While the results of references 32 and 33 cannot be compared with the arclet data here, they do predict a decreasing cathode drop for increased current, which was observed in the arclet mode.

The model of Part II is compared with experiment by checking the predicted thermionic limit with the experimental arclet breakdown values (see Figures 44 and 45). Note that the thermionic mode was observed in both the low current density region and the high current density region, as predicted. The channel region for thermionic operation around $T_w = 1600^\circ K$ is clearly defined for the $\epsilon_K = .004$ case (Figure 45). The data in the channel region for the $\epsilon_K = .002$ case (Figure 44) are more scattered. This scatter is not surprising in view of the sensitivity of a narrow channel region to a fluctuation in seed concentration and the ± 15 per cent variation in the seed concentration for the experimental arrangement used here. However, all the channel data in Figure 44 indicate high voltage drops in the region predicted. The calculations based on the large combination of cross section values agree best with the $\epsilon_K = .002$ and .004 data. While the $\epsilon_K = .001$ case was not computed, the stagnation plate data for $\epsilon_K = .001$ in Figure 42 agree with the trends for the computed cases; there was no channel region observed as all current sweeps resulted in an arclet formation, and the high current density thermionic region was observed to start at about 10 $amps/cm^2$ and $1500^\circ K$.

A typical experimental voltage-current characteristic is compared with theory in Figure 46 for $\epsilon_K = .002$. The experimental cathode voltage drop has the same behavior as predicted for low current densities with a value about 40 per cent higher than predicted. Part of this error is probably due to the crude approximation for the voltage probe correction factor, which is about 50 per cent here. Note that the experimental curve starts to saturate earlier than the theoretical one and that the experimental curve saturates considerably slower than predicted. These two effects tend to counterbalance so that the agreement of the breakdown data with the computed thermionic limit is better than should be expected. On reason for the reduced saturation rate is electron heating due to the sheath voltage drop. At low values of the sheath voltage drop, the electronic thermal conductivity maintains a nearly uniform electron temperature. At high sheath drops (> 2 volts), the electrons heat up and this results in a greater surface emission due to the extra ionization effect on surface coverage discussed in Section 2. 9.

The experimental data verify that the primary mechanisms for the electrode - seeded plasma interaction are accounted for by the model described in Part II. The experimental results indicate that an important secondary effect (probably electron heating) should be included in a refined theory. The present model predicts the thermionic limit within a factor of two. The above theoretical and experimental results are used in the following to check the validity of the surface model of Levine and Gyftopoulos.

The low temperature ($< 1400^{o}$K) data in Figure 43 fall on the same curve independent of the seed concentration, because the coverage at low temperature approaches a monolayer so that the thermionic emission is independent of the seed concentration. The temperature shift of the experimental curve from the theoretical curve is discussed later in this section.

The high temperature ($> 1600^{o}$K) data points in Figure 42 are not for the stagnation plate cathode, but a crude, simple relation between the thermionic limits for different types of cathode is found from equation (88) for the hybrid case (see Section 2. 6). The relation for the thermionic limits is:

$$J_L \approx J_{eZ} + (J_L' - J_{eZ}) \frac{n_{e\infty}^2}{n_{e\infty}'^2} \sqrt{\frac{L\gamma a'}{L'\gamma' a}} \quad . \qquad (89)$$

The spiral cathode data are greater than the stagnation plate results because although $L' << L$, the ratio of A_{cath}/A_{duct} is greater than one, which implies a higher electron temperature for the spiral cathode data and the increase in $n'^2_{e\infty}\sqrt{\gamma}$ swamps the length effect in equation (89).

The thermionic limit data for $\epsilon_K = .002$ have been reduced by the correction equation (89) and by the theory of Part II to give J_{eZ} as a function of T_w. The resulting reduced experimental curve for J_{eZ} is compared in Figure 47 with the Levine and Gyftopoulos model computed from various values of the surface work function and the seed surface density. The uncertainty in the data and the reduction technique is indicated by the error bars in Figure 47. The best overall fit to the surface model is for $\phi_f = 2.22$ eV and $\sigma_f = 4.8 \times 10^{14}$ atoms/cm^2. The electron emission S-curves are computed with the preceding values for a wide range of temperatures and atom desorption rates and displayed in Figure 48. The only other experimental emission data for a potassium-tungsten system are those of Killian(34) which are in the microamps/cm^2 range. The present data and Killian's data are compared with the Levine and Gyftopoulos model in Figure 48 and provide a check on the model over eight orders of magnitude of current density. The agreement of both sets of data with the model is good on the negative slope portion of the J_e versus T_w curves. However, both sets of data are shifted over by about 100 Kelvin degrees on the low temperature side of the S-curves. This temperature shift rises slightly with an increase in temperature.

A possible explanation for this temperature shift is that second layer effects, which are not accounted for by the model, become important as monolayer coverage is approached (indicated by the low temperature envelope for the S-curves).

It is concluded that the Levine and Gyftopoulos surface correlation compares favorably with potassium on tungsten experiments over a current density range from 0.2 microamps/cm^2 to 5 amps/cm^2. Due to the simplicity of the expressions (quoted in Section 2.3) and the large number of adsorbate - substrate combinations that can be computed, this correlation is of great utility for electrode studies in seeded plasmas.

V. SUMMARY

A theoretical model has been developed which predicts the behavior of thermionically emitting electrodes in contact with a high pressure, non-equilibrium, seeded plasma. The model accounts for the coupling of the adsorption phenomena of alkali metal seed particles onto electrode surfaces with that behavior due to the plasma in the electric boundary layer.

The electrode - seeded plasma interaction is studied by a continuum model of the plasma which includes the fluxes of the seed atoms and ions. Expressions are quoted for the desorption rates of heavy seed particles and for the emission of electrons from the electrode surface. The effect of large electric fields at the surface, due to an electrostatic sheath, on the surface emission is accounted for by the Schottky correction term. The surface emission rates are related to number densities at the surface, so that the plasma problem is well-posed. An iterative scheme is developed for the solution of the electric boundary layer and the state of the electrode surface.

A detailed study of the stagnation electrode is presented, and extensive computer calculations for the argon-potassium-tungsten system are given.

The major result of this investigation is that the ion flux to the cathode surface can greatly enhance the thermionic limiting current density. This enhancement is due to the buildup of seed particles on the cathode surface, since the incoming ion flux must be counterbalanced by the slow outward diffusion of seed atoms. The adsorbed layer of seed particles lowers the effective work function of the electrode surface, which allows the large thermionic emission.

For the non-equilibrium type of plasma studied here, the ionization in the ambipolar diffusion region is important, and this ionization enlarges the ion flux to the cathode, which amplifies the thermionic emission even further.

The Schottky effect increases the thermionic emission by about 30 per cent for the range of parameters studied here. Above about 1 amps/cm^2, the ion flux effect dominates; and for cathode temperatures above 1500°K and current densities greater than 10 amps/cm^2, the thermionic limit is only bounded by nearly complete coverage of the cathode or by total seed ionization.

Below about 10 amps/cm^2, the thermionic mode is restricted to a low current density region which is very sensitive to seed fraction and surface temperature. For certain values of seed fraction a channel may exist, at around a surface temperature of 1600°K, which connects the low current density and the high current density ($>$ 10 amps/cm^2) regions.

Calculations for the anode revealed that the anode voltage drops are small, and no limiting phenomena such as occurs at the cathode is indicated.

Experiments were performed for the stagnation electrode and for spiral electrodes. The experiments revealed that as the thermionic limit was approached, a transition to an arclet mode of cathode operation would occur at some critical breakdown voltage drop. This breakdown voltage was typically 10 volts and increased for lower values of the transition current density. The cathode voltage drops in the arclet mode were higher (> 4 volts) than the voltage drops (typically 2 volts) which occurred in the thermionic mode and the transition from the arclet mode to the thermionic mode was observed.

The experiments on the stagnation cathode agreed with the theoretical predictions and the low current density, the high current density, and the channel regions were observed. The agreement with the computed thermionic limit was within a factor of two, and some important secondary effect (probably electron heating) is indicated.

The surface correlation of Levine and Gyftopoulos (7-10) was checked by computing the S-curves for electron emission by their model and reducing the above experiments by means of the electrode-plasma theory developed here and comparing. The only other known emission experiments on a potassium-tungsten system by Killian(34) were also used. This comparison indicates favorable agreement over 8 orders of magnitude of current density, although there is a 100°K shift from the low temperature envelope of S-curves. This shift could be due to second layer effects.

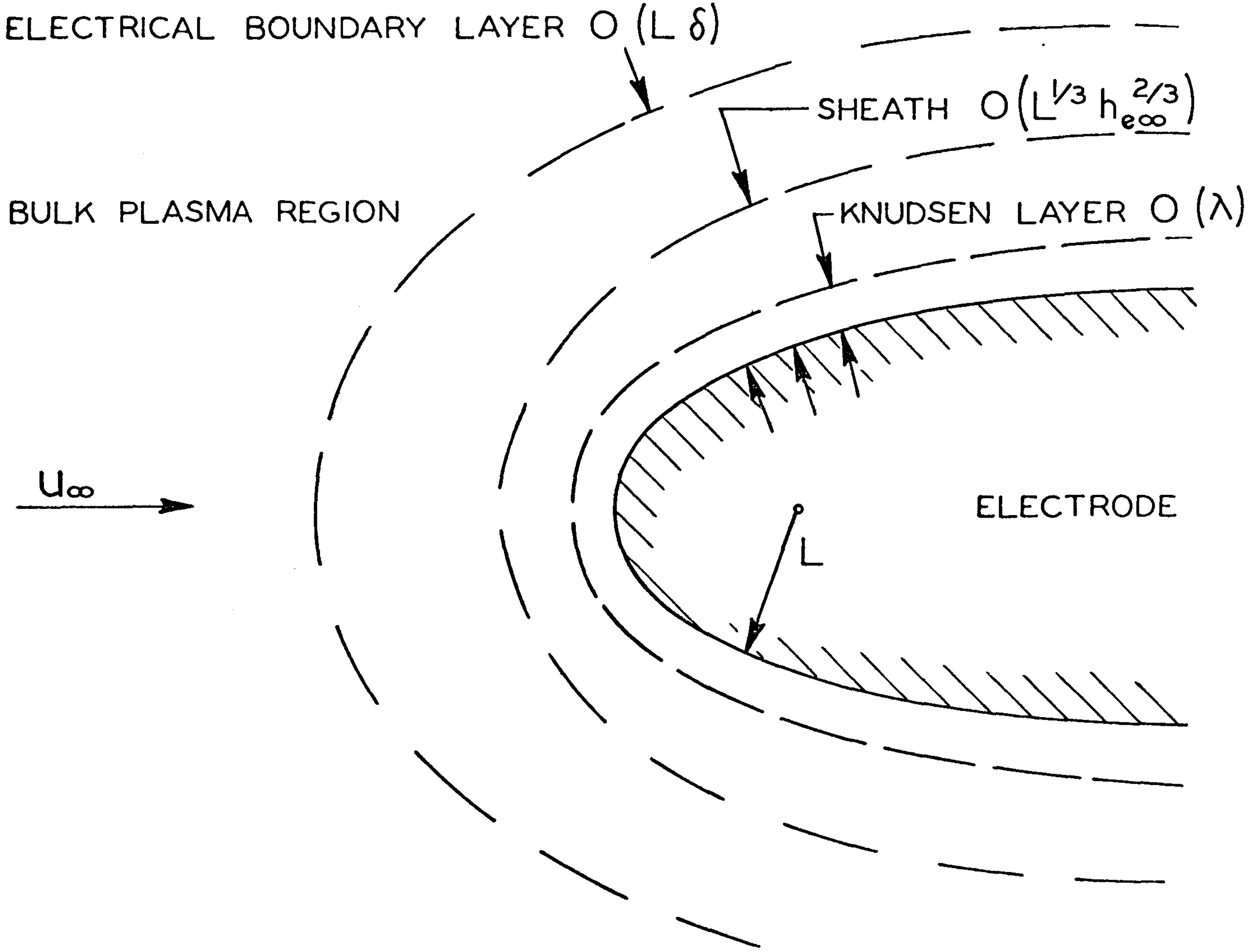

FIG. 1 SCHEMATIC OF ELECTRICAL REGIONS

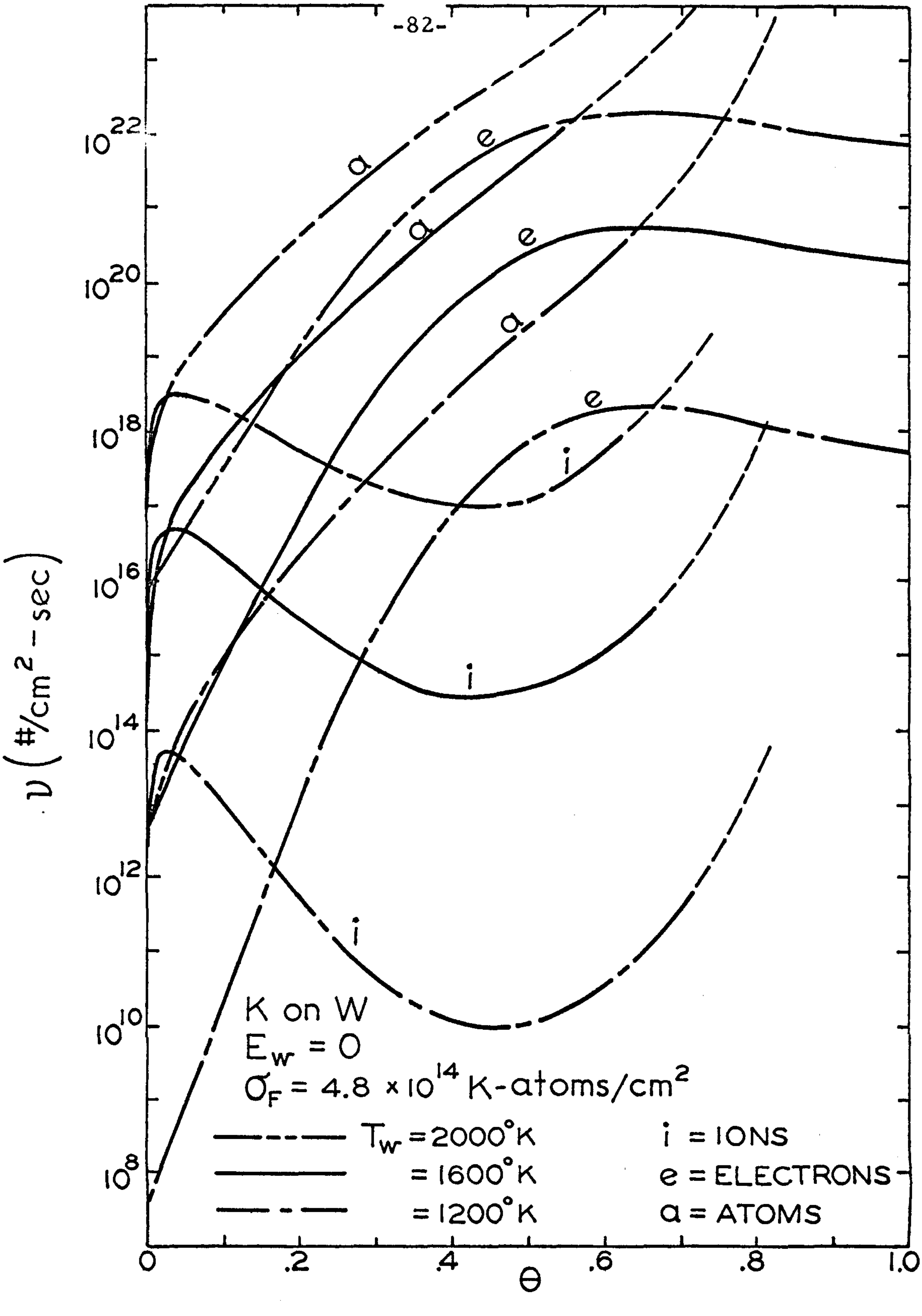

FIG. 2 DESORPTION RATE ISOTHERMS

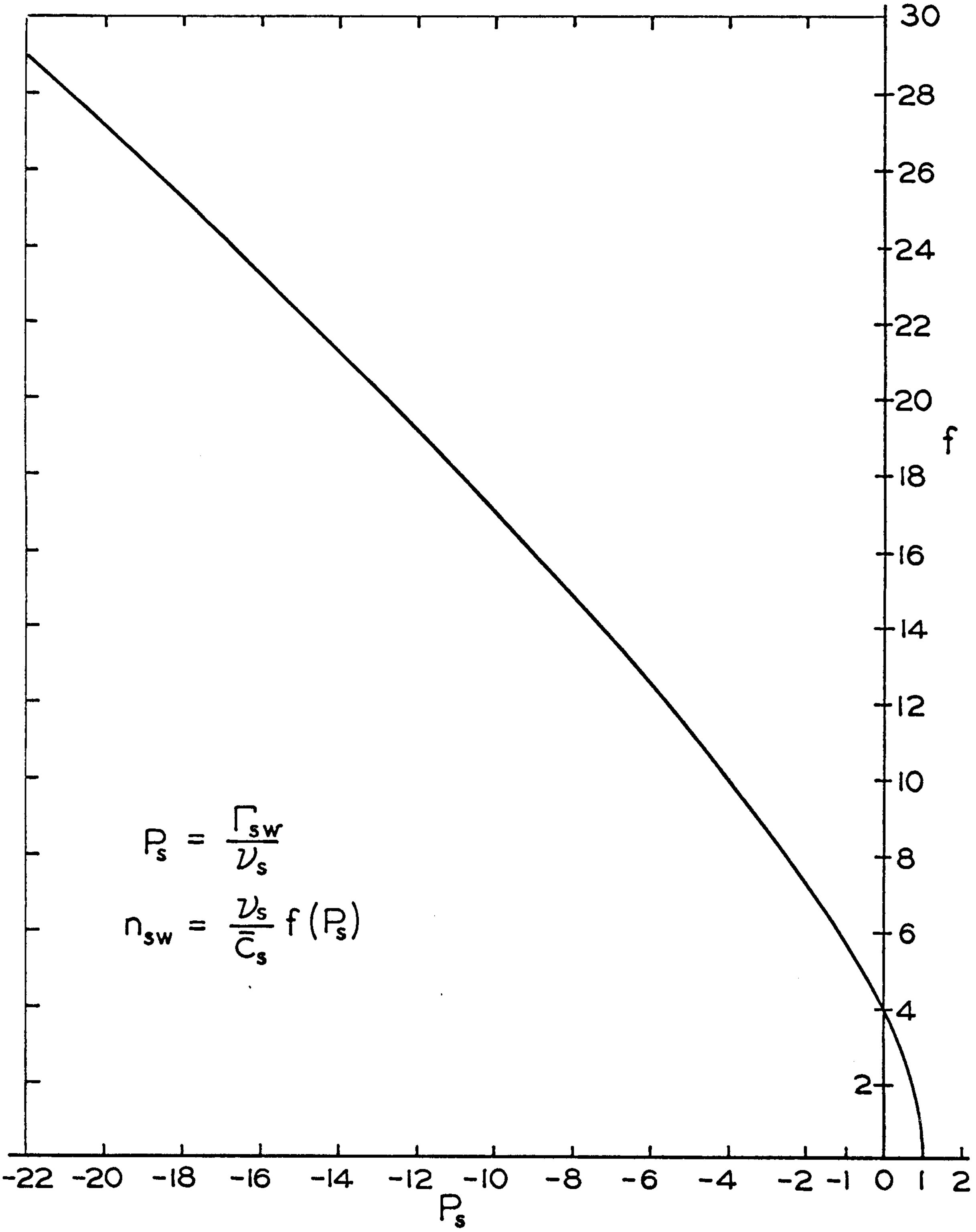

FIG. 3 BOUNDARY CONDITION FUNCTION

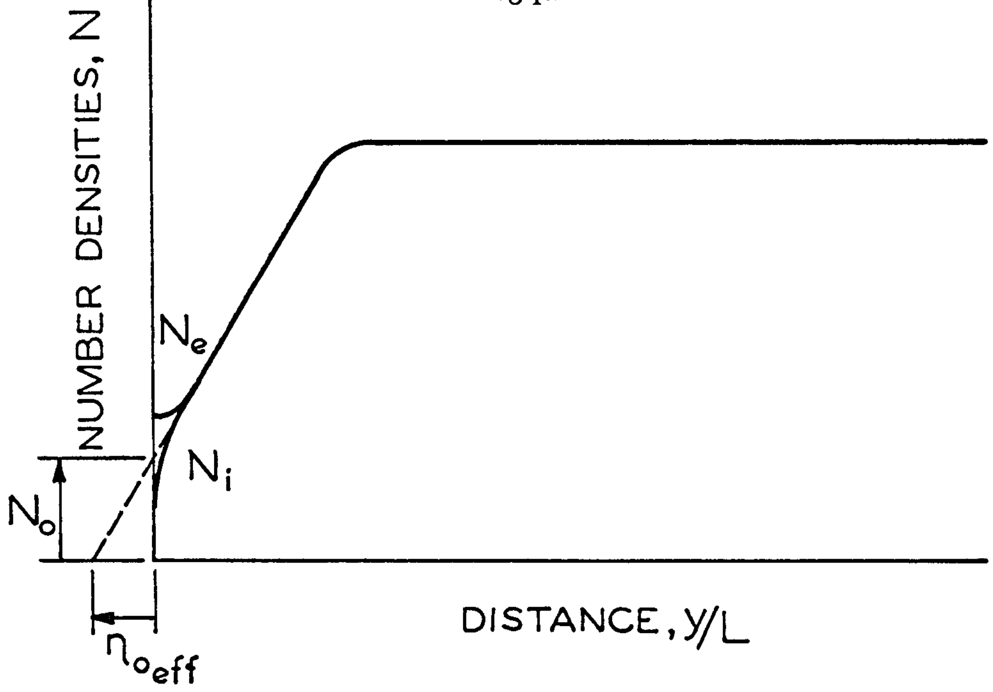

CASE (a) RELAXATION SHEATH

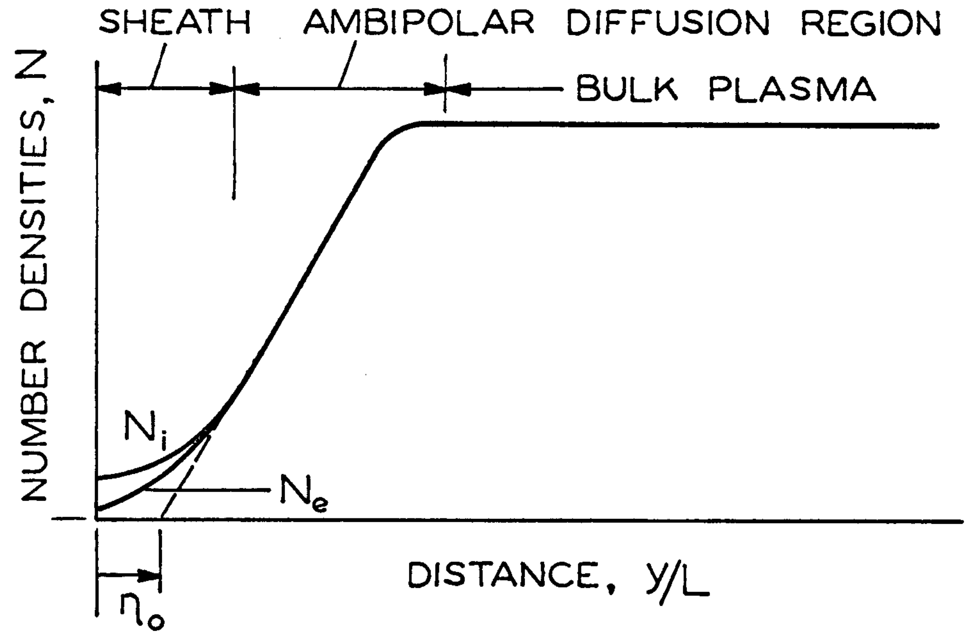

CASE (b) DIFFUSION SHEATH

FIG. 4 NUMBER DENSITY PROFILES

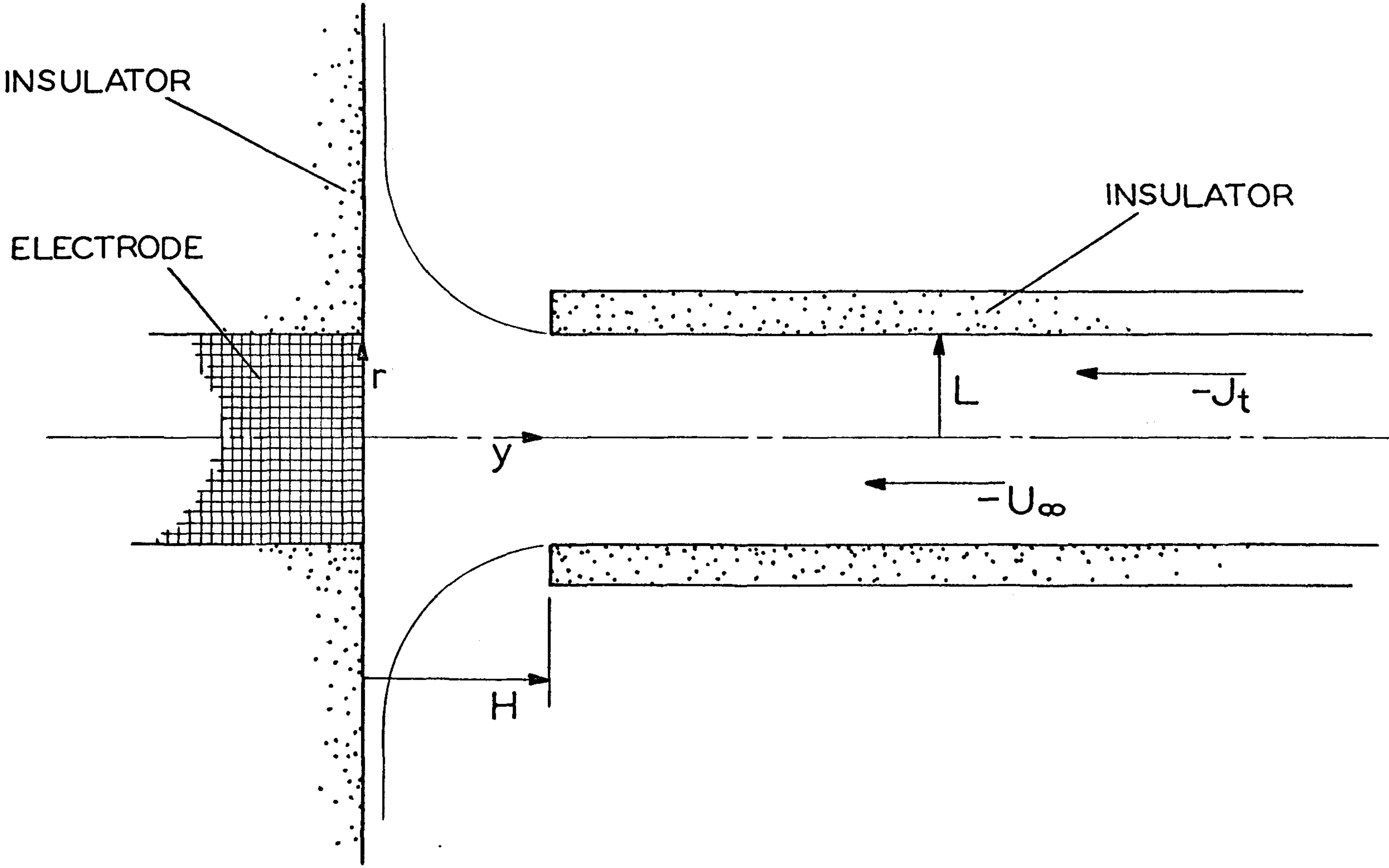

FIG. 5 SYSTEM GEOMETRY

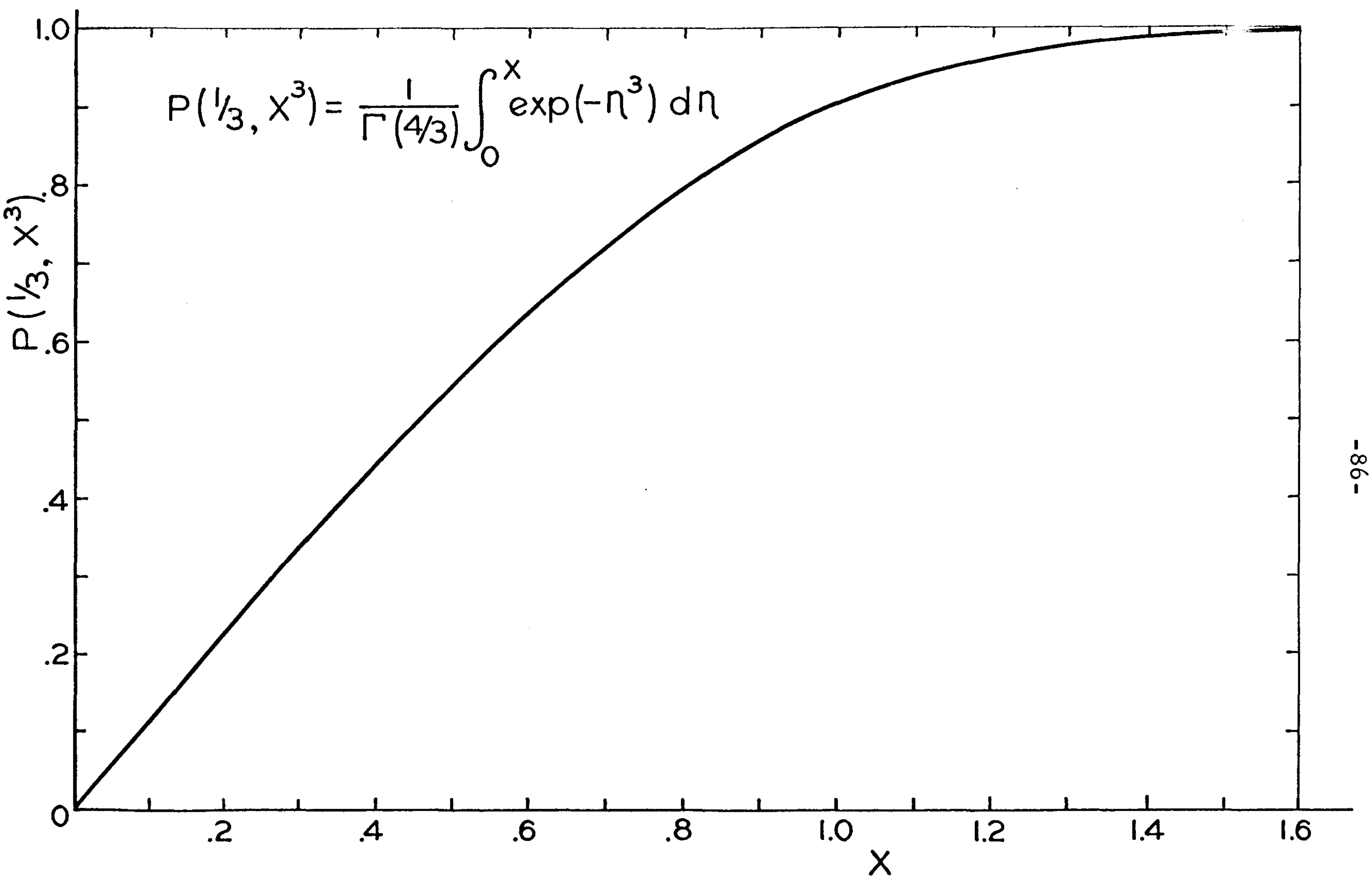

FIG. 6 DIFFUSION SOLUTION FUNCTION

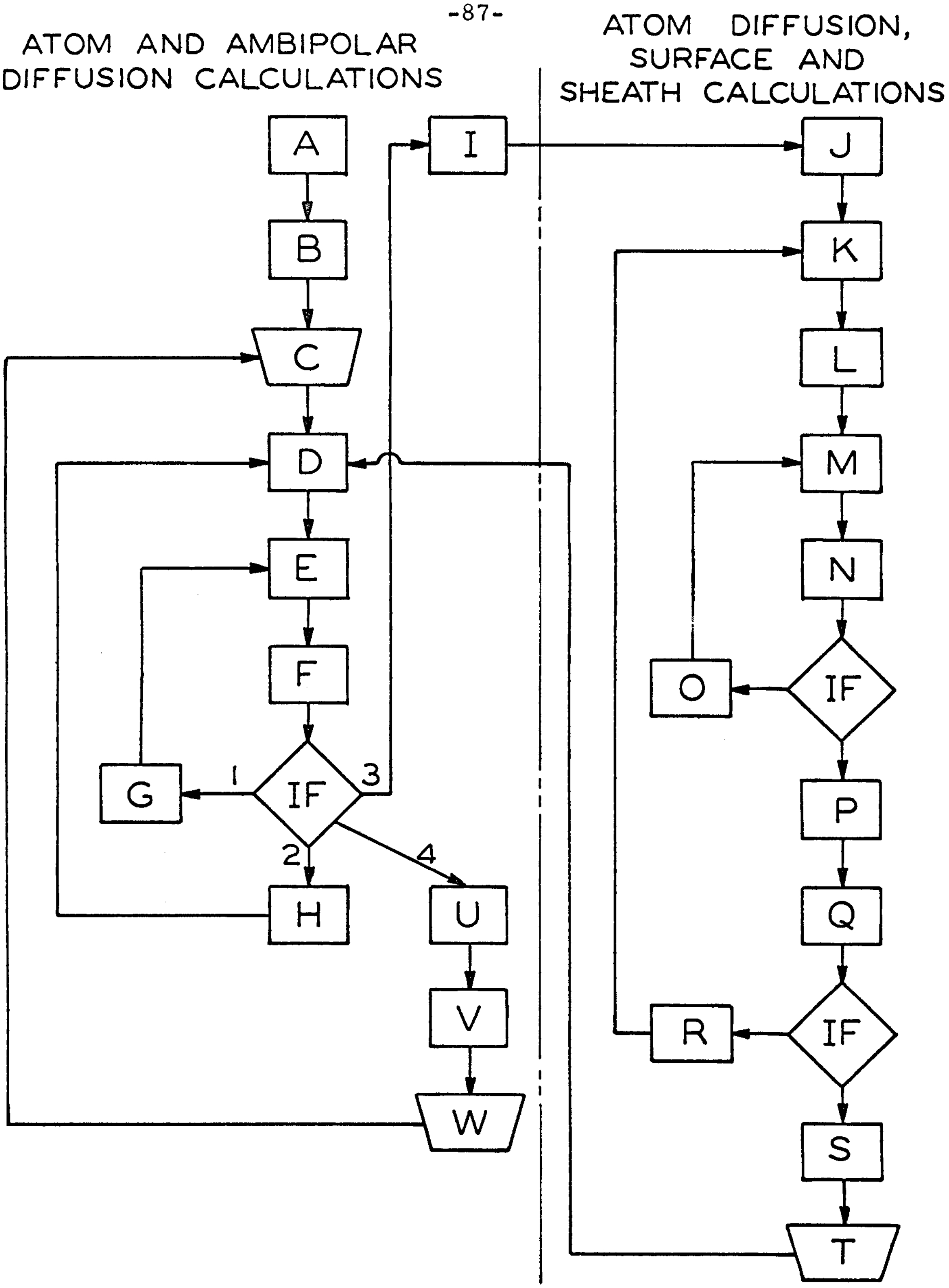

FIG. 7 COMPUTATION SCHEME

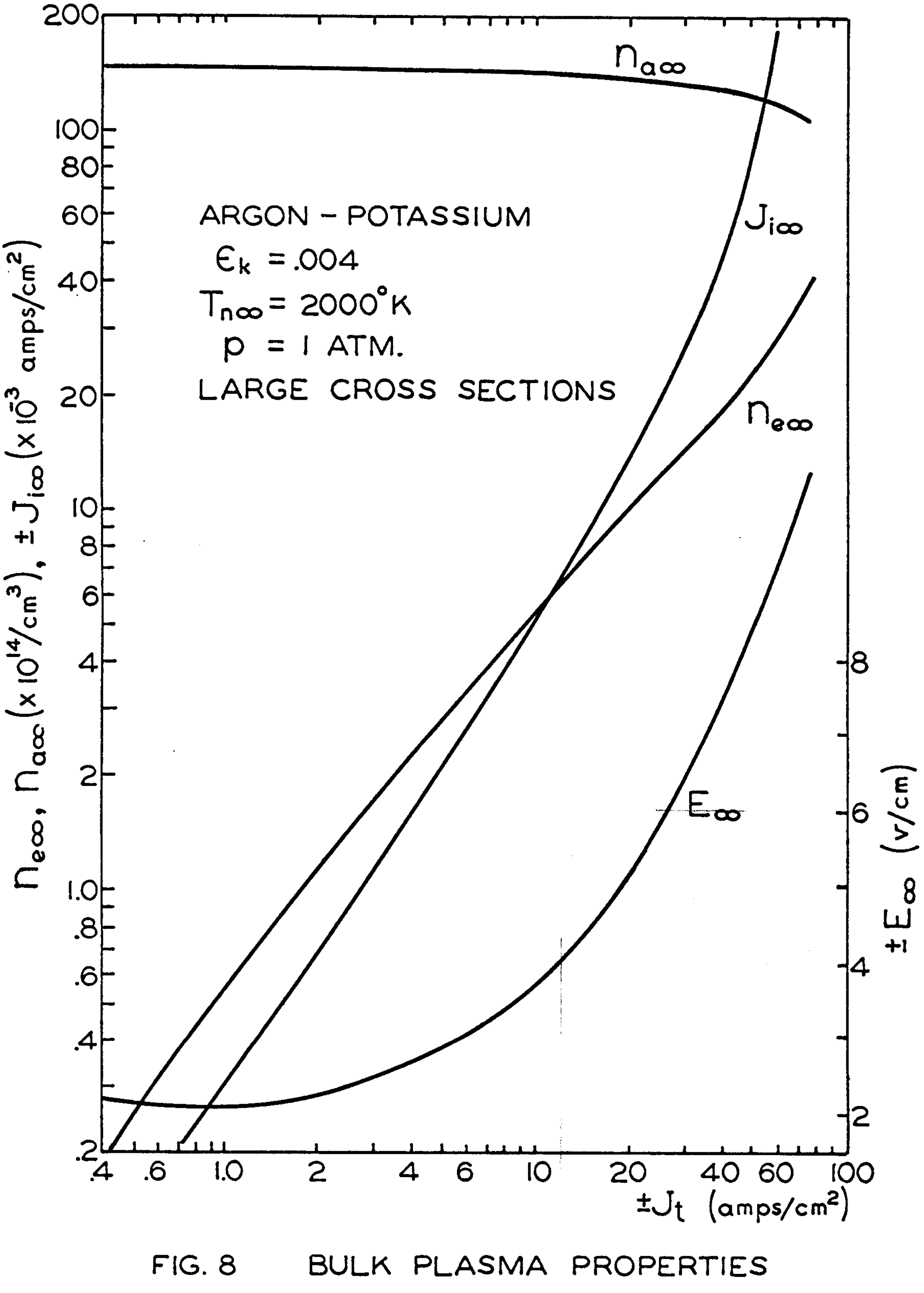

FIG. 8 BULK PLASMA PROPERTIES

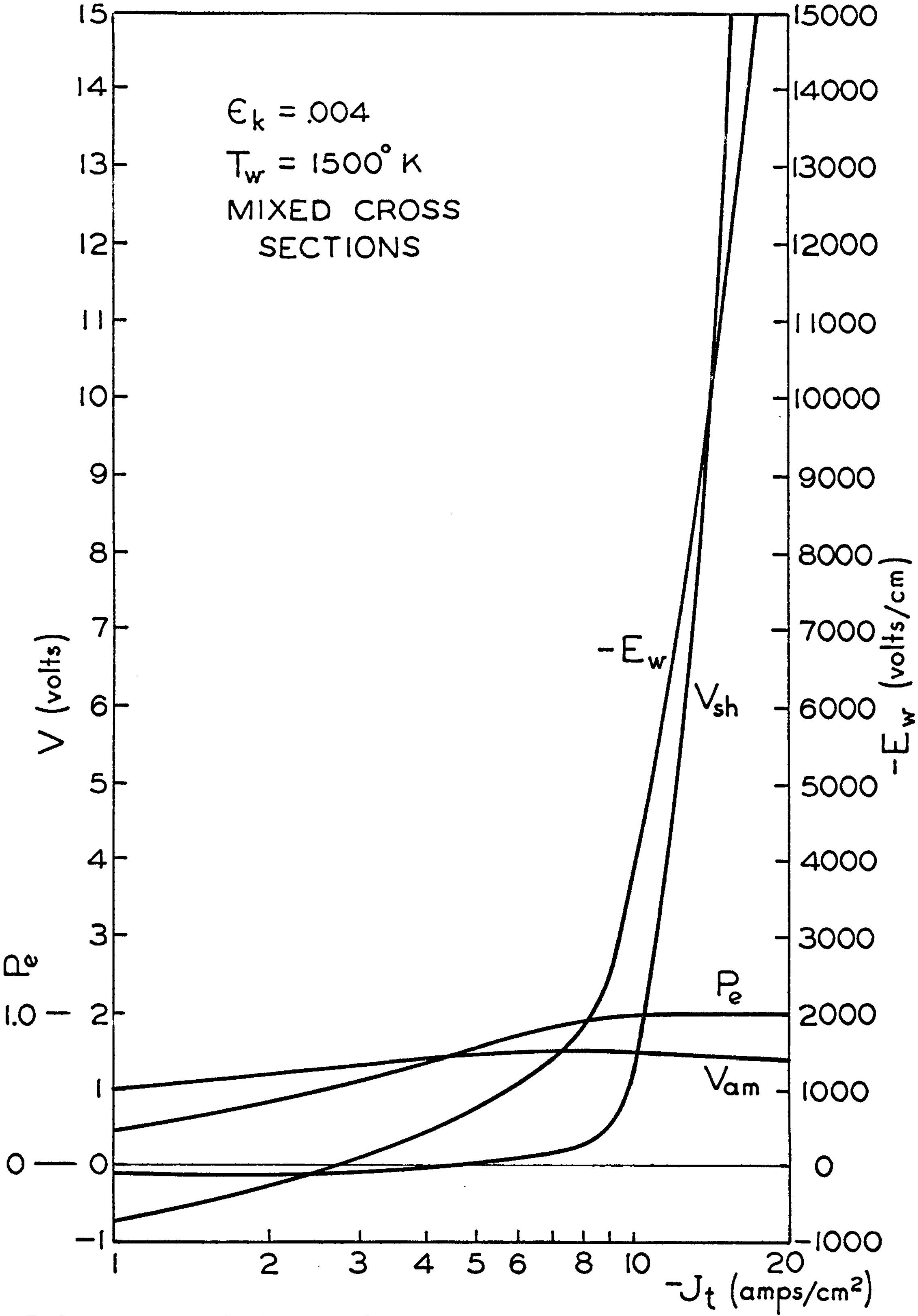

FIG. 9 CURRENT DENSITY CHARACTERISTICS

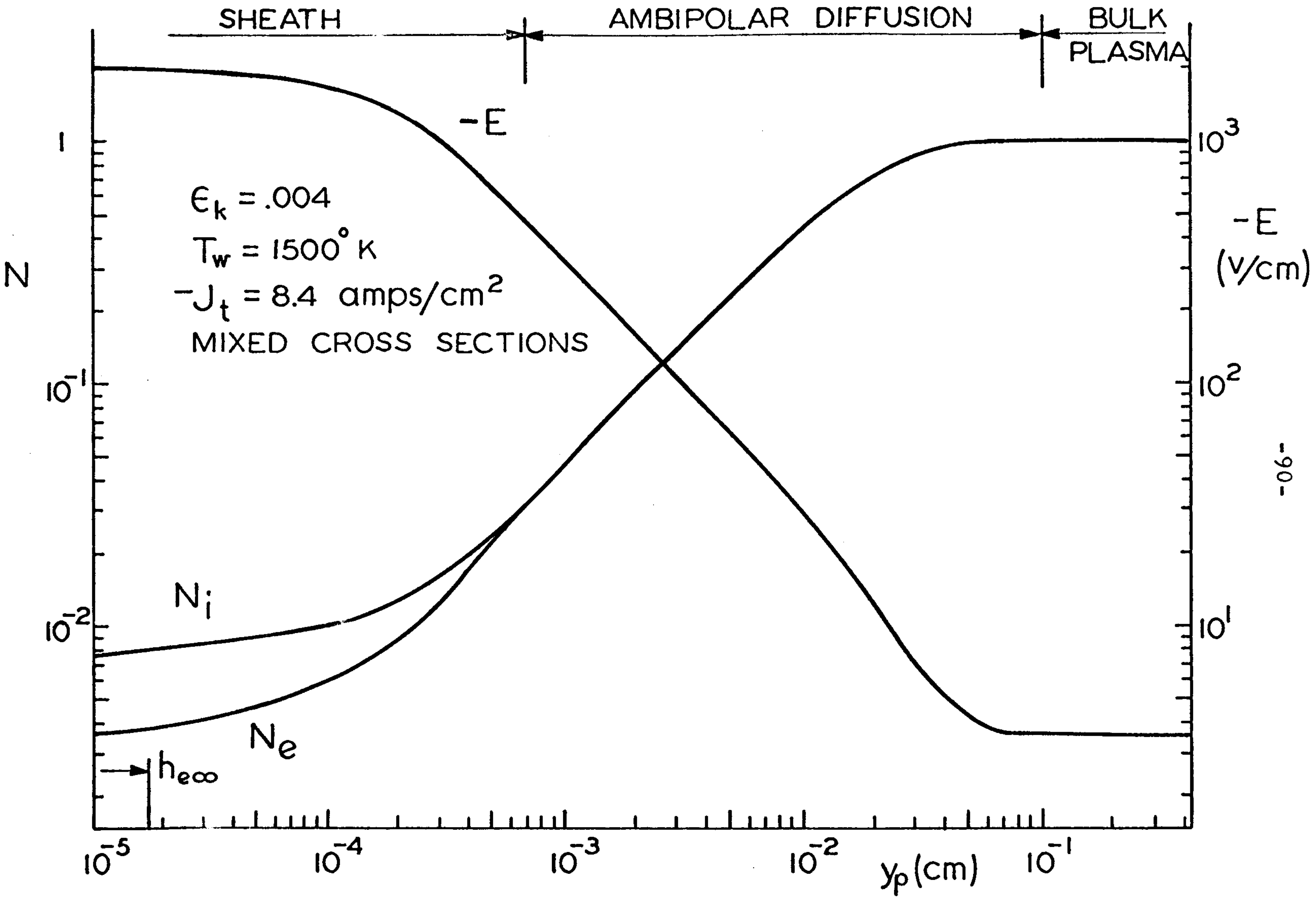

FIG. 10 COMPOSITE SOLUTION

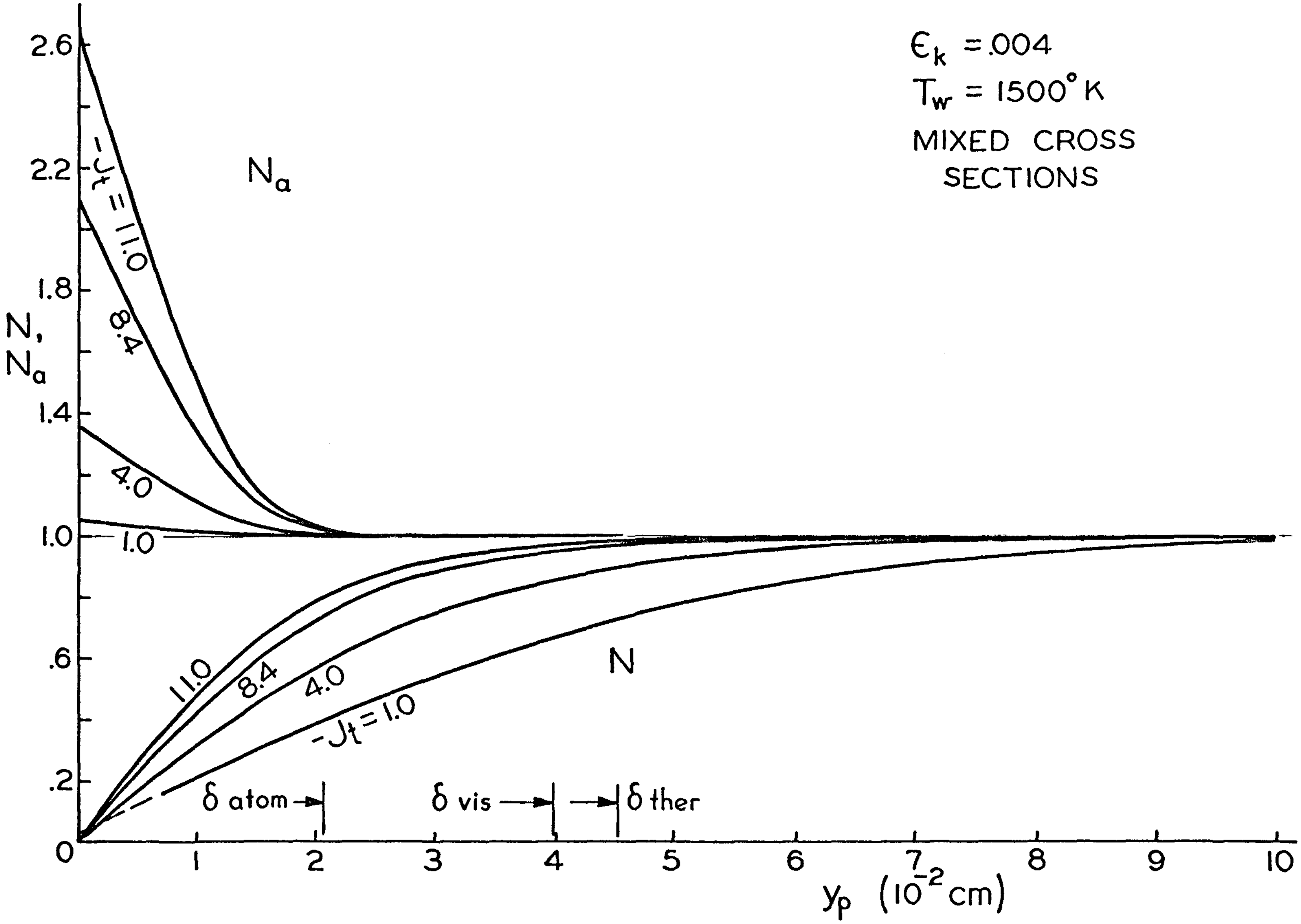

FIG. 11 ATOM AND AMBIPOLAR DIFFUSION SOLUTIONS

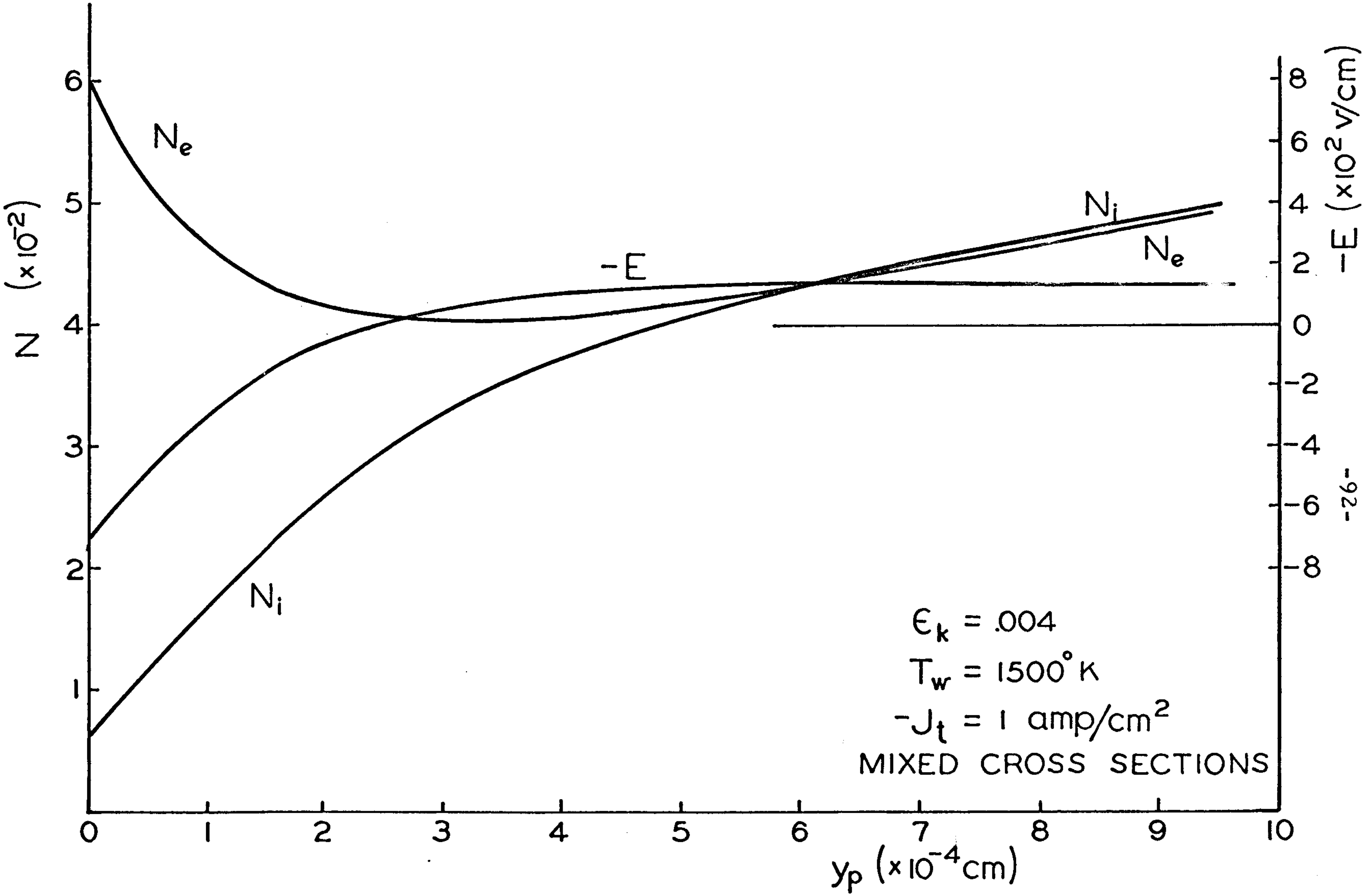

FIG. 12a SHEATH STRUCTURE

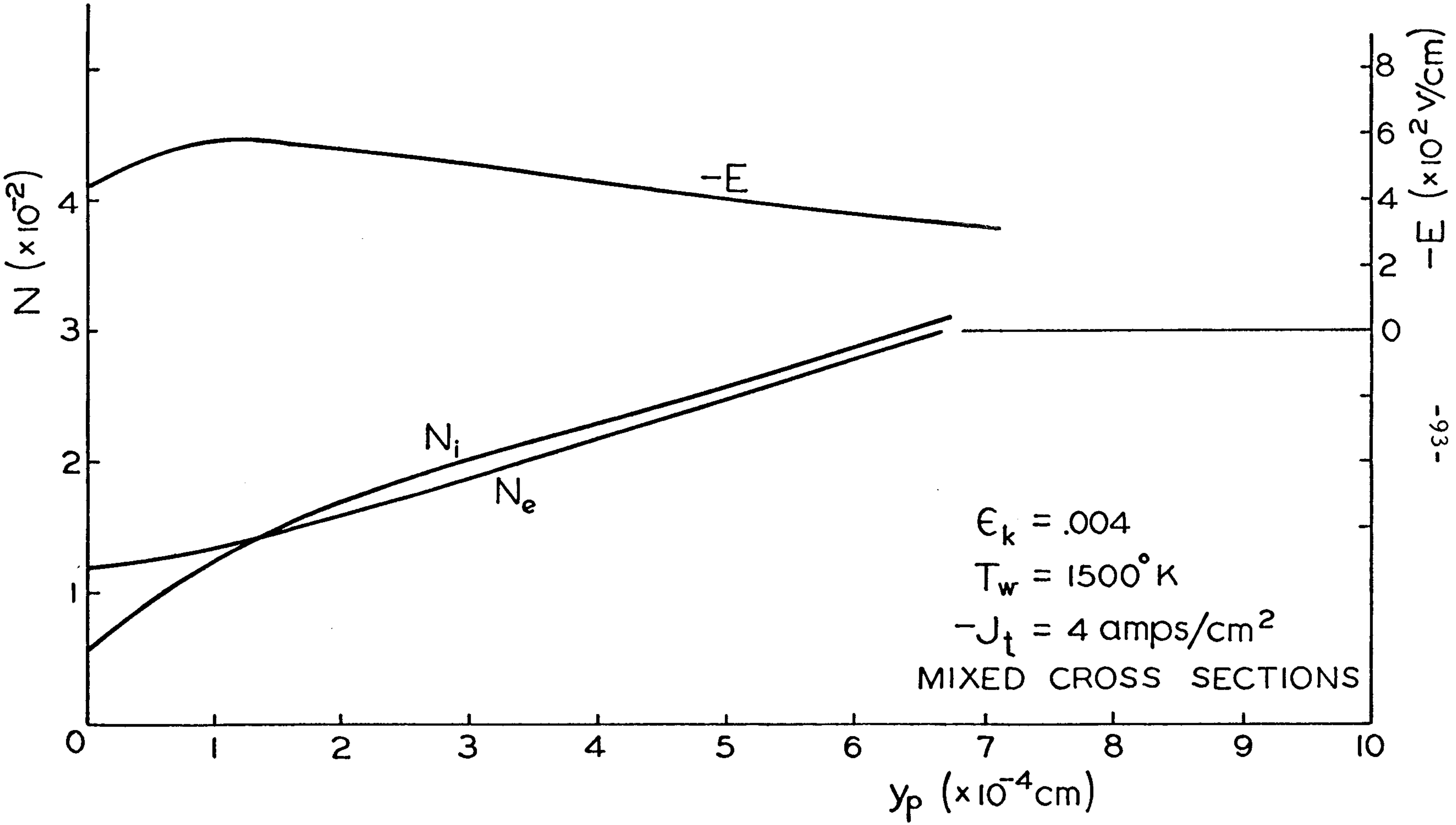

FIG. 12 b SHEATH STRUCTURE

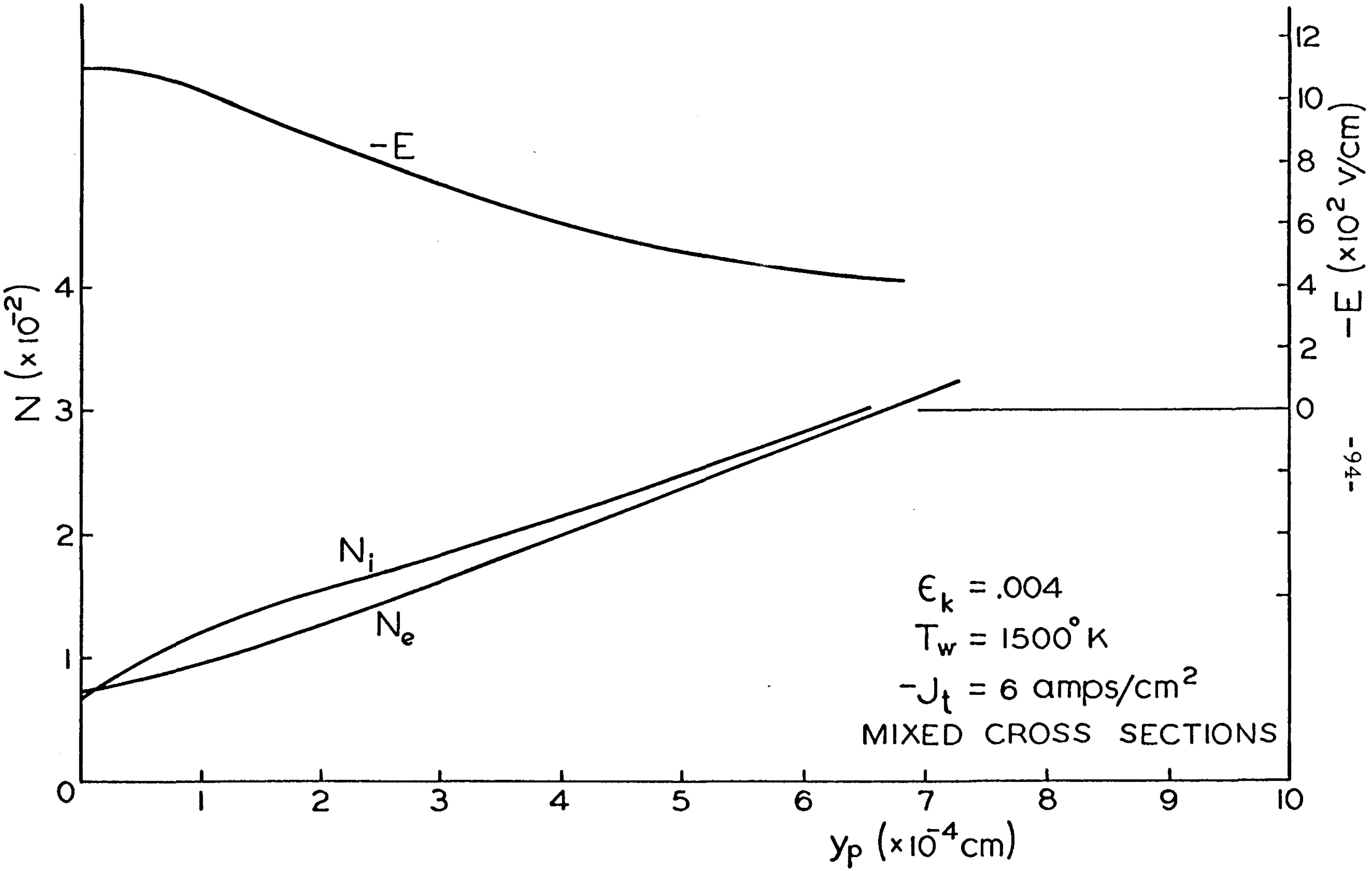

FIG. 12c SHEATH STRUCTURE

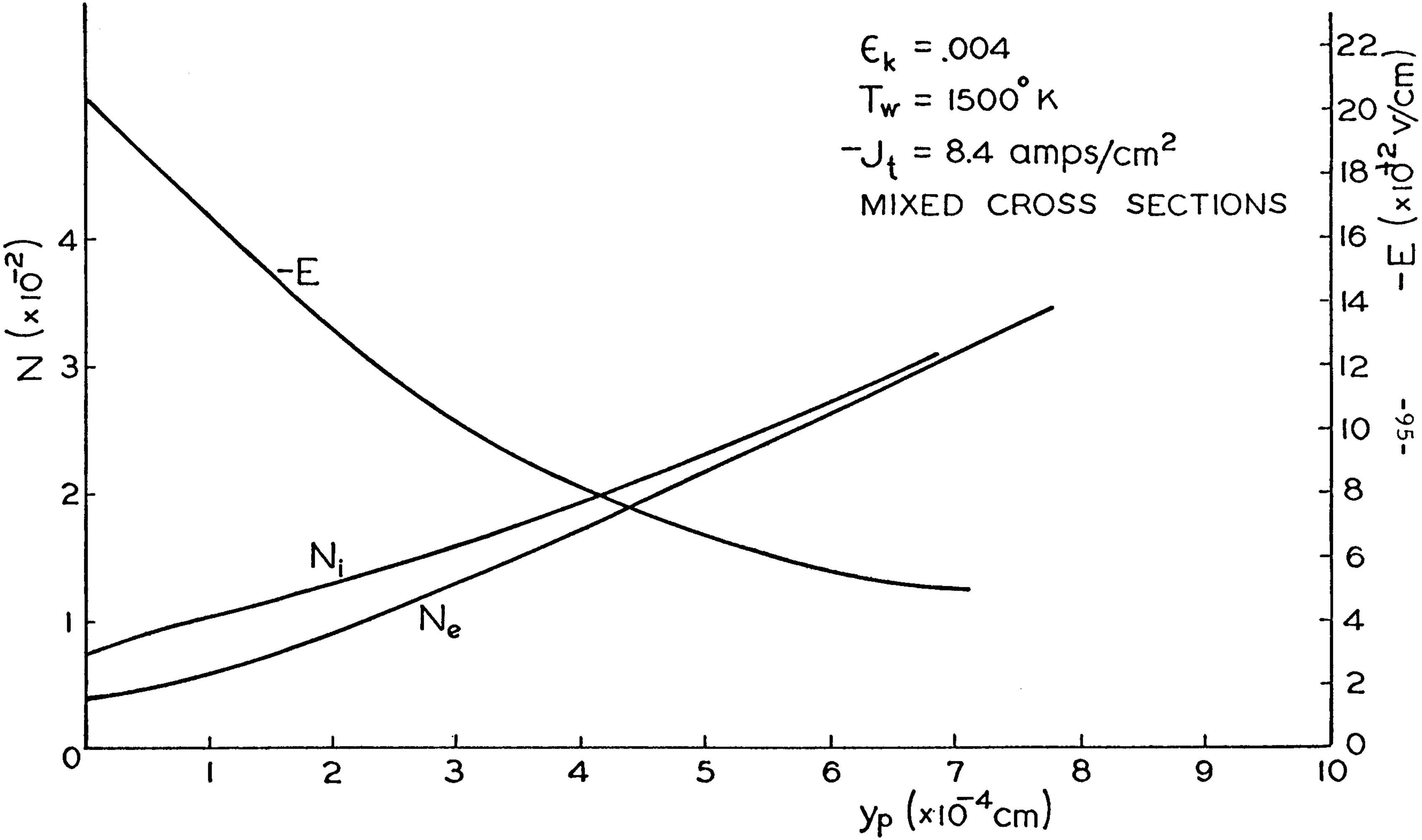

FIG. 12d SHEATH STRUCTURE

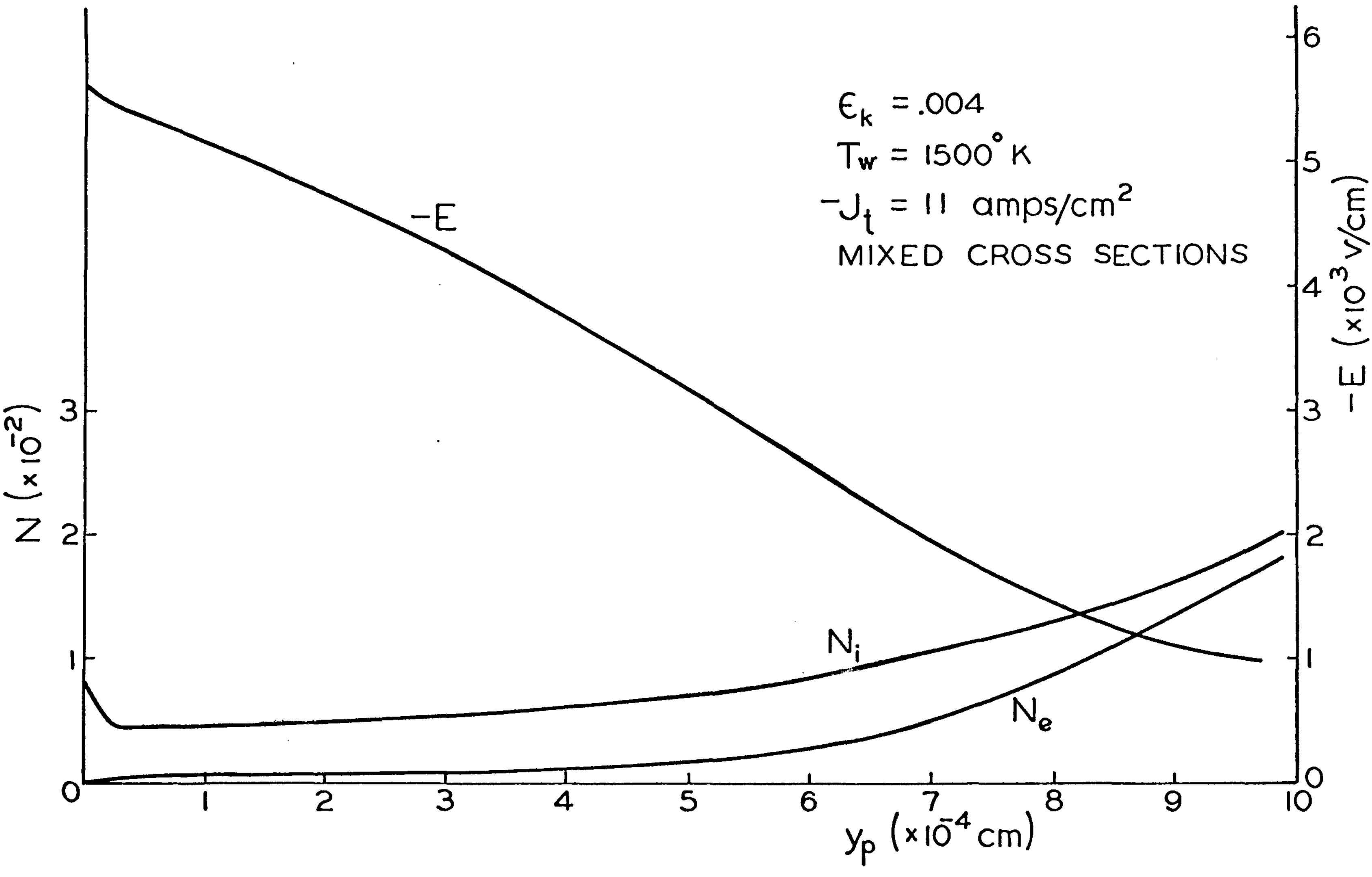

FIG. 12e SHEATH STRUCTURE

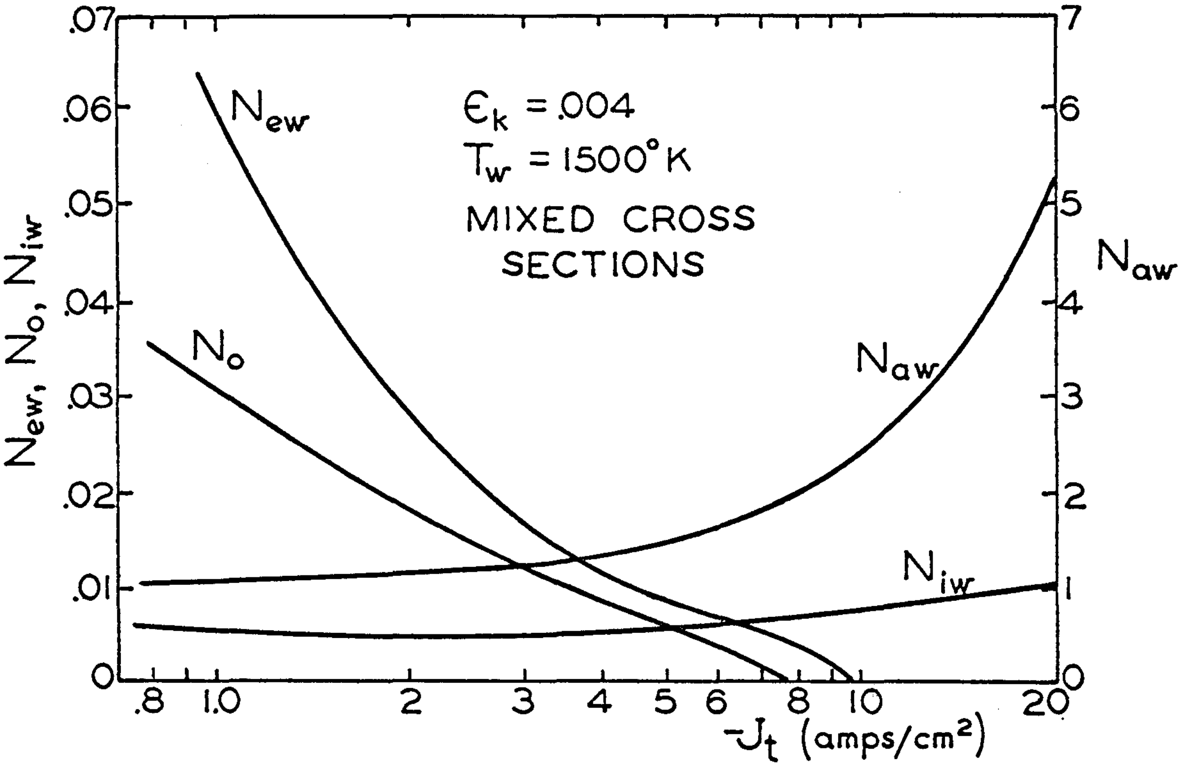

FIG. 13 BOUNDARY CONDITIONS

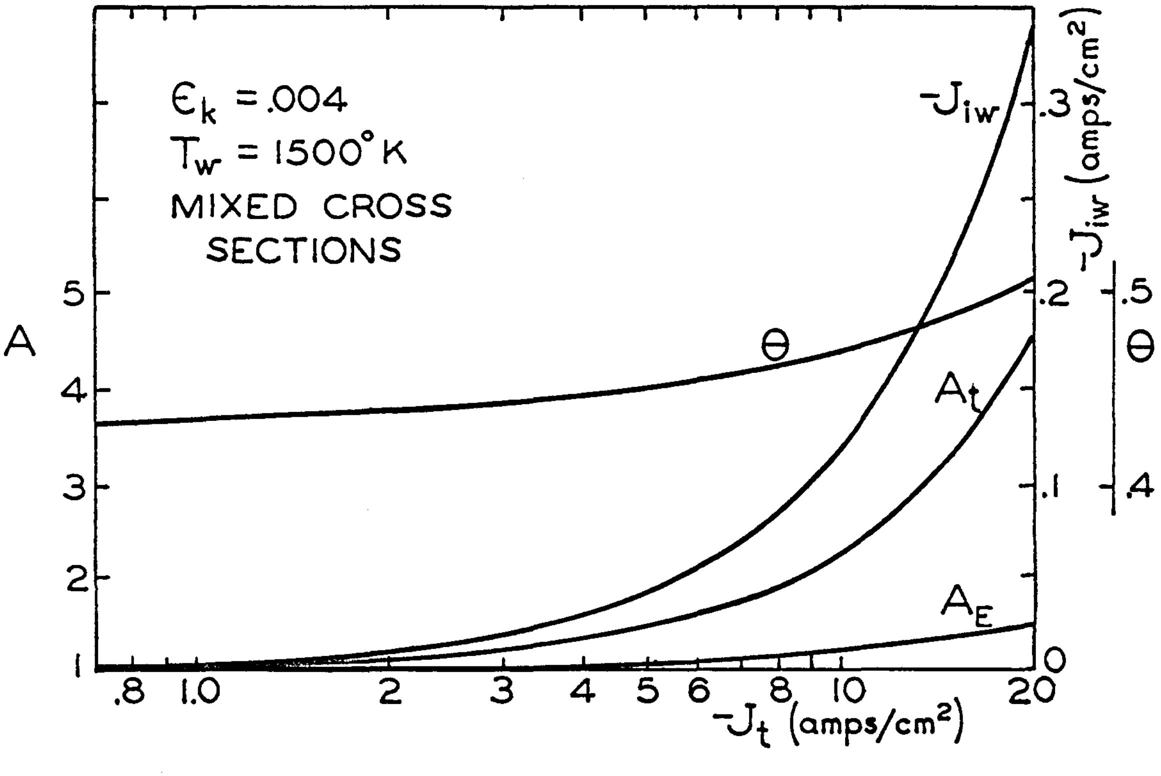

FIG. 14 CATHODE EMISSION AUGMENTATION

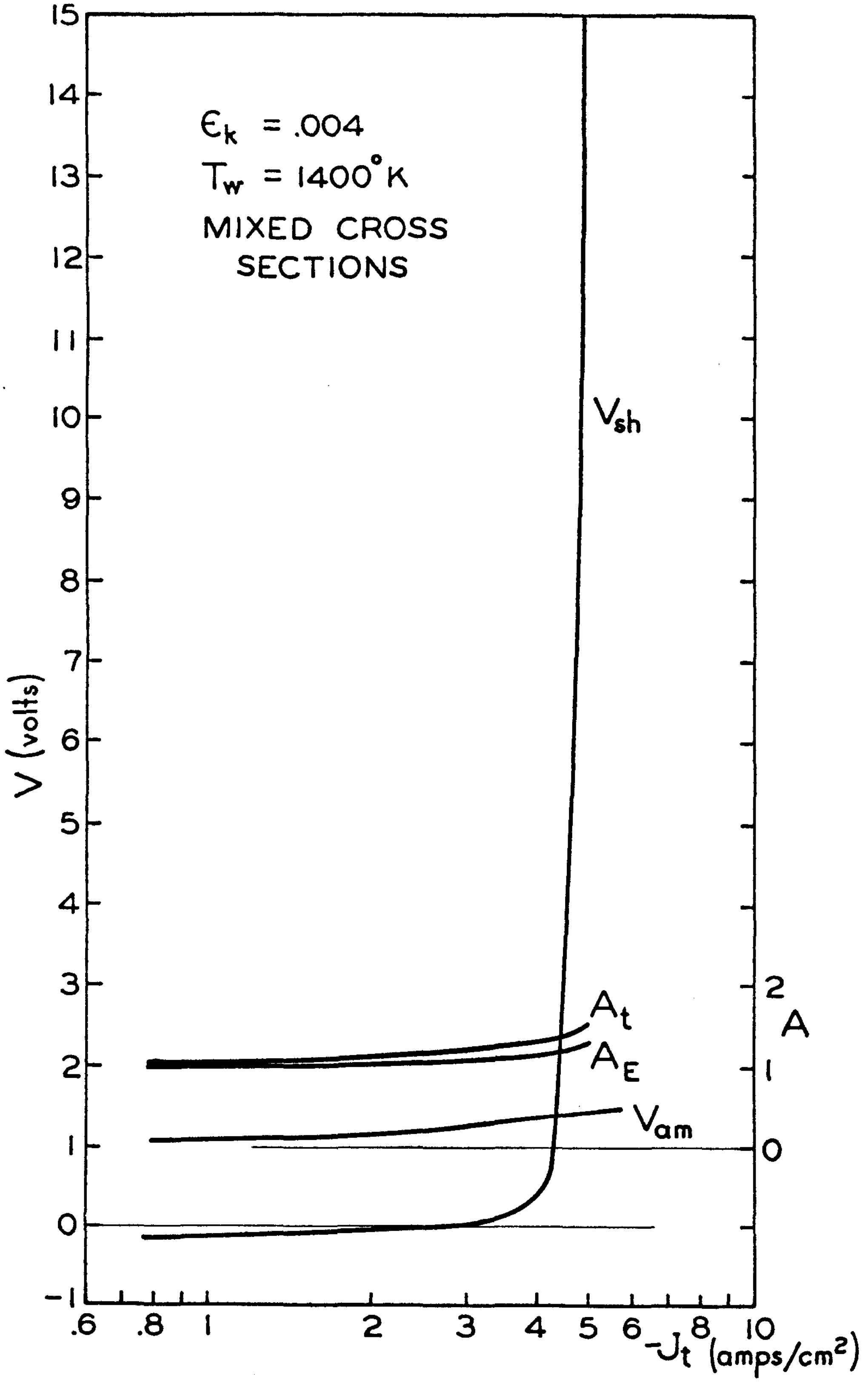

FIG. 15 CURRENT DENSITY CHARACTERISTICS

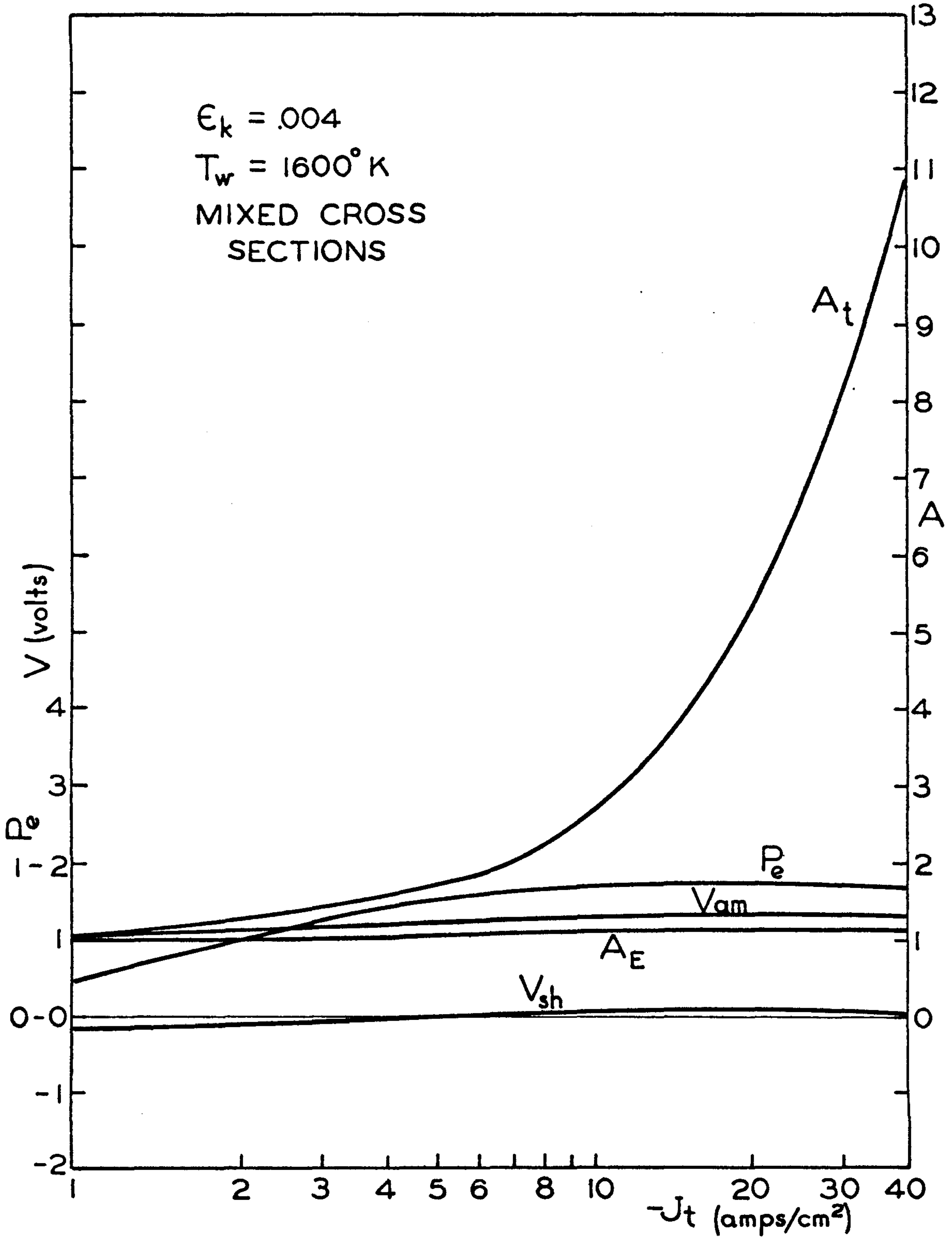

FIG. 16 CURRENT DENSITY CHARACTERISTICS

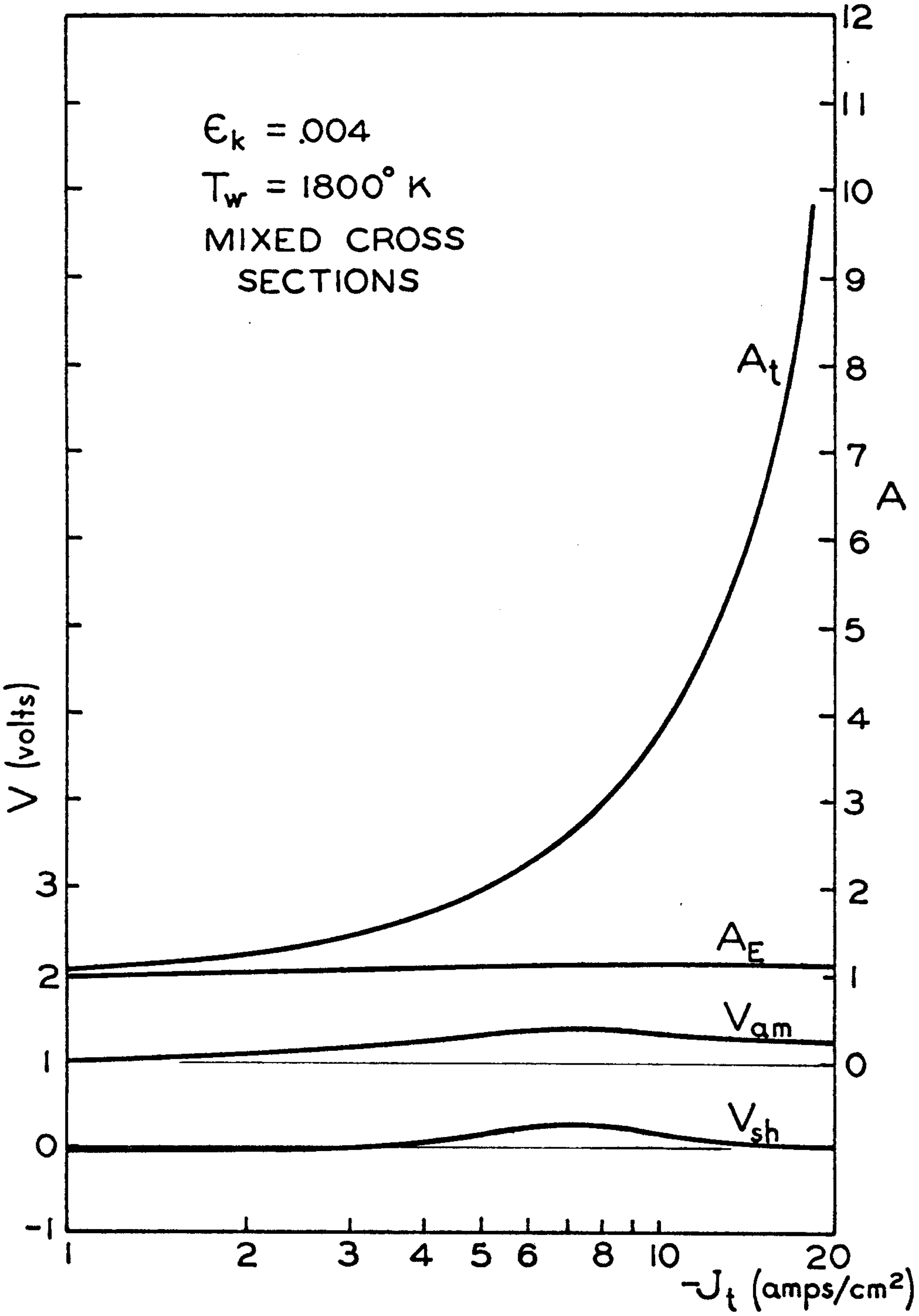

FIG. 17 CURRENT DENSITY CHARACTERISTICS

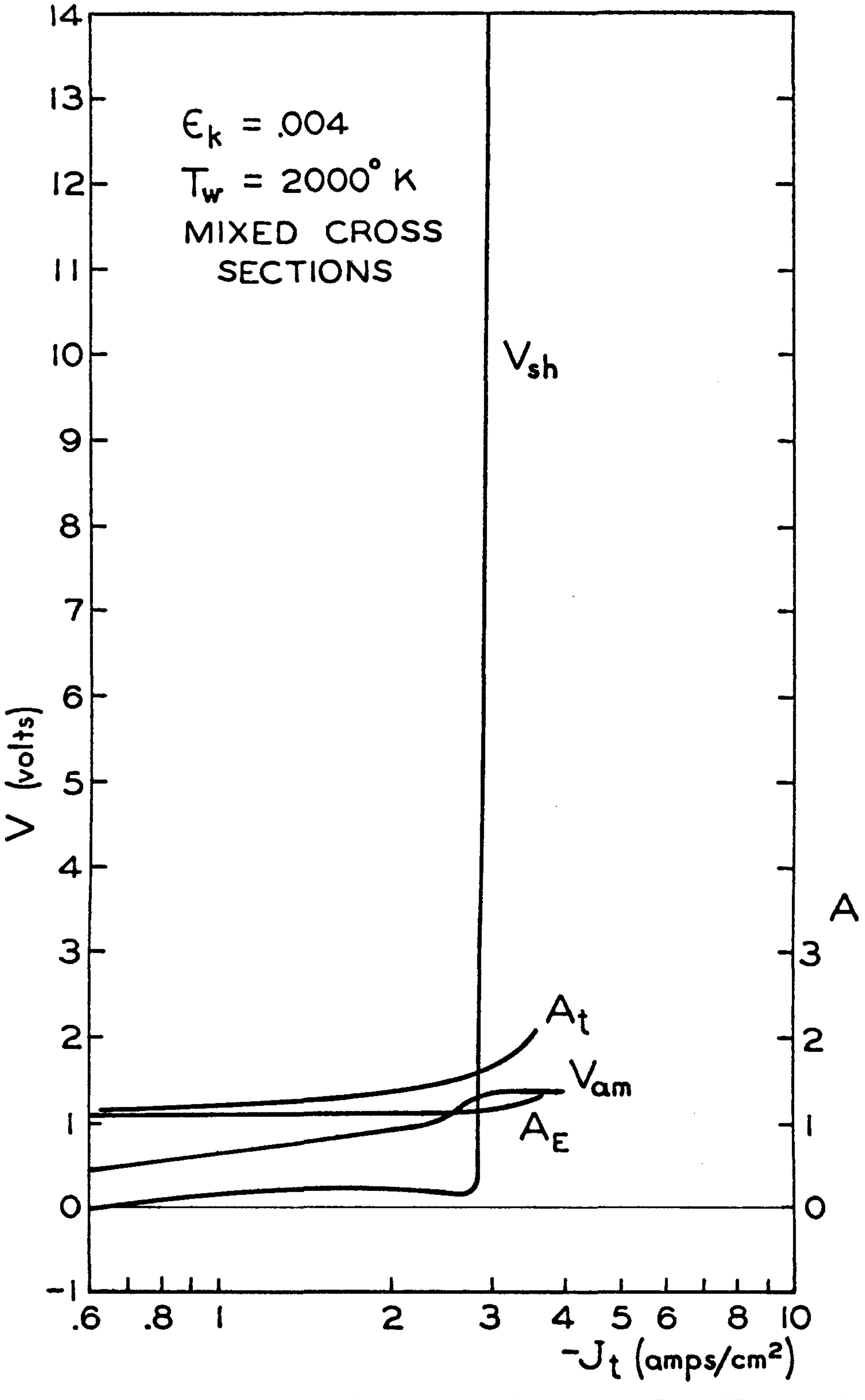

FIG. 18 CURRENT DENSITY CHARACTERISTICS

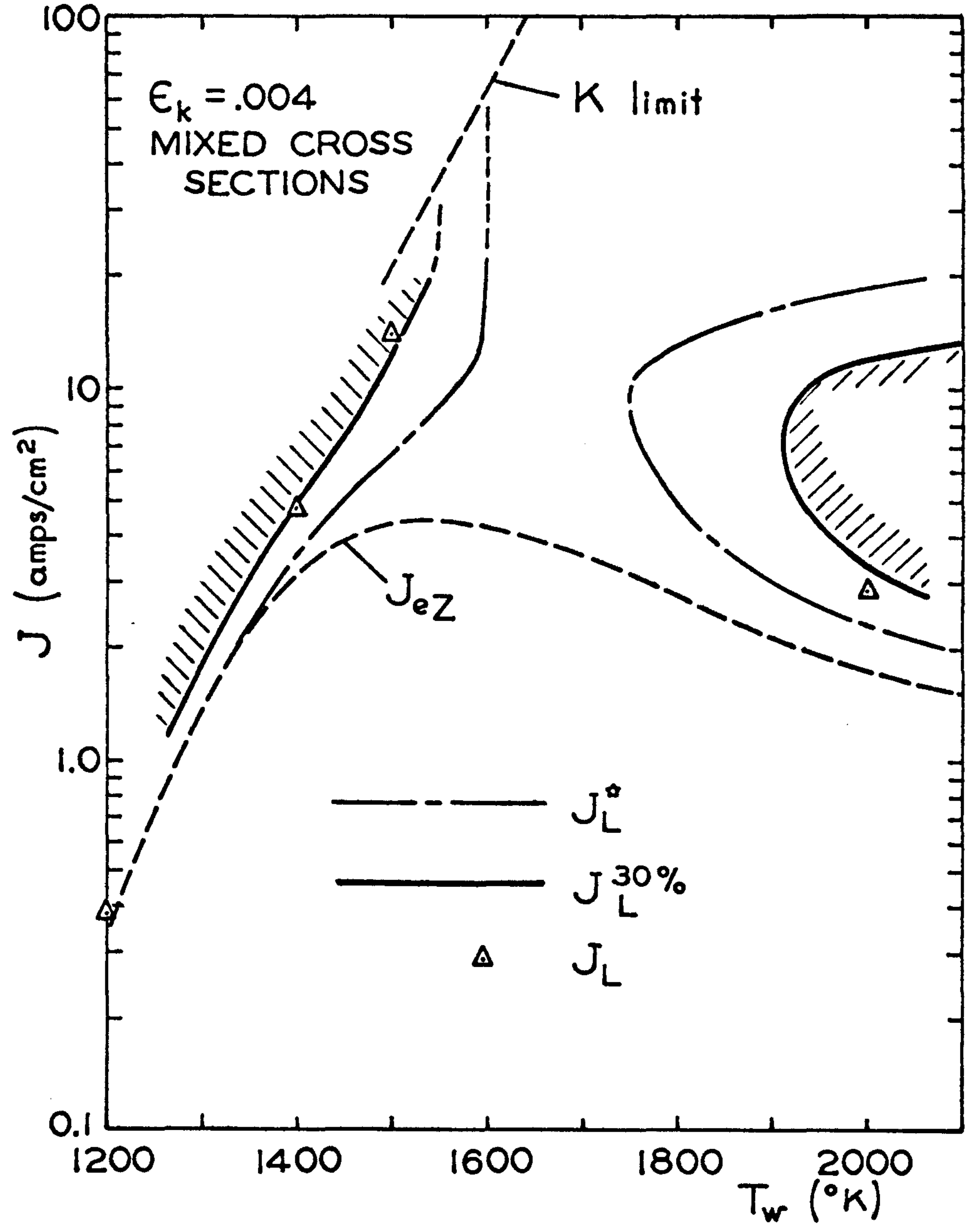

FIG. 19 THERMIONIC REGIME

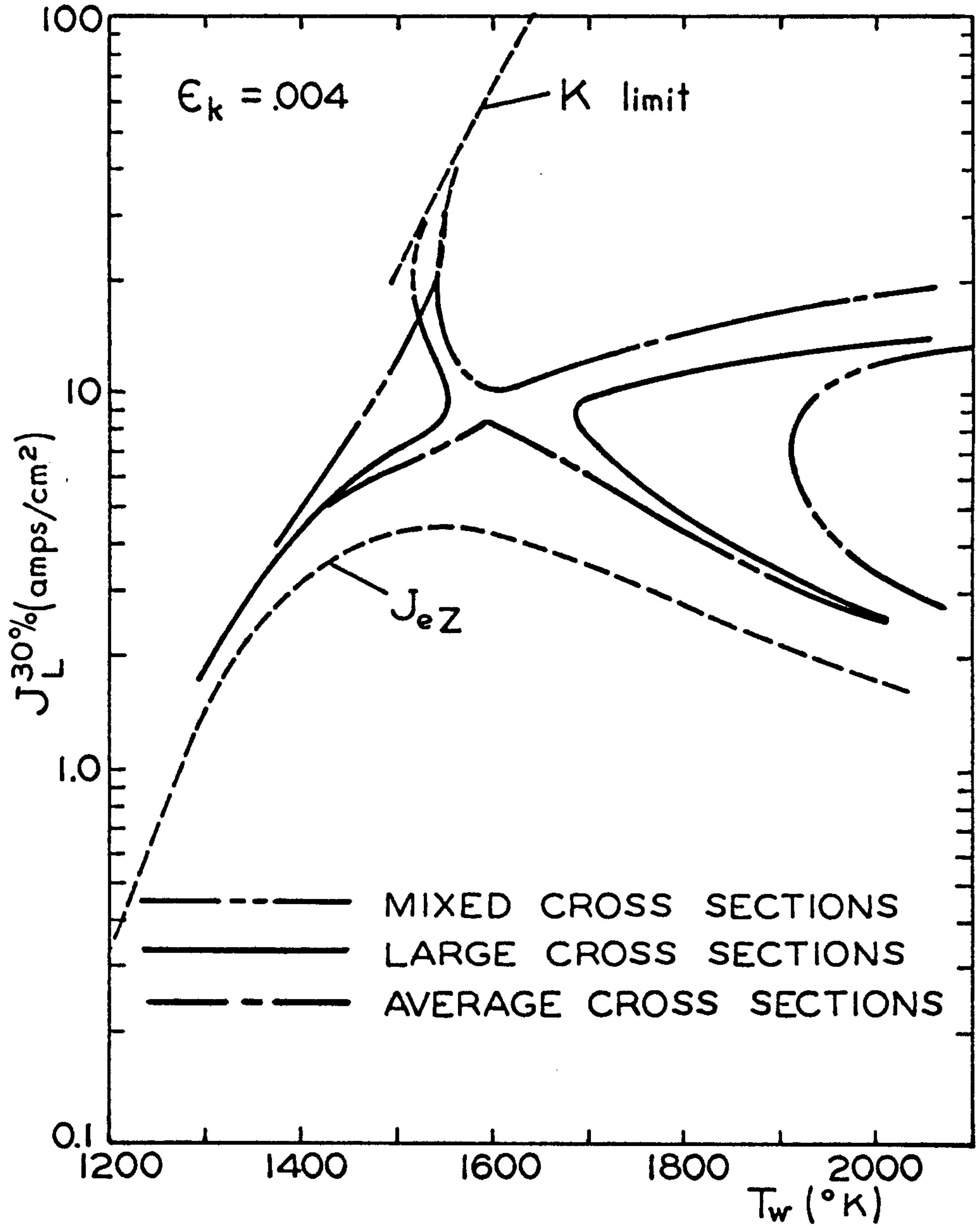

FIG. 20 CROSS SECTION EFFECT ON THERMIONIC REGIME

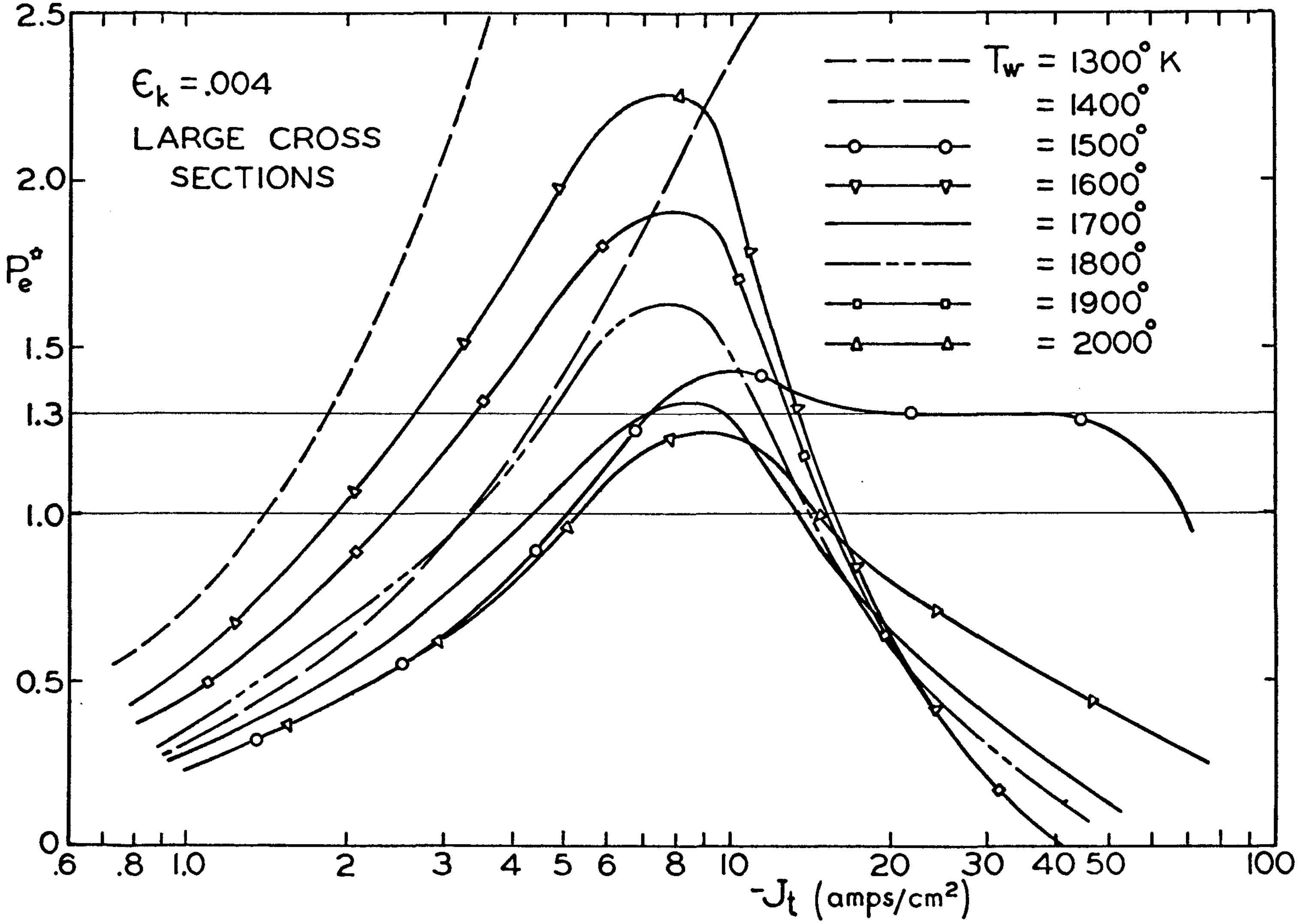

FIG. 21 ELECTRON CURRENT FRACTION

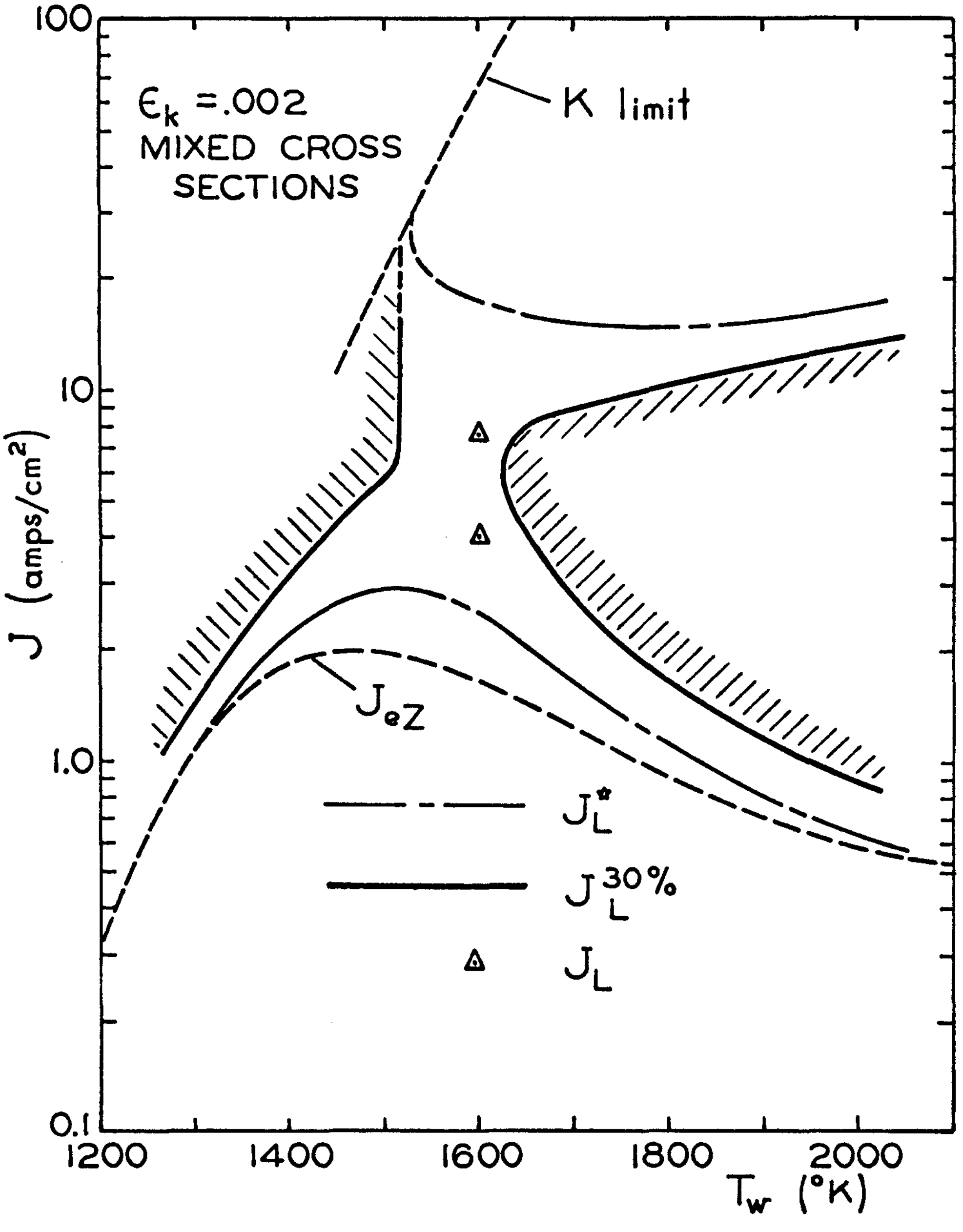

FIG. 22 THERMIONIC REGIME

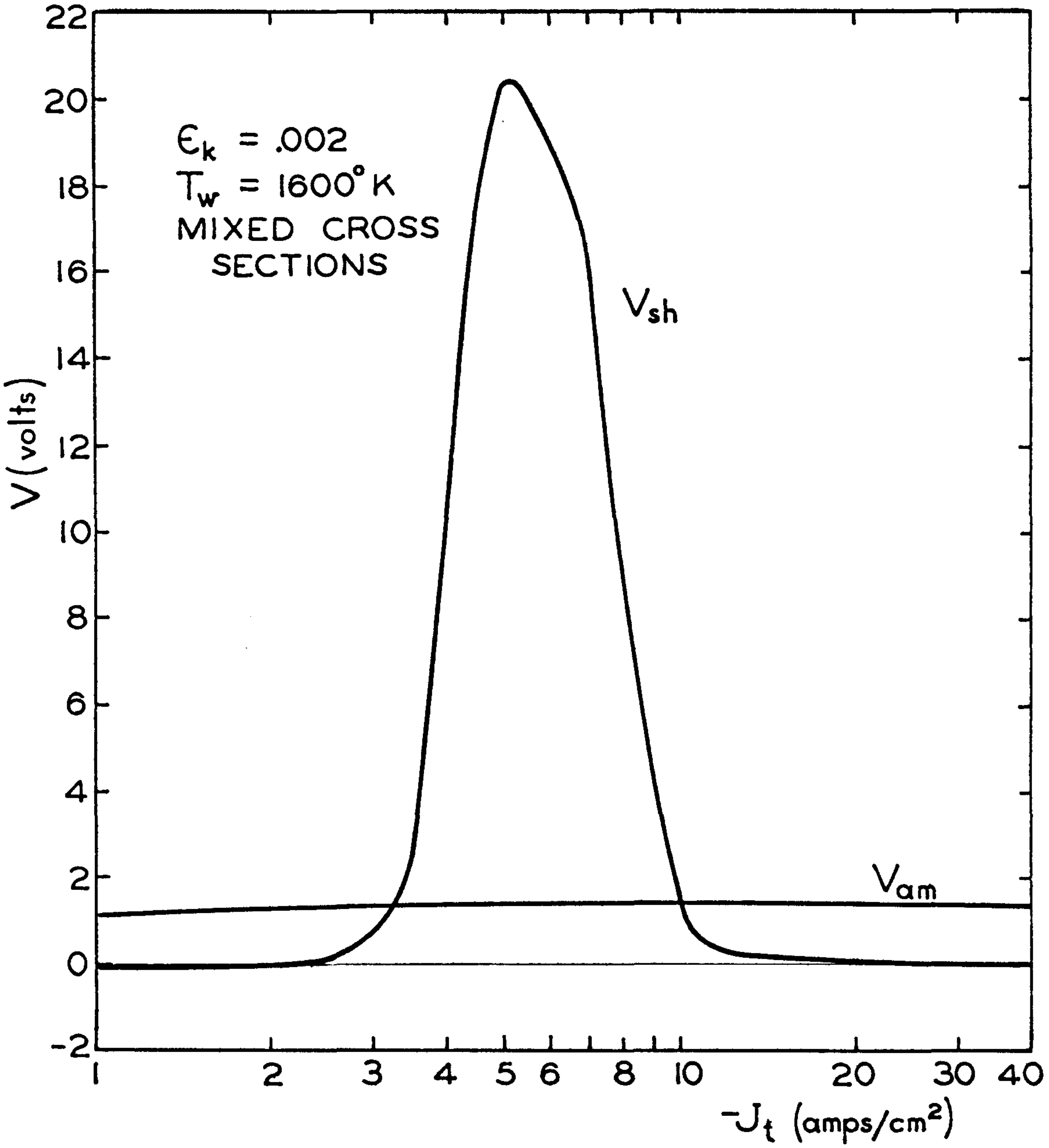

FIG. 23 CURRENT DENSITY CHARACTERISTICS

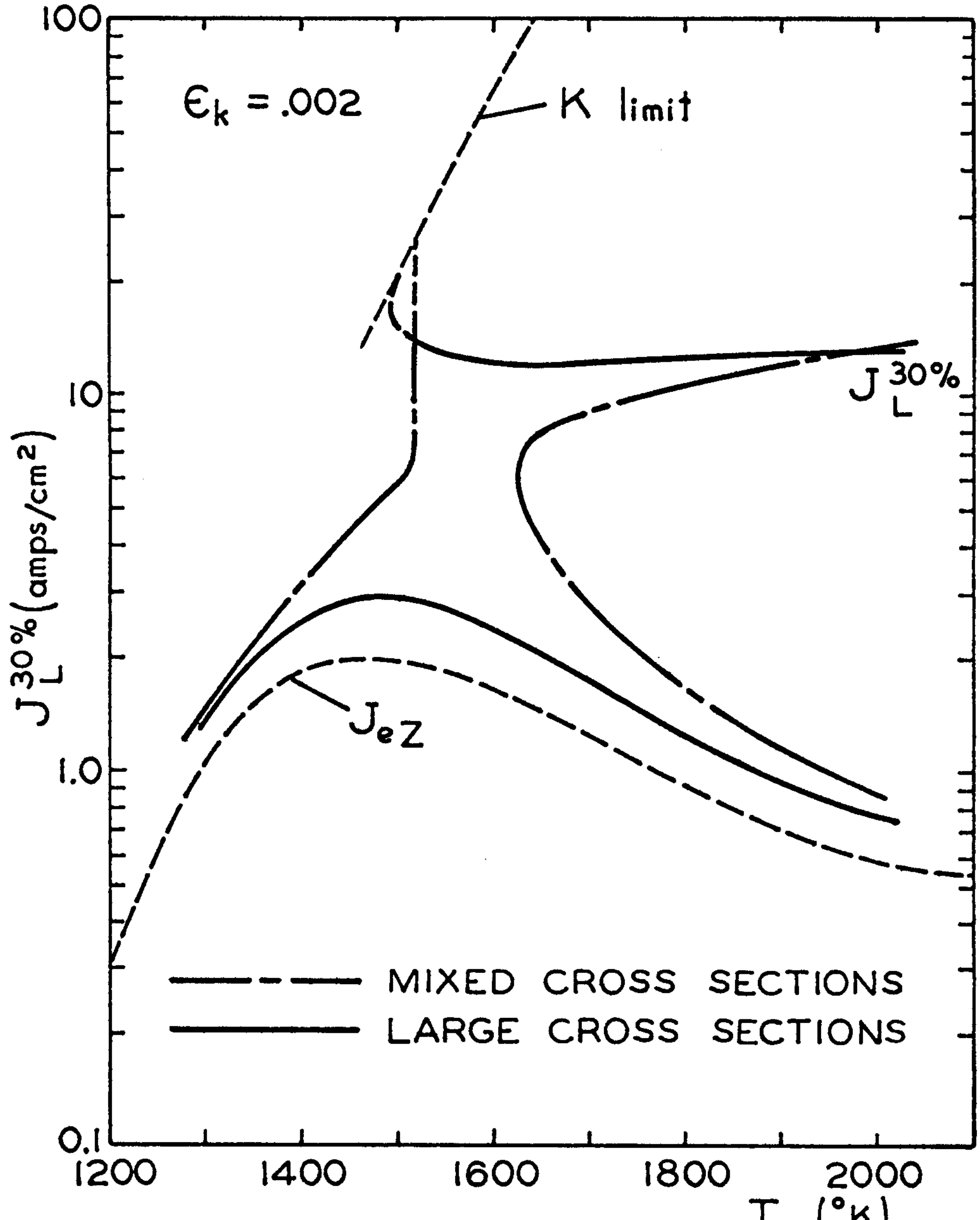

FIG. 24 CROSS SECTION EFFECT
ON THERMIONIC REGIME

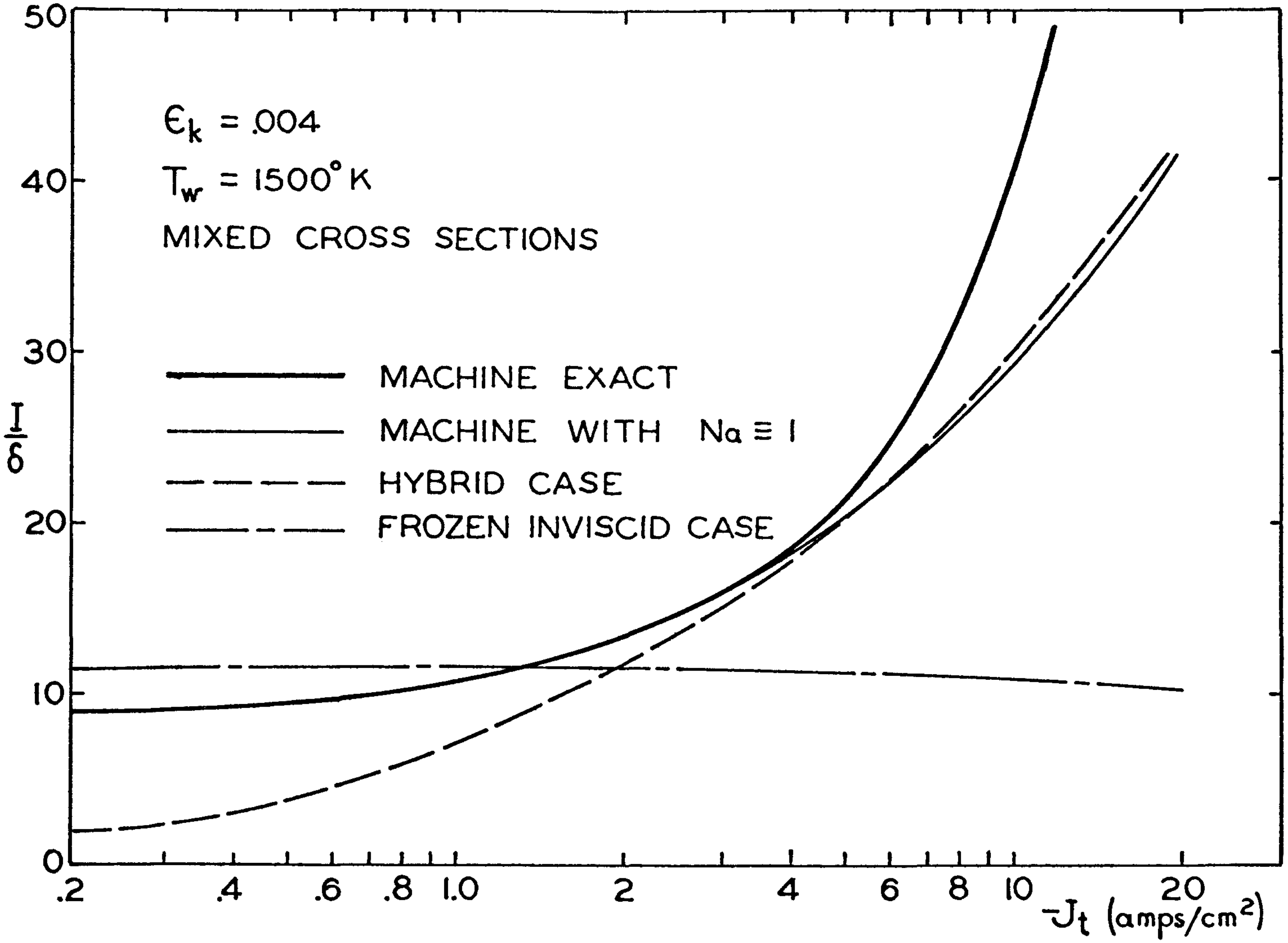

FIG. 25 COMPARISON OF AMBIPOLAR DIFFUSION SOLUTIONS

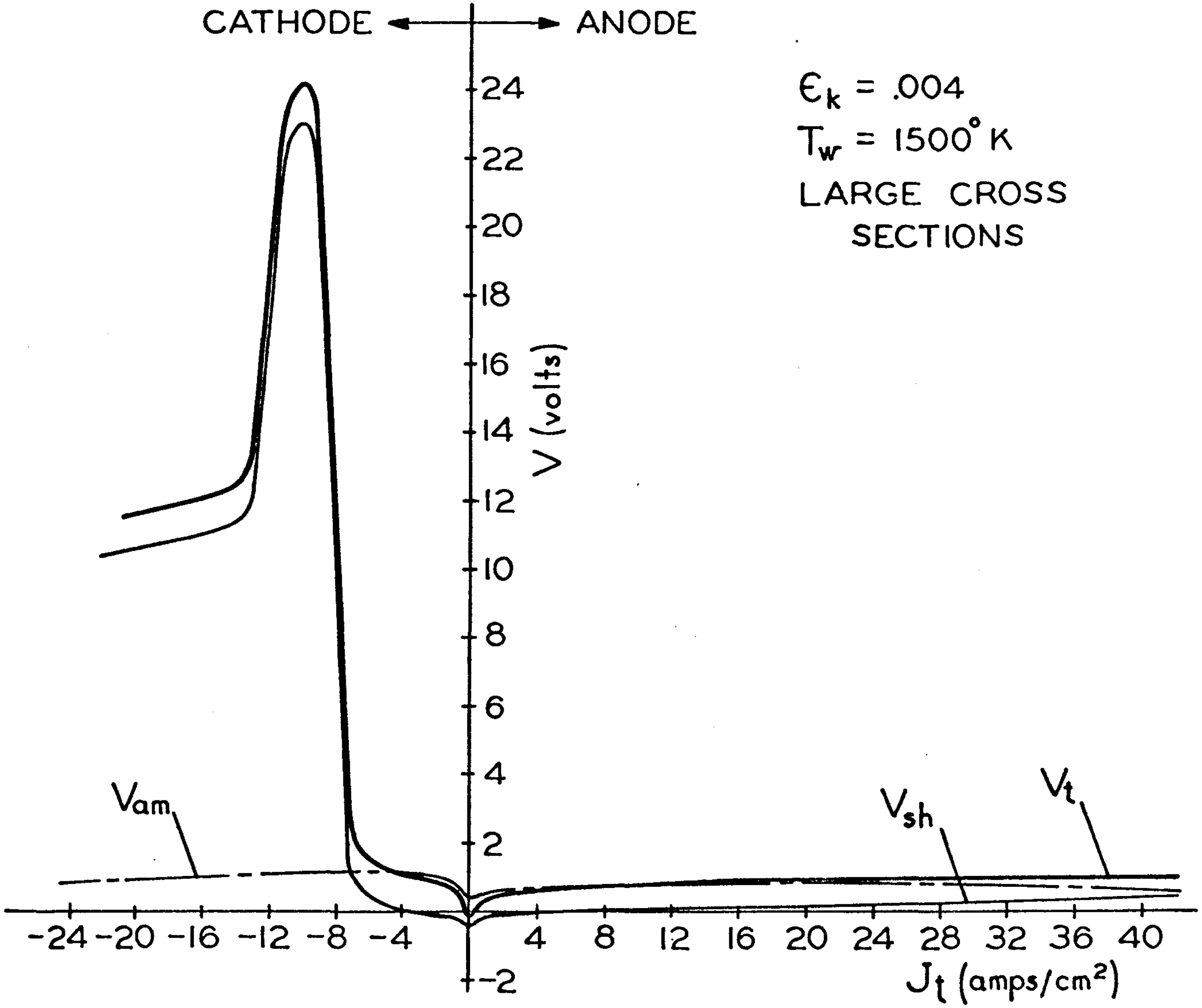

FIG. 26 CURRENT–VOLTAGE CHARACTERISTICS

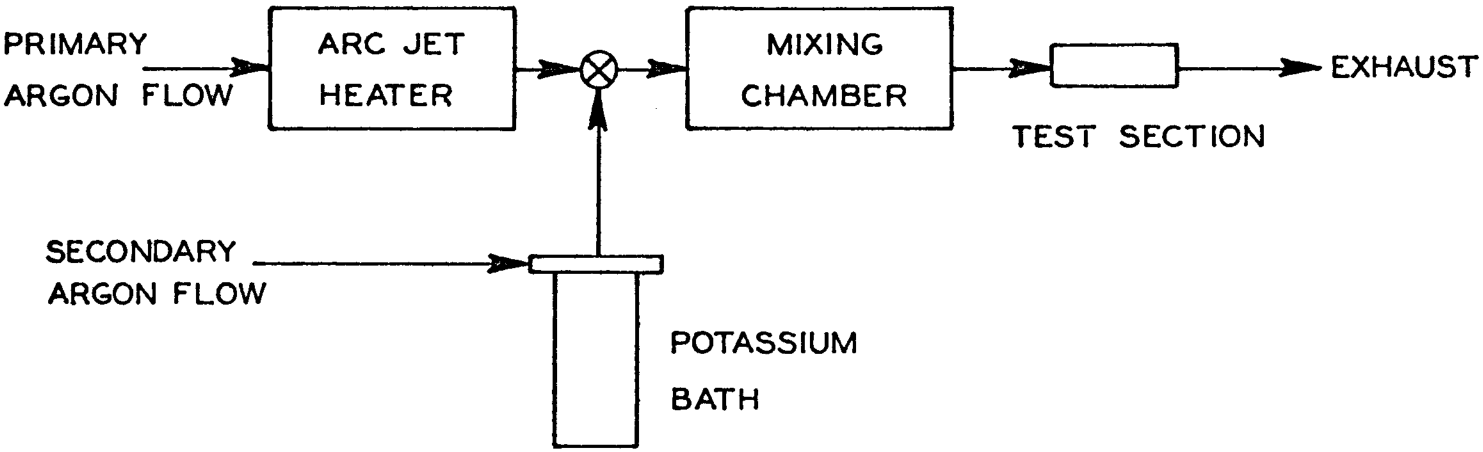

FIG. 27 SCHEMATIC DIAGRAM OF FLOW SYSTEMS

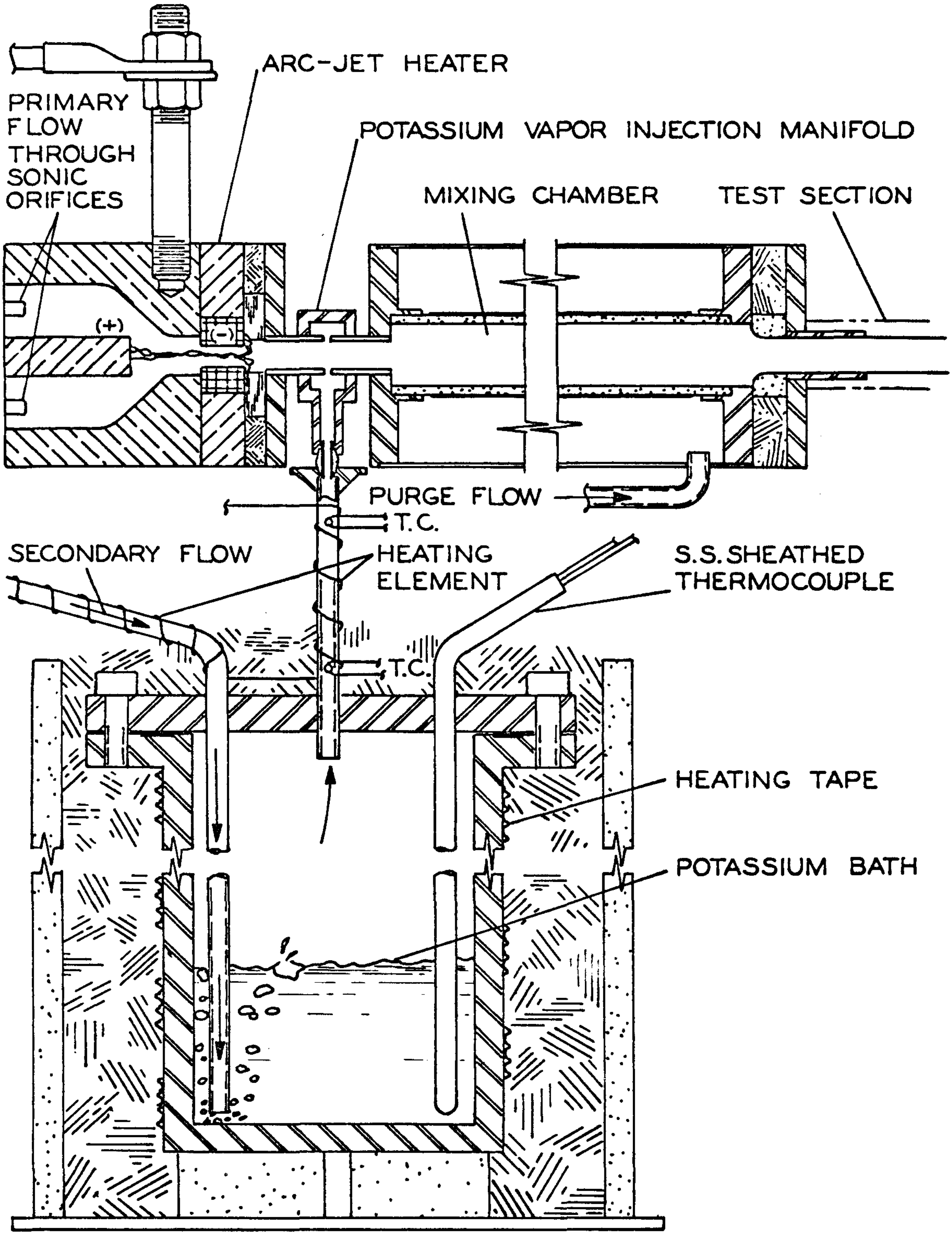

FIG. 28 ARC-JET HEATER AND FLOW MIXING APPARATUS

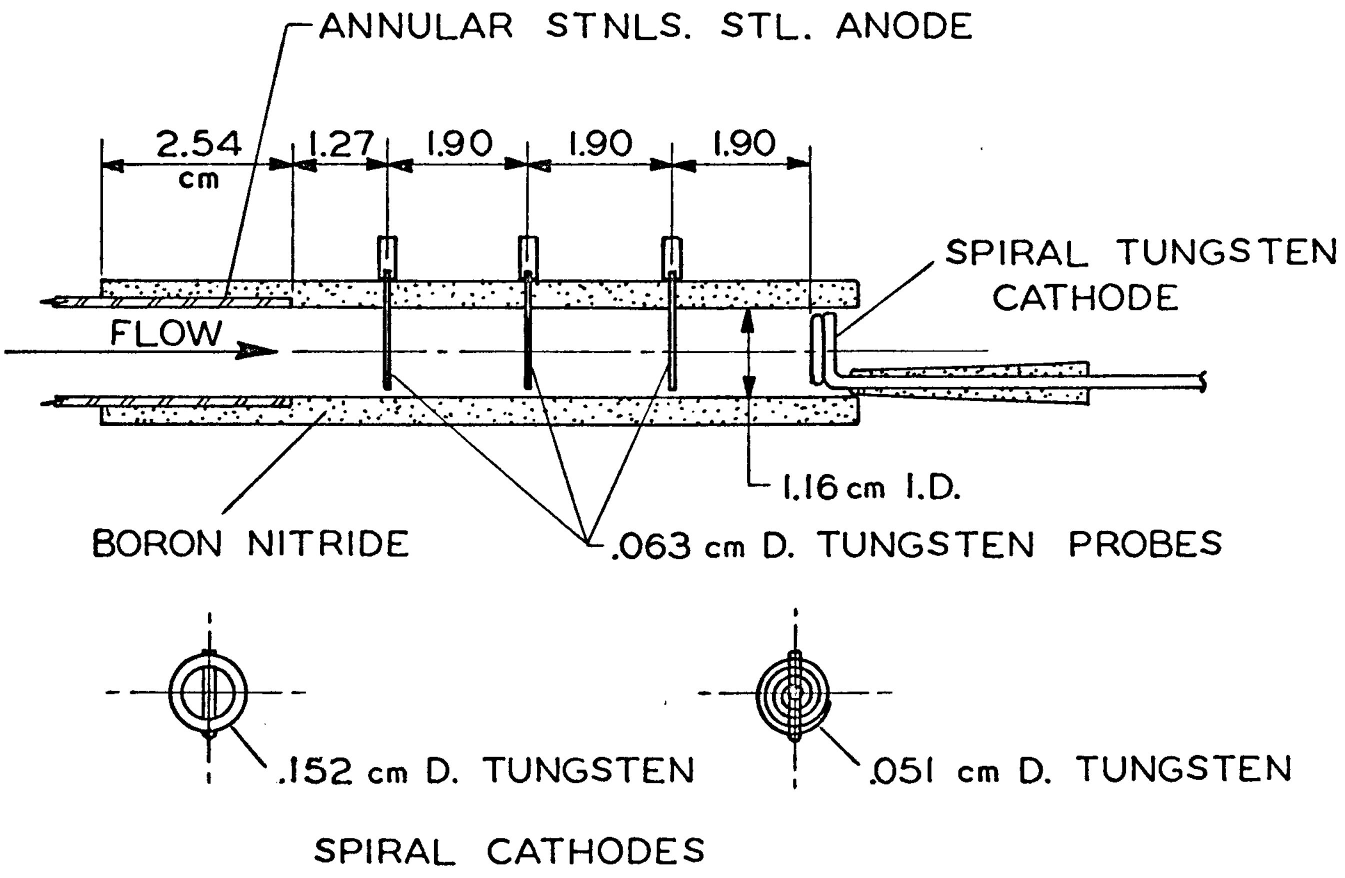

FIG. 29 TEST SECTION WITH SPIRAL ROD CATHODE

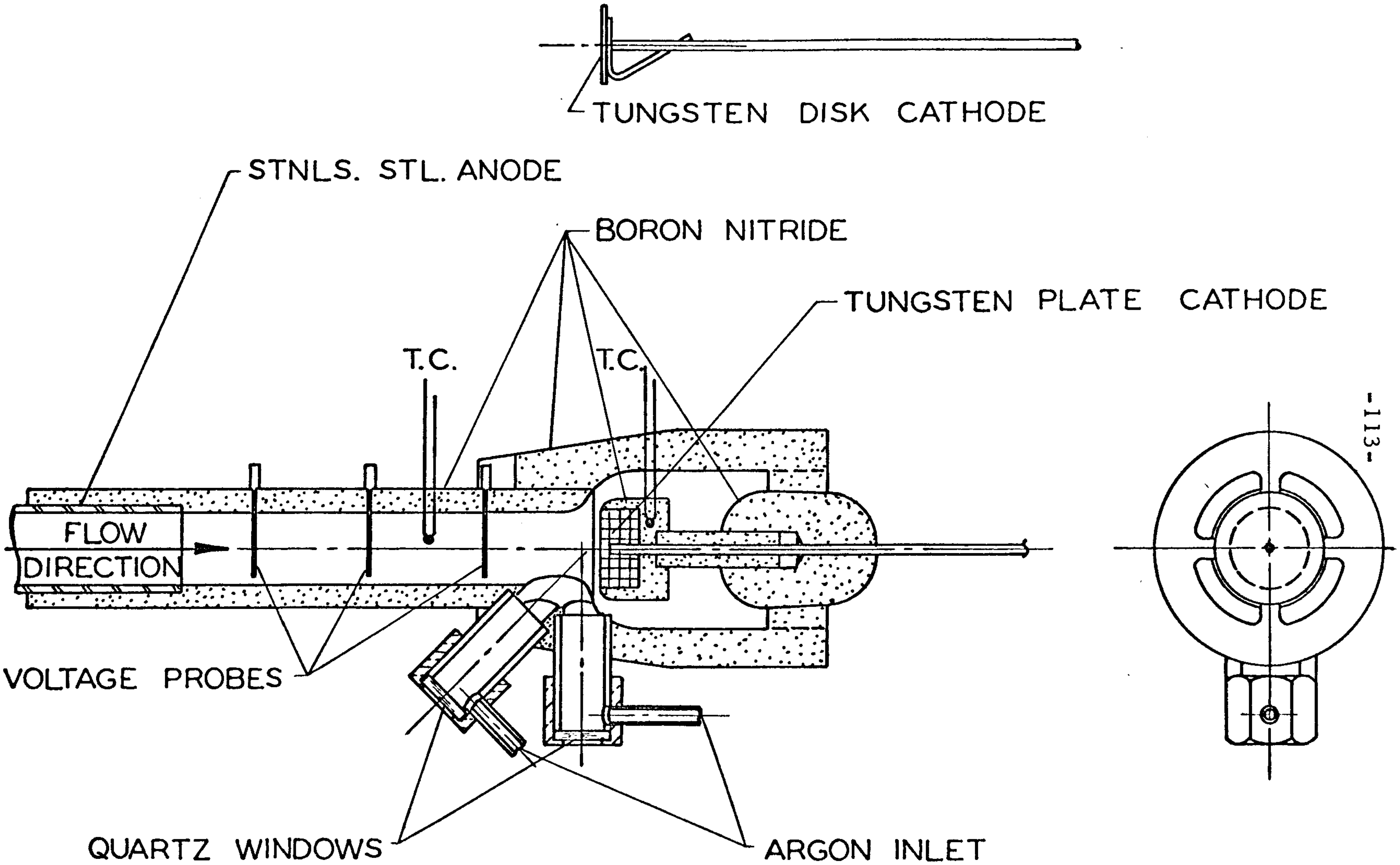

FIG. 30 TEST SECTION WITH STAGNATION FLOW CATHODE

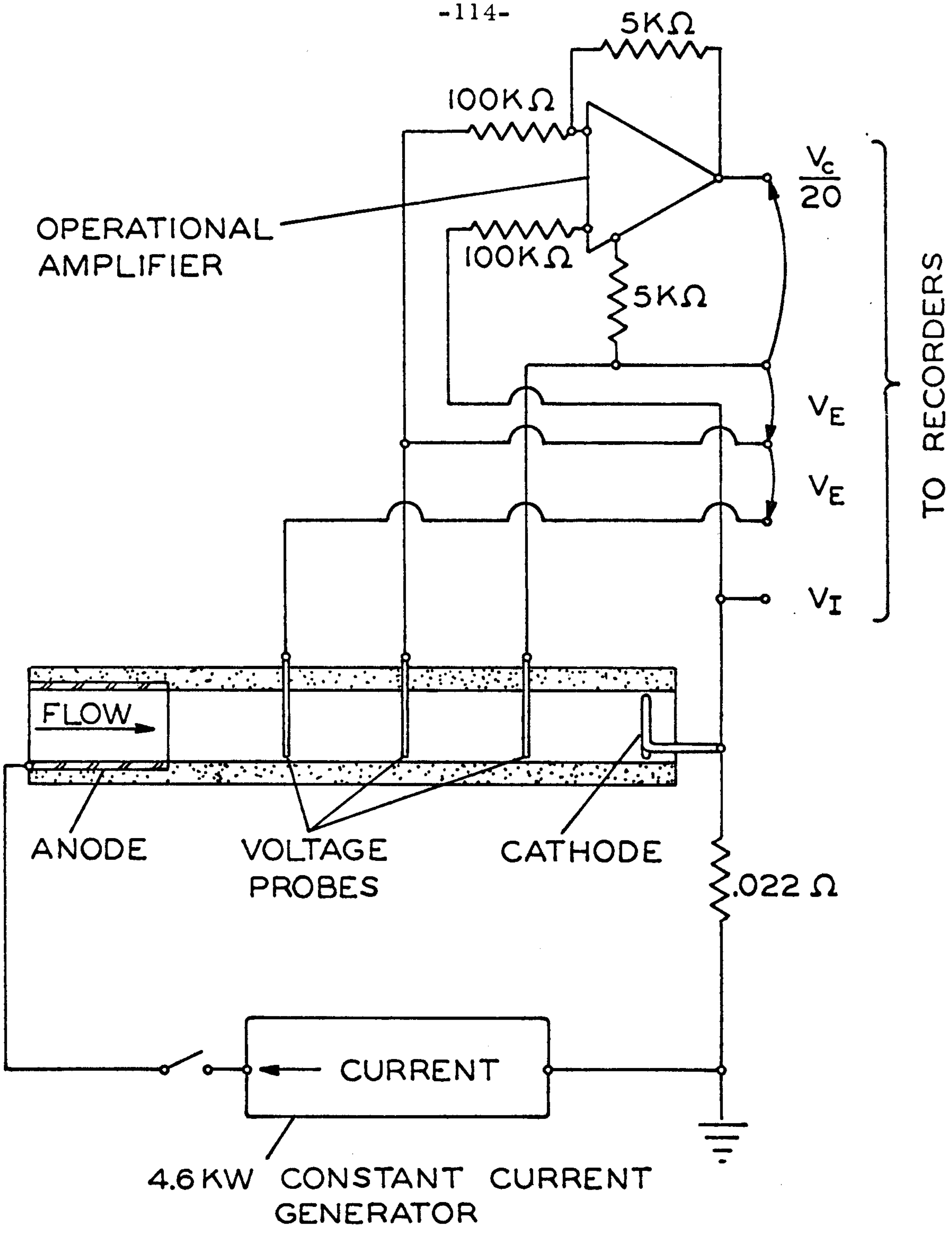

FIG. 31 SCHEMATIC OF ELECTRIC CIRCUIT

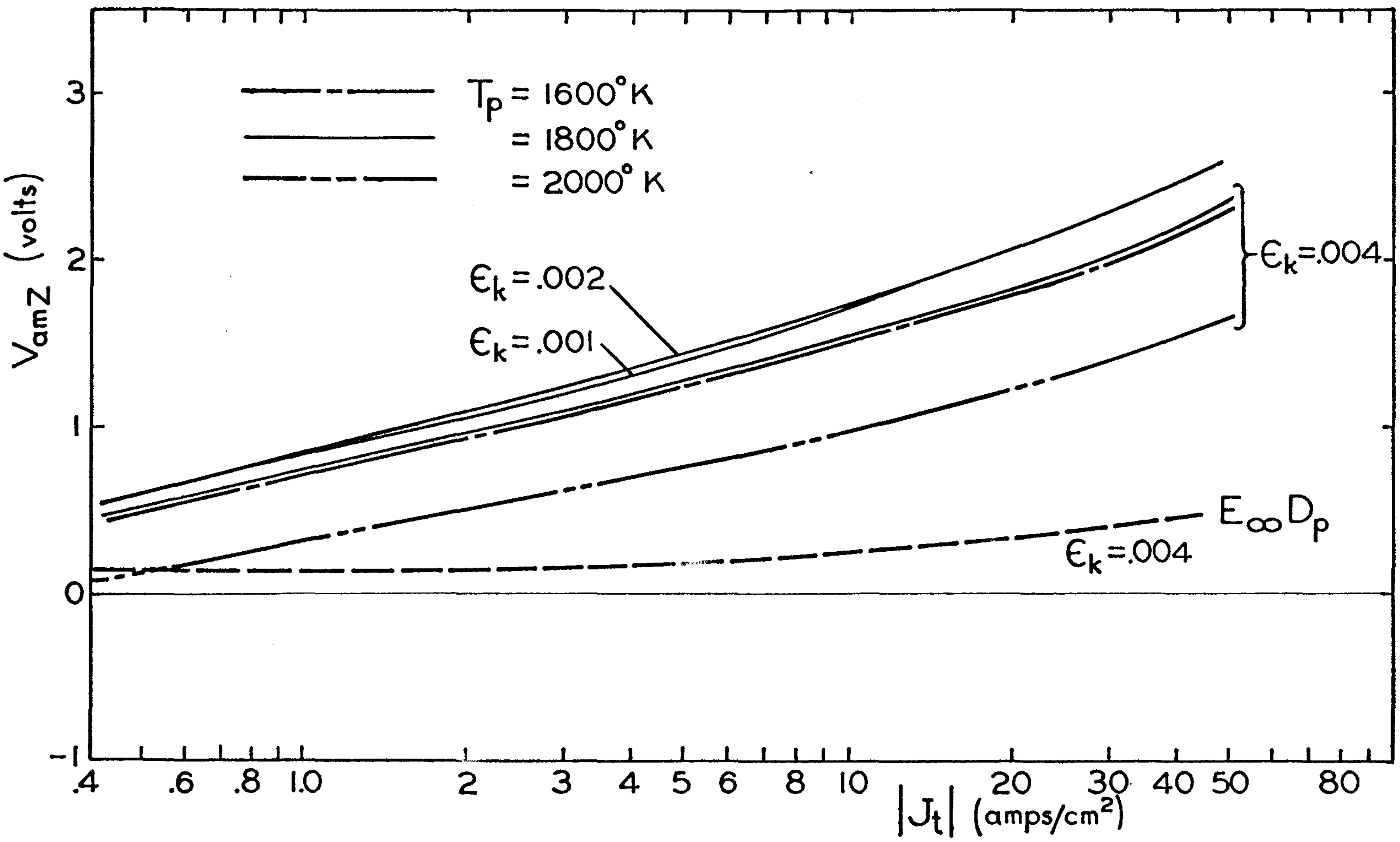

FIG. 32 FLOATING PROBE VOLTAGE CORRECTION

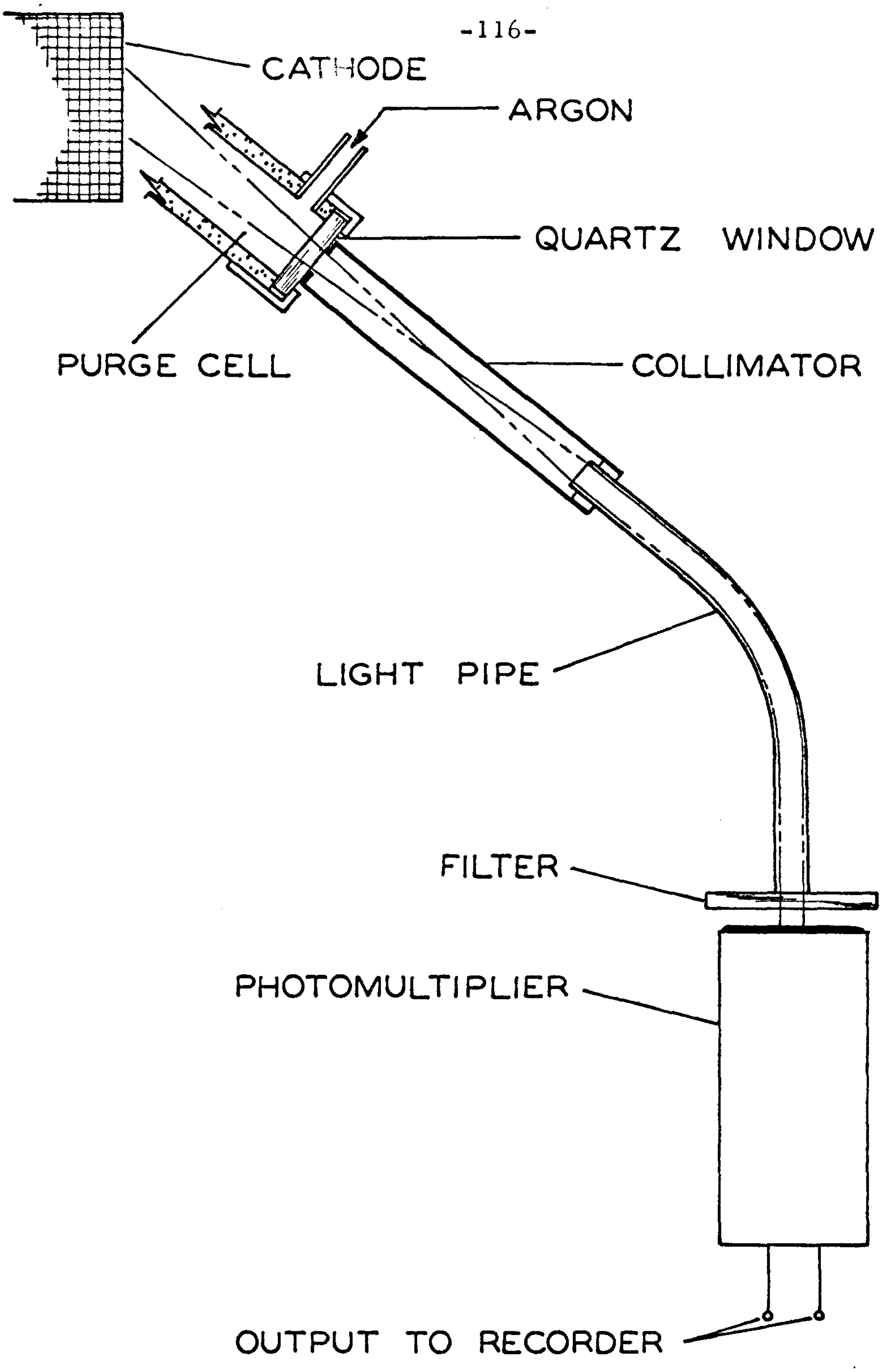

FIG. 33 SCHEMATIC OF OPTICAL SYSTEM

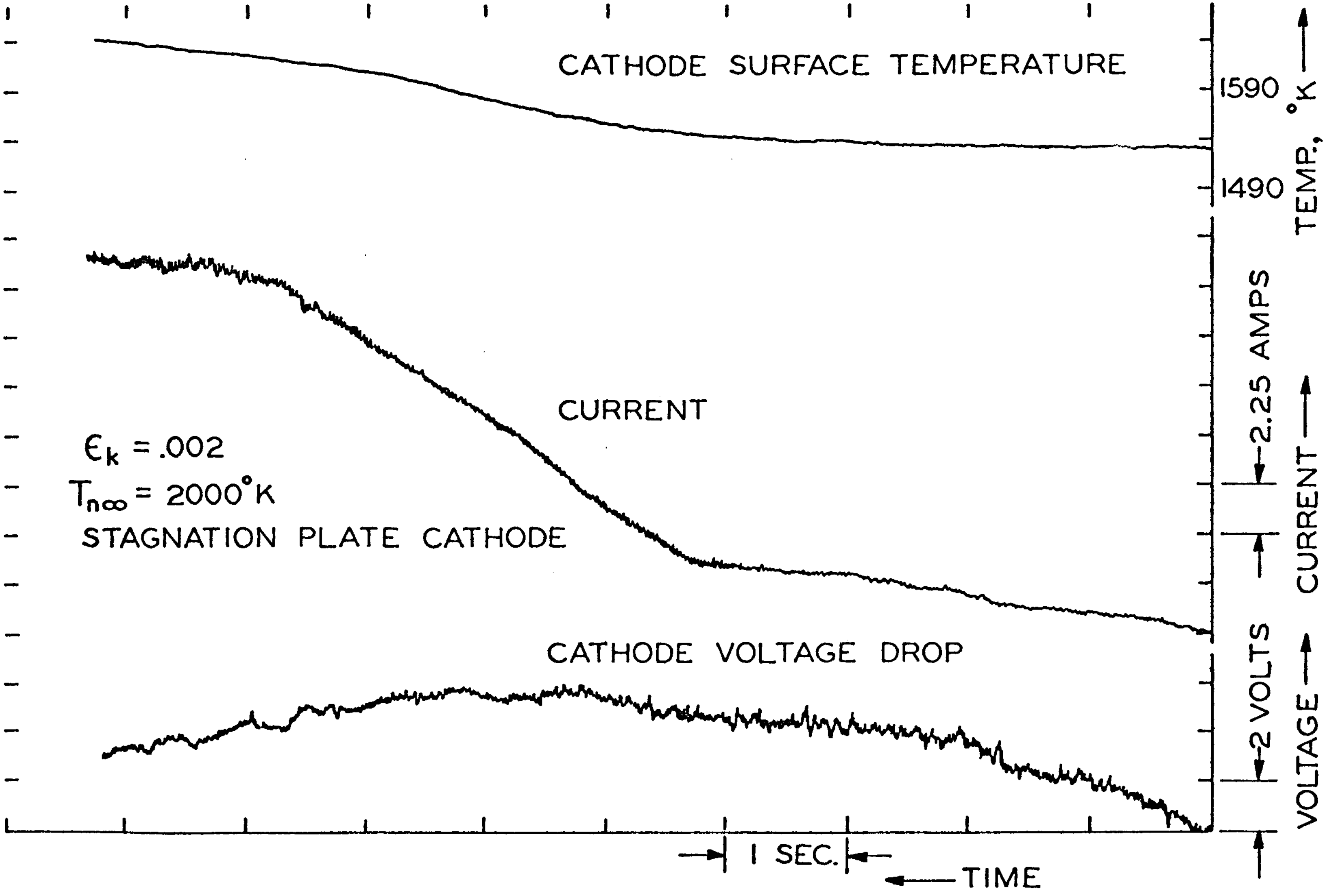

FIG. 34a STRIP CHART RECORDER DATA

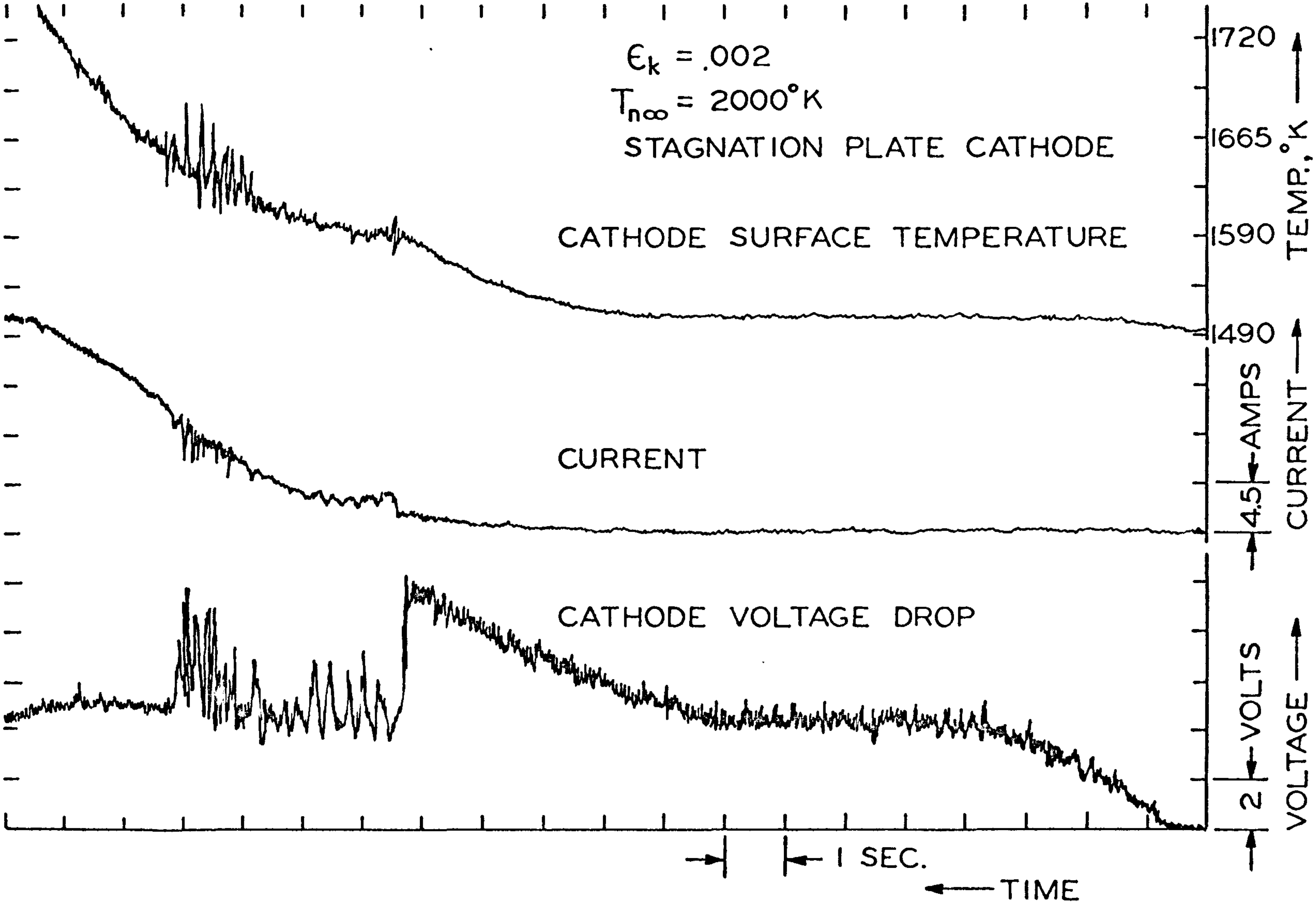

FIG. 34 b STRIP CHART RECORDER DATA

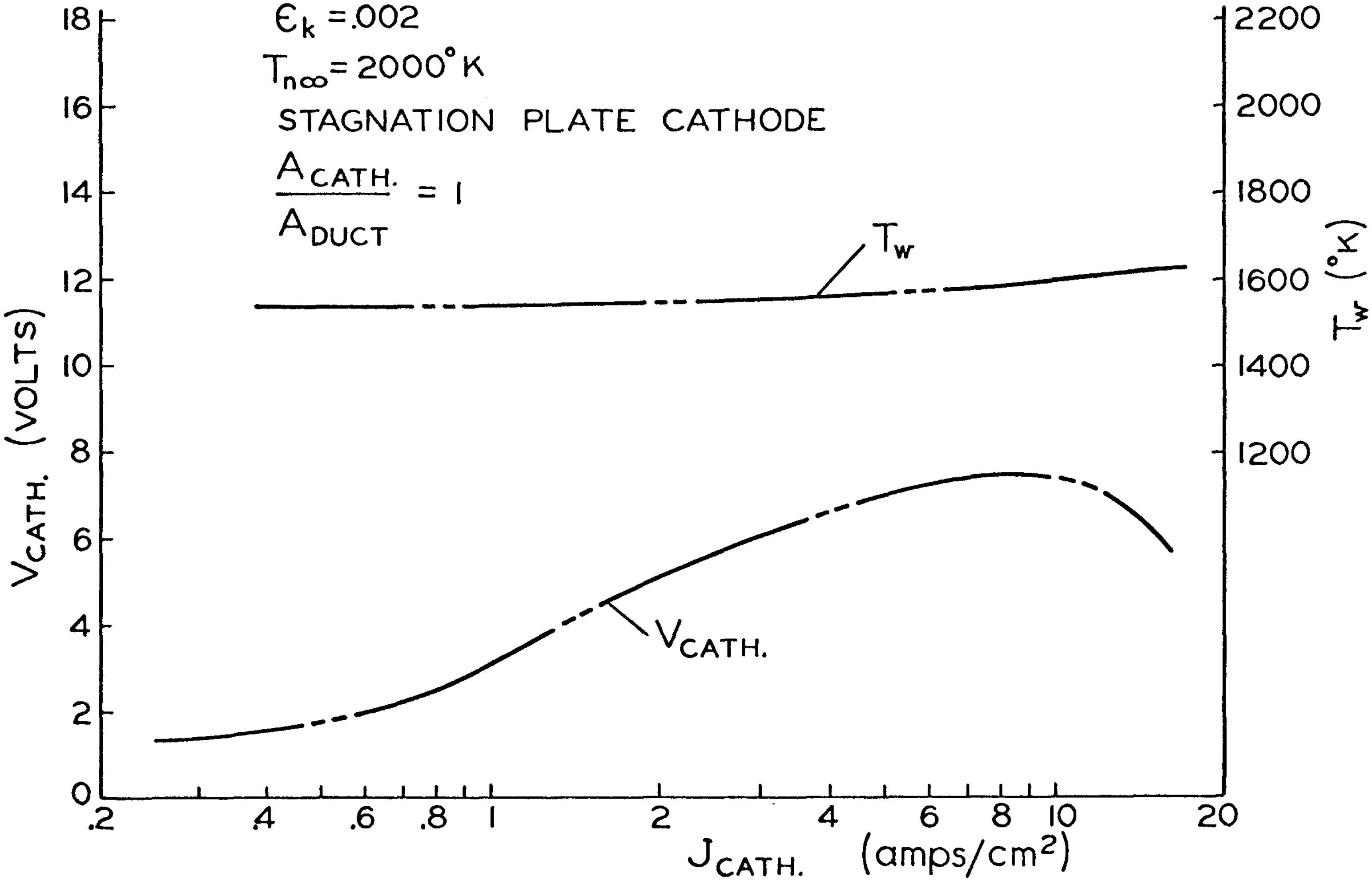

FIG. 35a EXPERIMENTAL CURRENT-VOLTAGE CHARACTERISTIC

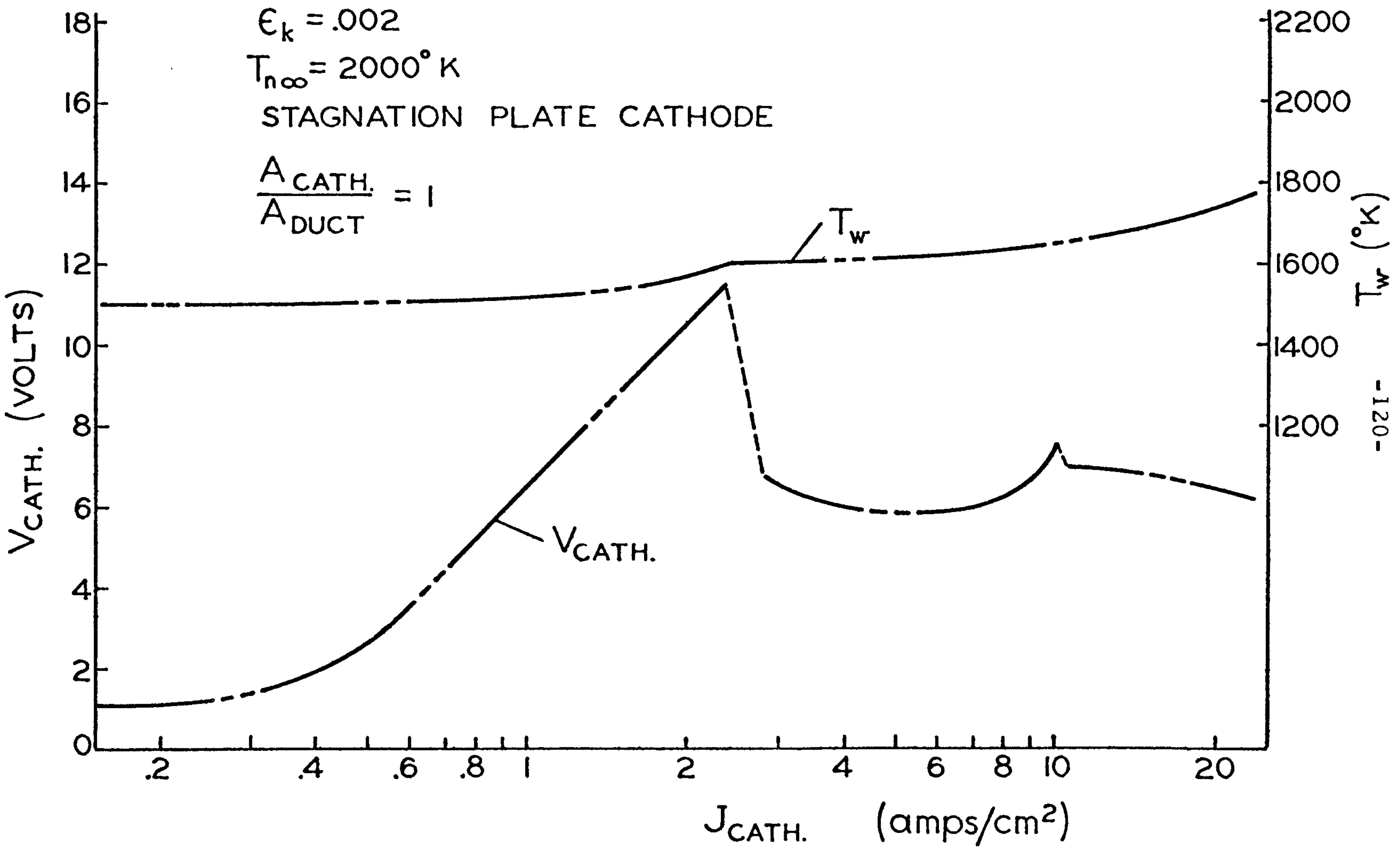

FIG. 35b EXPERIMENTAL CURRENT VOLTAGE CHARACTERISTIC

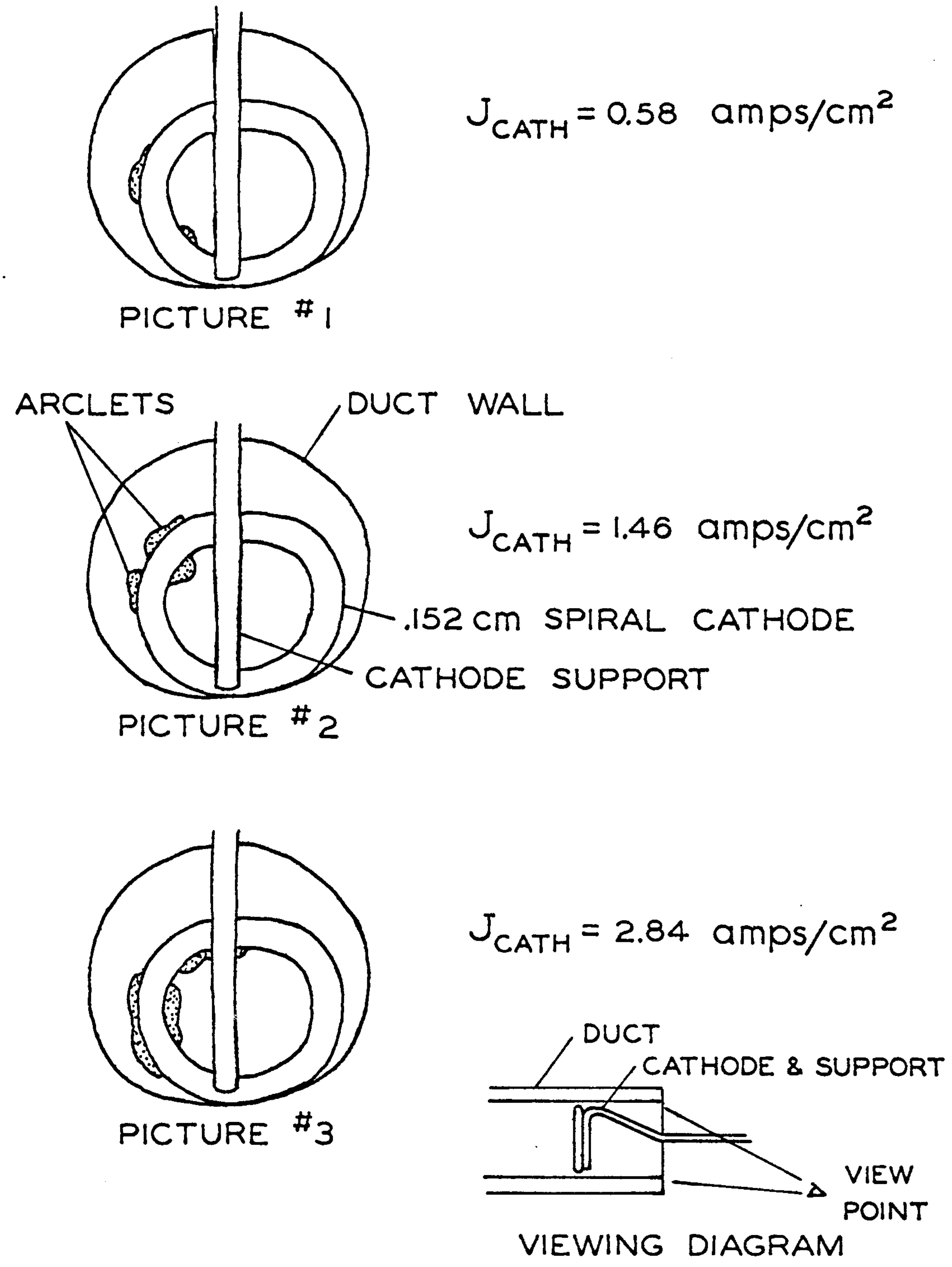

FIG. 36 CATHODE PICTURED DURING ARCLET MODES

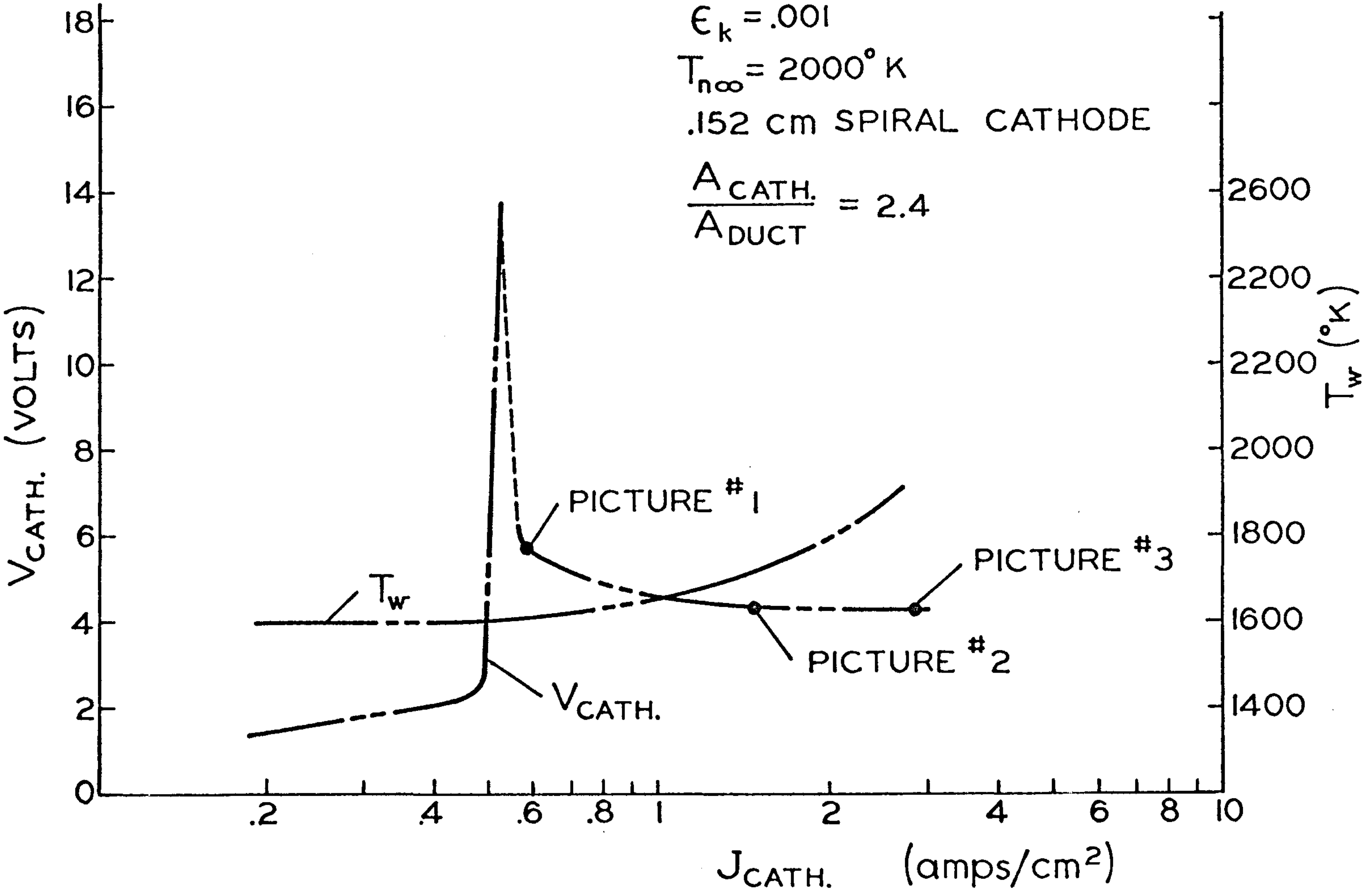

FIG. 37 EXPERIMENTAL CURRENT-VOLTAGE CHARACTERISTIC

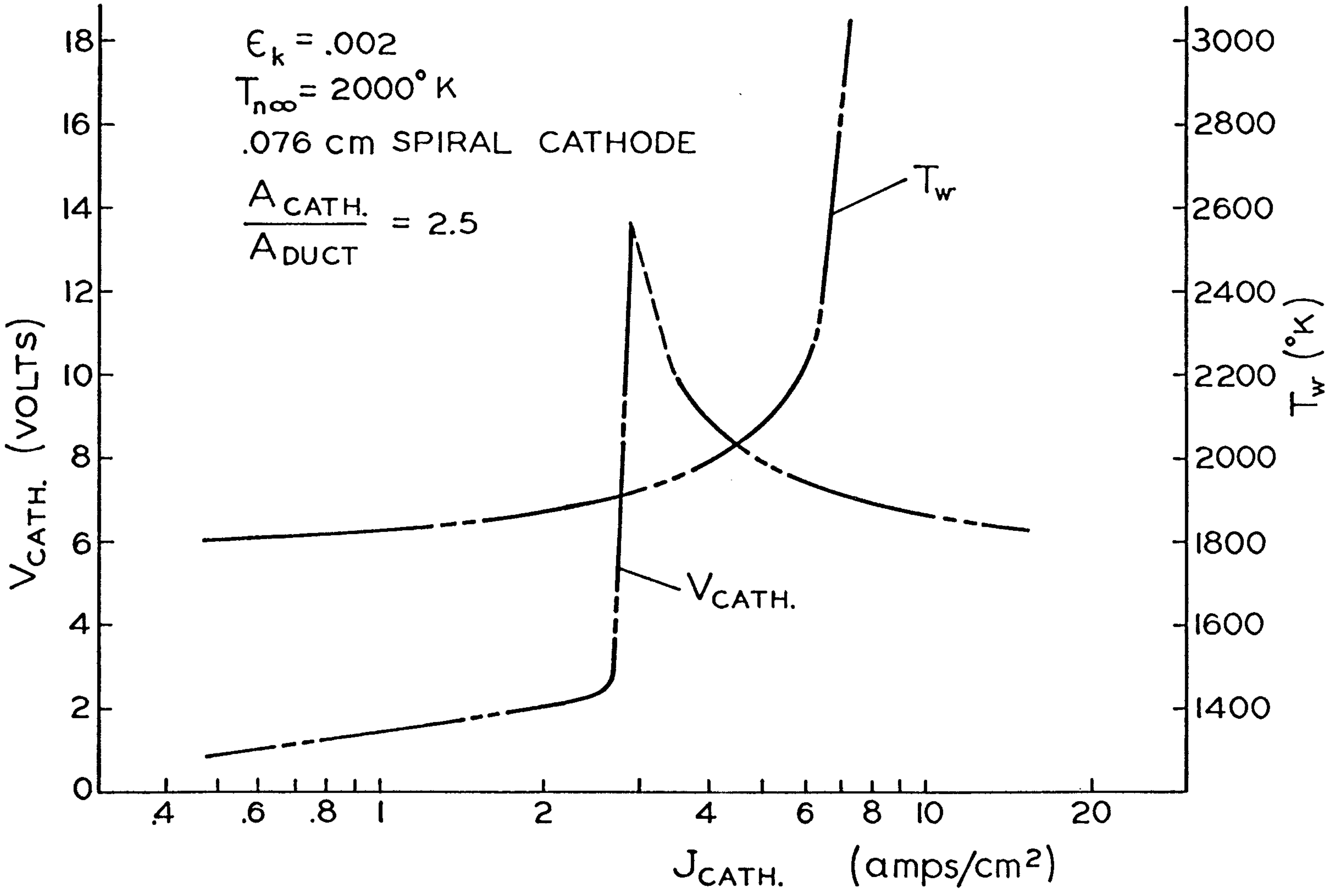

FIG. 38 EXPERIMENTAL CURRENT-VOLTAGE CHARACTERISTIC

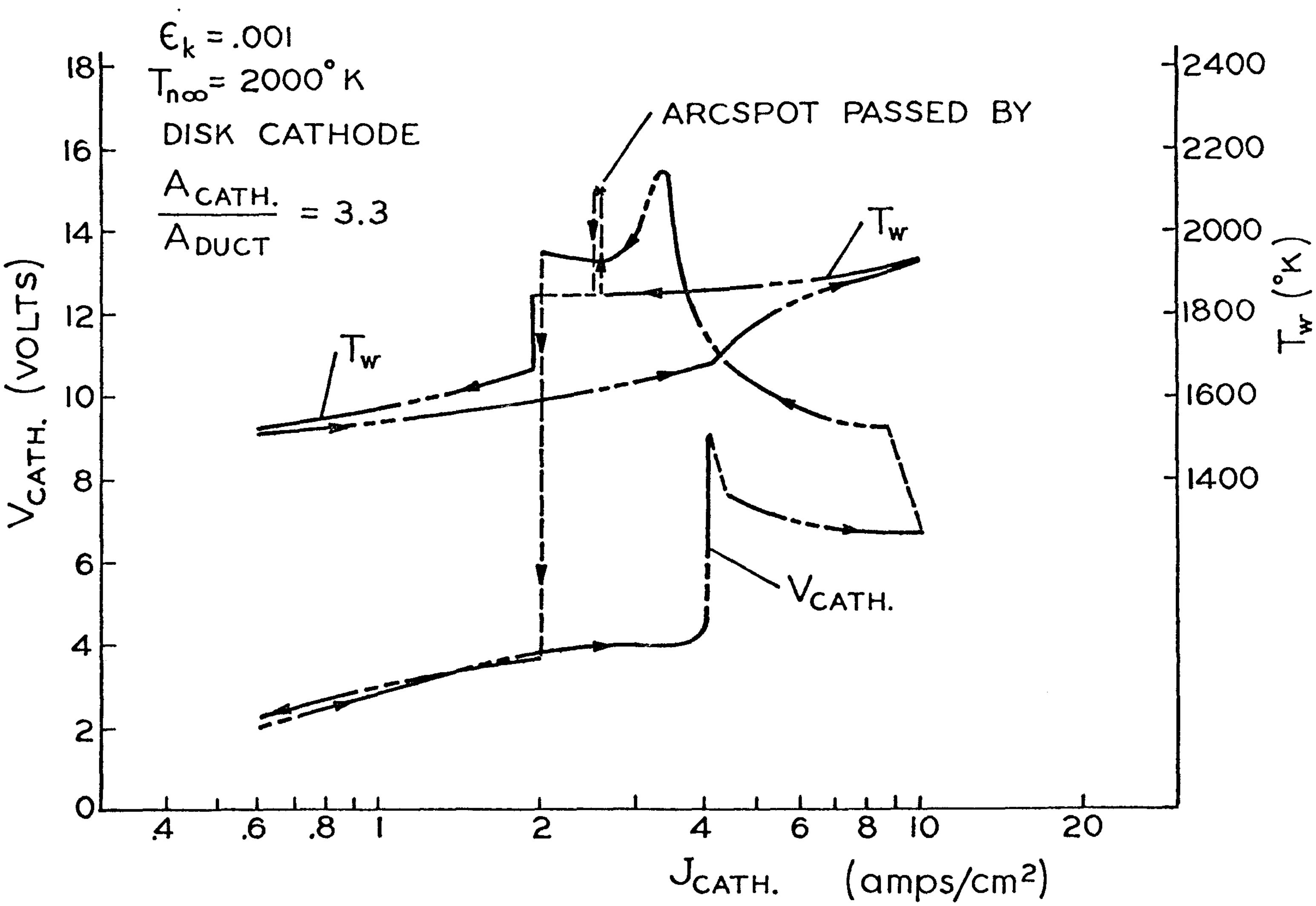

FIG. 39 EXPERIMENTAL CURRENT-VOLTAGE CHARACTERISTIC

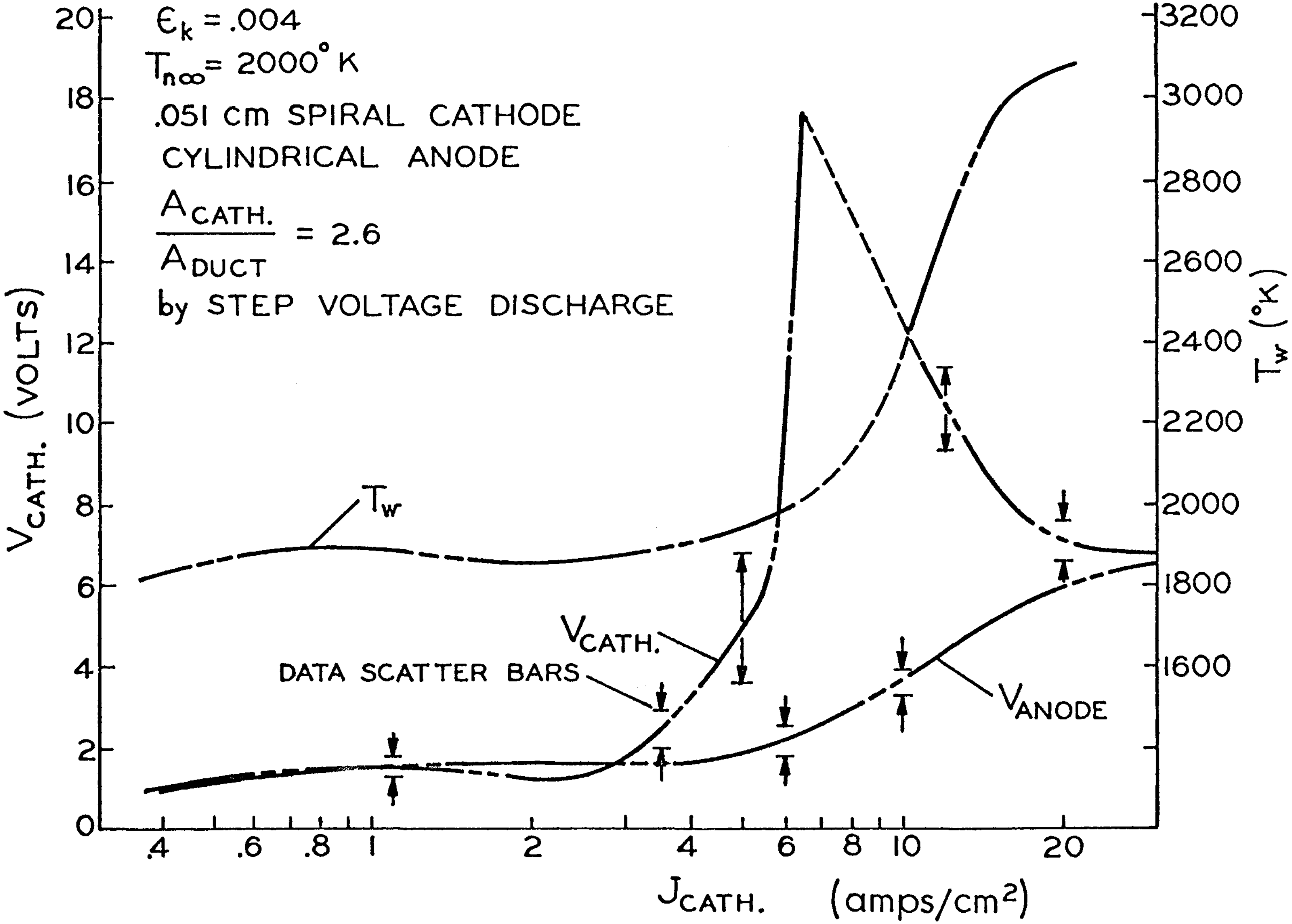

FIG. 40 EXPERIMENTAL CURRENT-VOLTAGE CHARACTERISTIC

TABLE 3

Code for Data Symbols Used for Figures 41 through 45

Basic Symbol	Seed Fraction
△	.0005
○	.001
▽	.002
□	.004
◺	.006

Arclet Formation Code for Typical Basic Symbol

Symbol	Meaning
□	arclet breakdown with current increasing
⊠	arclet stopped with current increasing
	arclet stopped with current decreasing
-⊟-5	maximum voltage drop of 5 volts for current sweep that did not result in an arclet breakdown
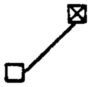	arclet occurred between these two points for one current sweep

Cathode Type Code for Typical Basic Symbol

Symbol	Cathode Type	A_{cath}/A_{duct}
⁻□	.051 cm spiral	2.6
-□	.076 cm spiral	2.6
_□	.152 cm spiral	2.4

TABLE 3 (continued)

Symbol	Cathode Type	A_{cath}/A_{duct}
□‾	disk	3.3
□	stagnation plate	1

All data were taken by the continuous current sweep technique, with the exception of the .051 cm spiral data which were taken by the step function voltage method.

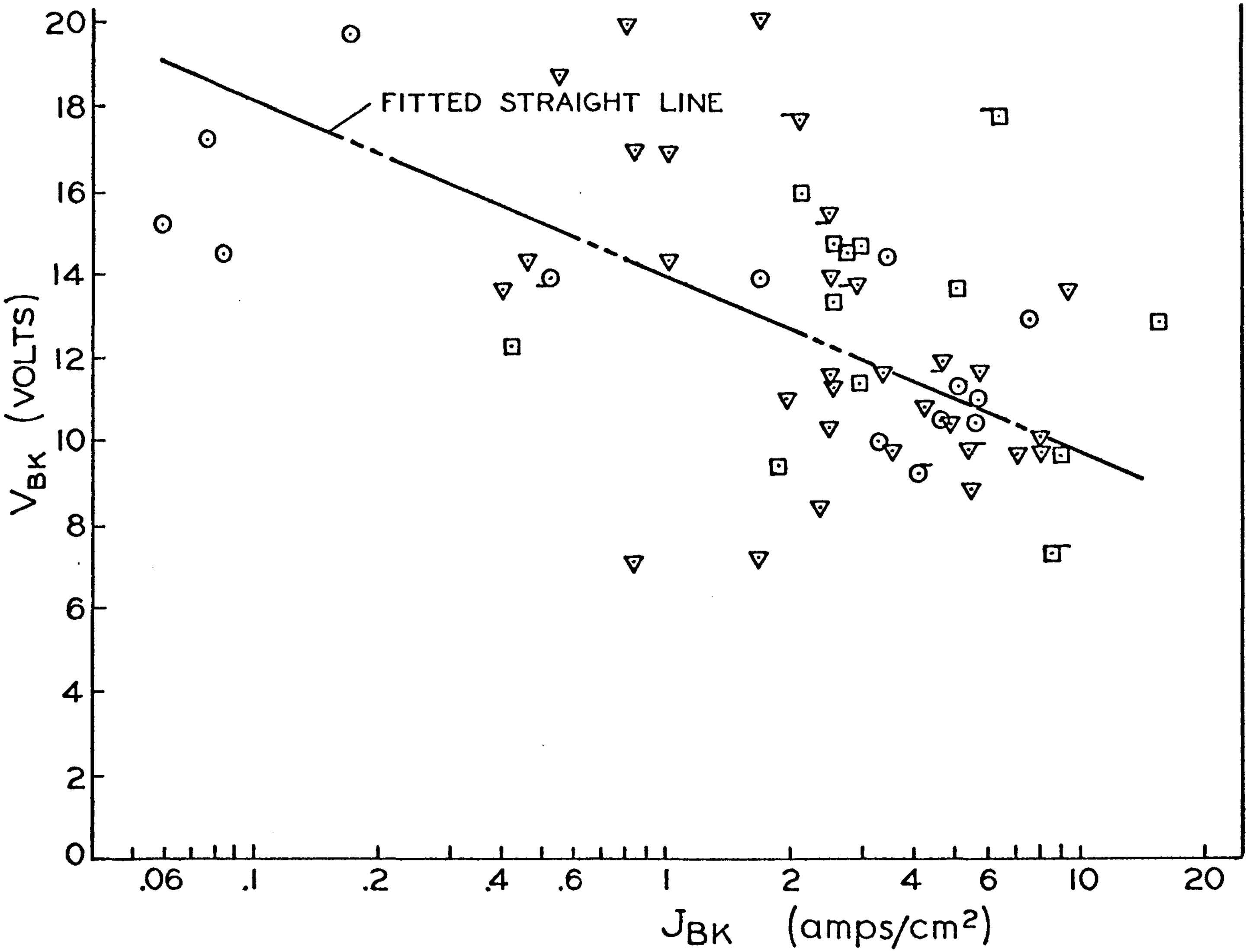

FIG. 41 ARCLET BREAKDOWN VOLTAGES

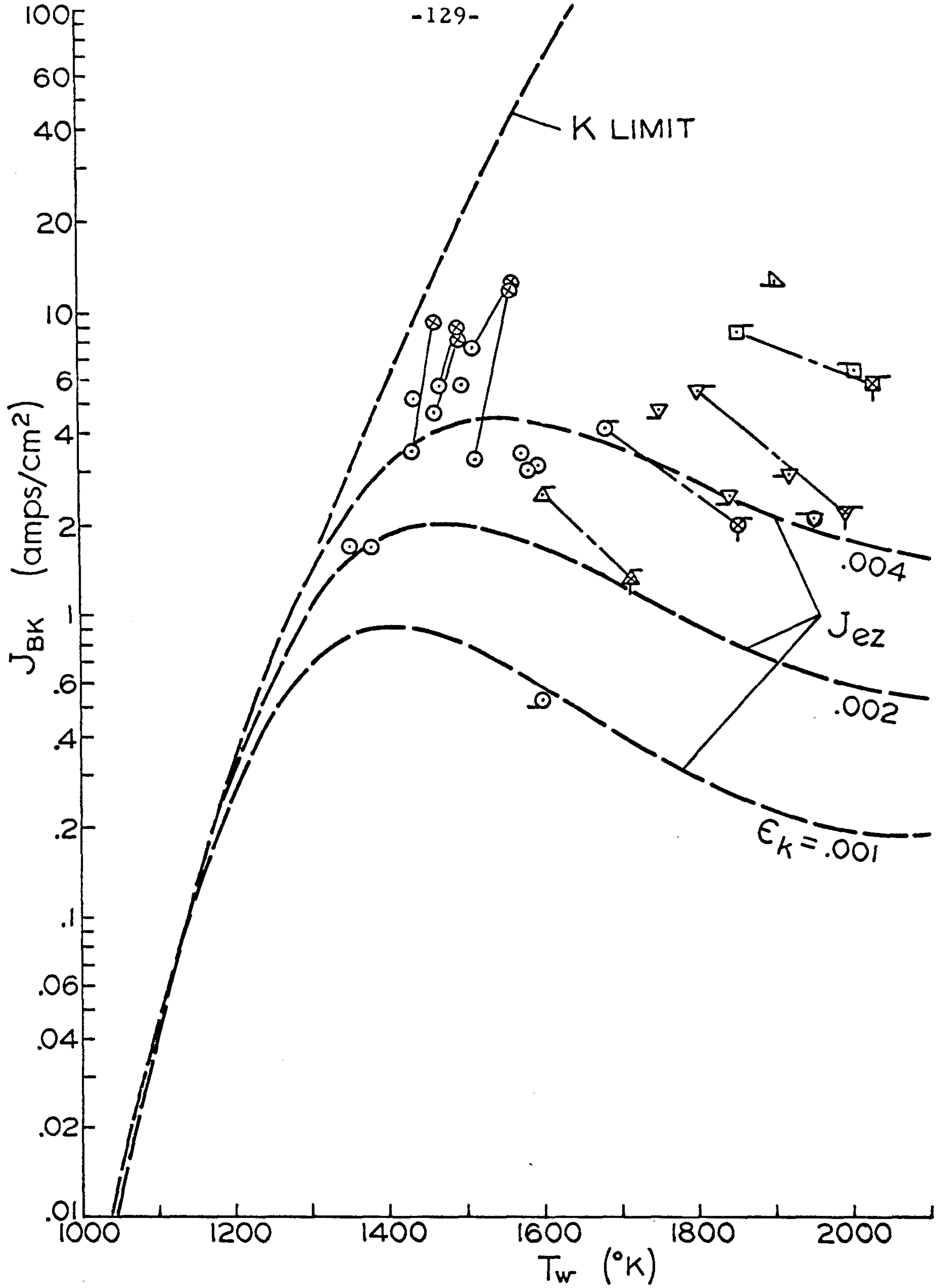

FIG. 42 BREAKDOWN CURRENT DENSITIES FOR VARIOUS CATHODE GEOMETRIES

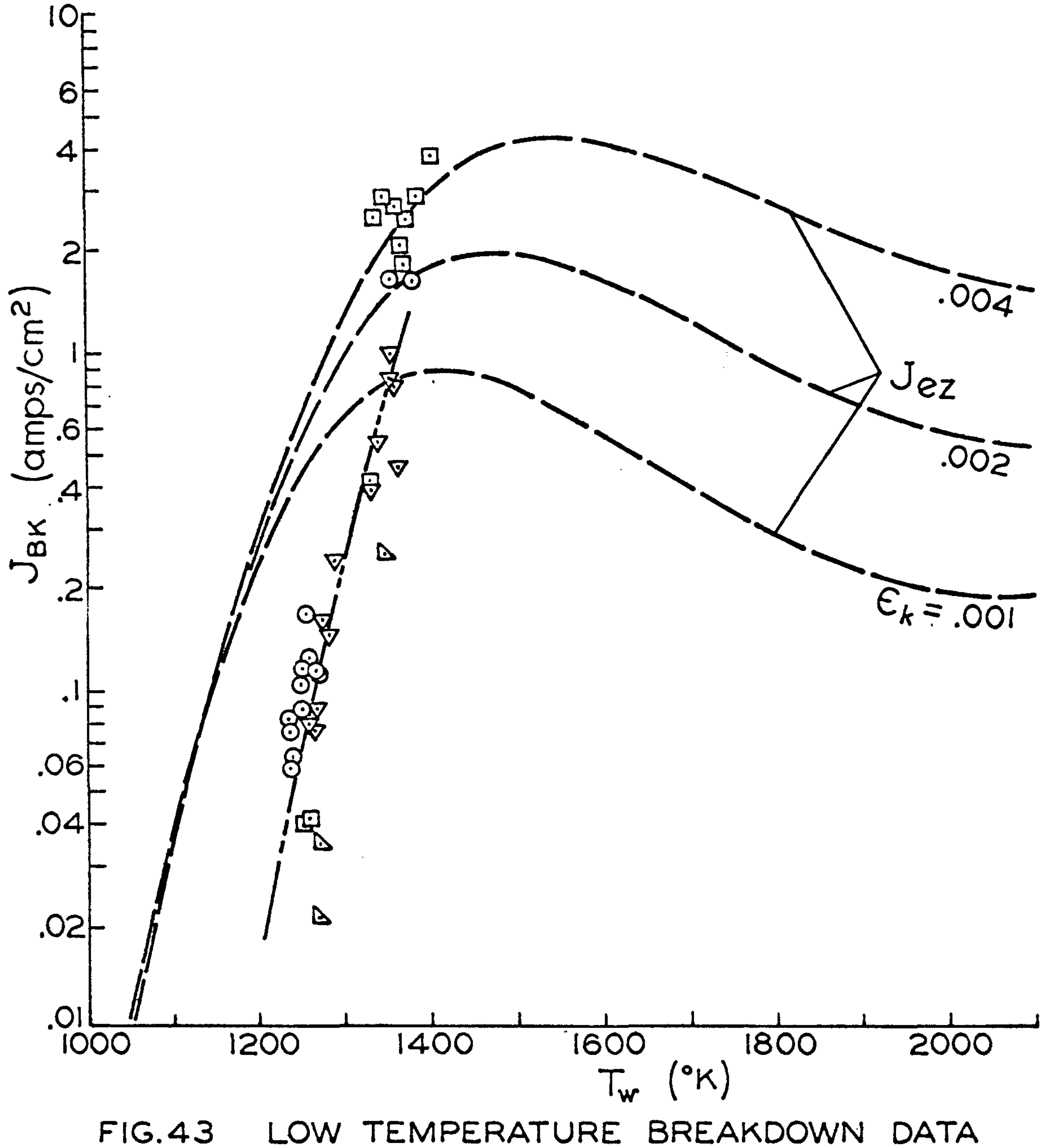

FIG. 43 LOW TEMPERATURE BREAKDOWN DATA

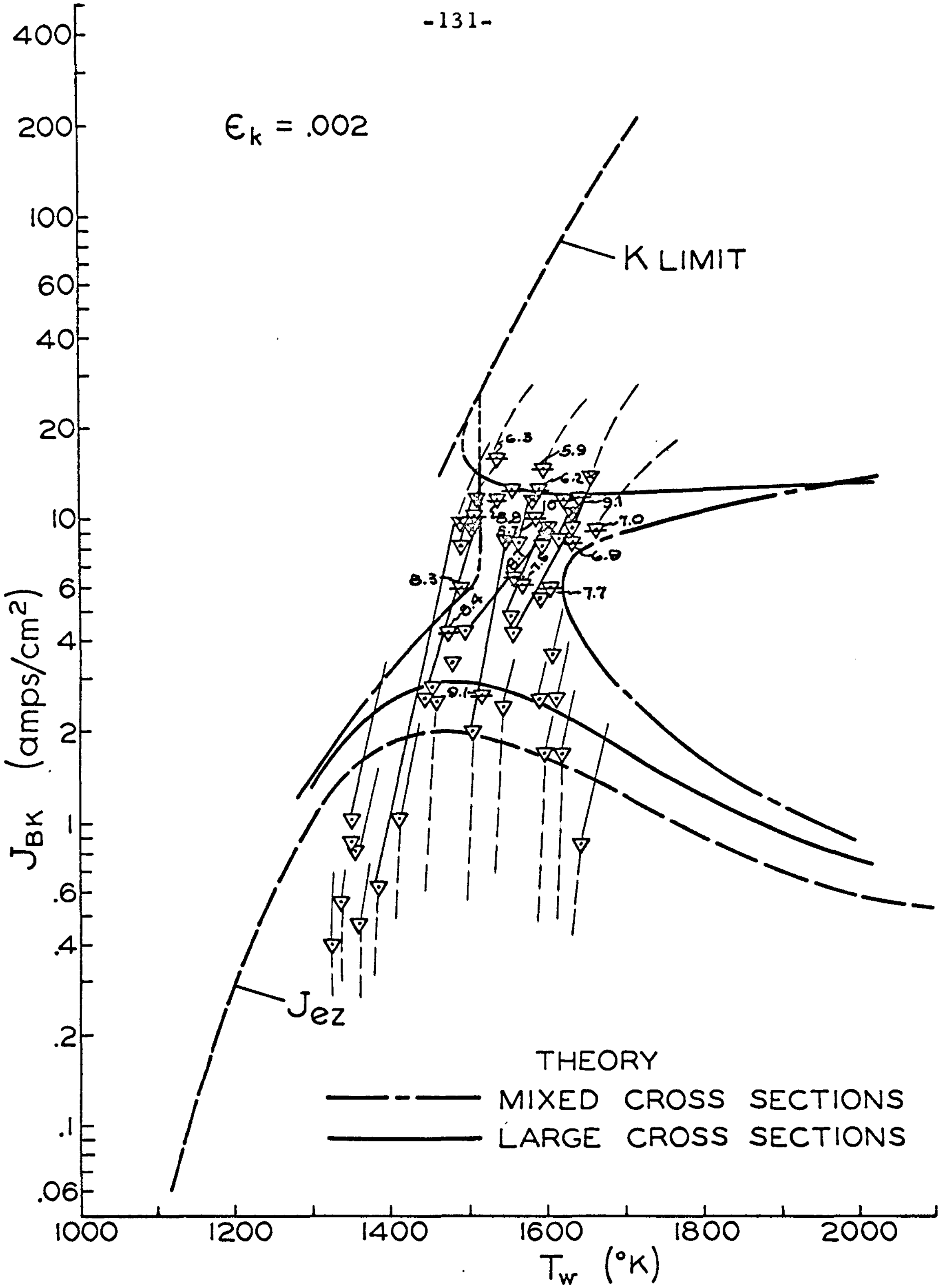

FIG. 44 THERMIONIC REGIME COMPARISON WITH DATA

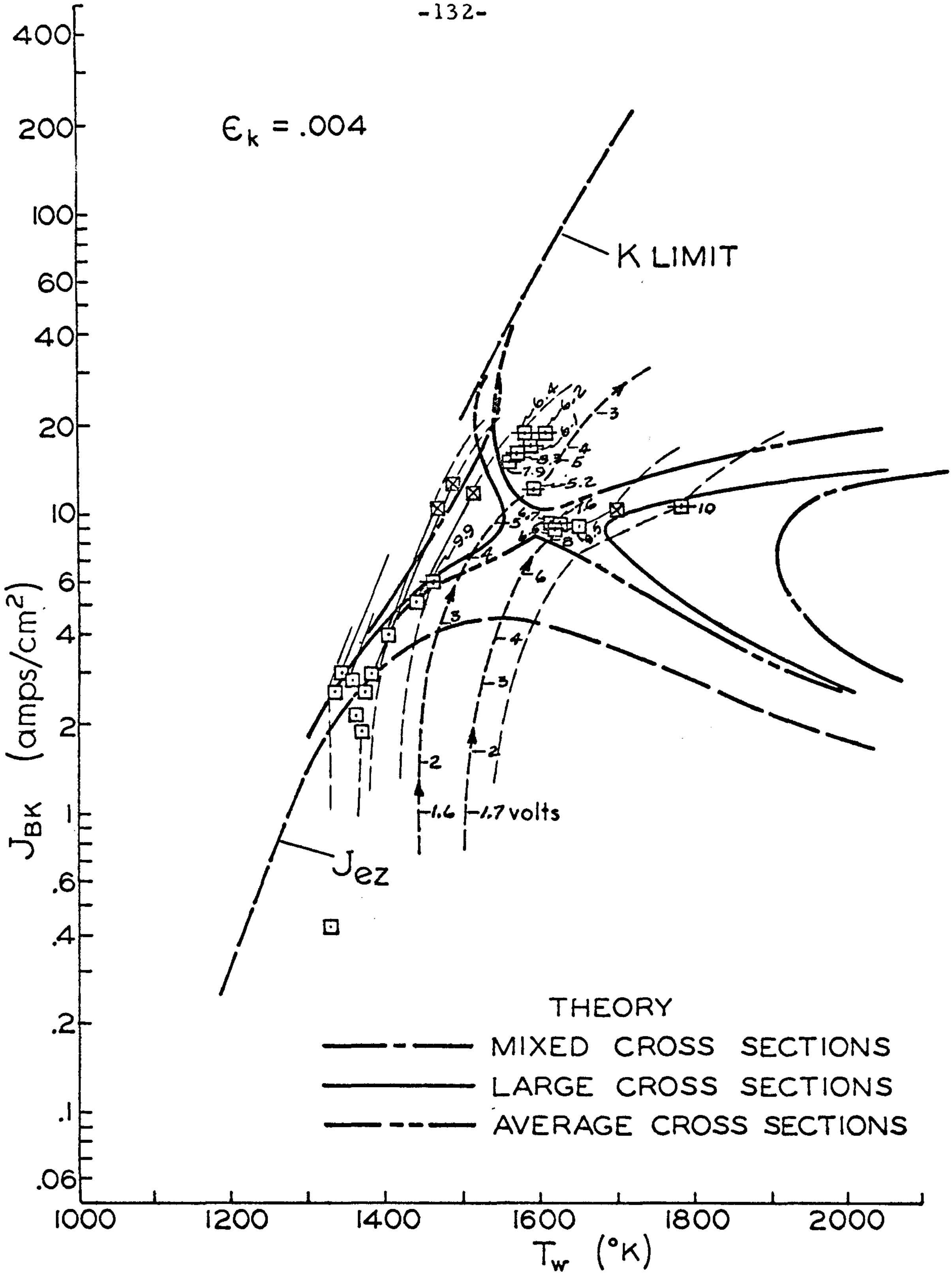

FIG. 45 THERMIONIC REGIME COMPARISON WITH DATA

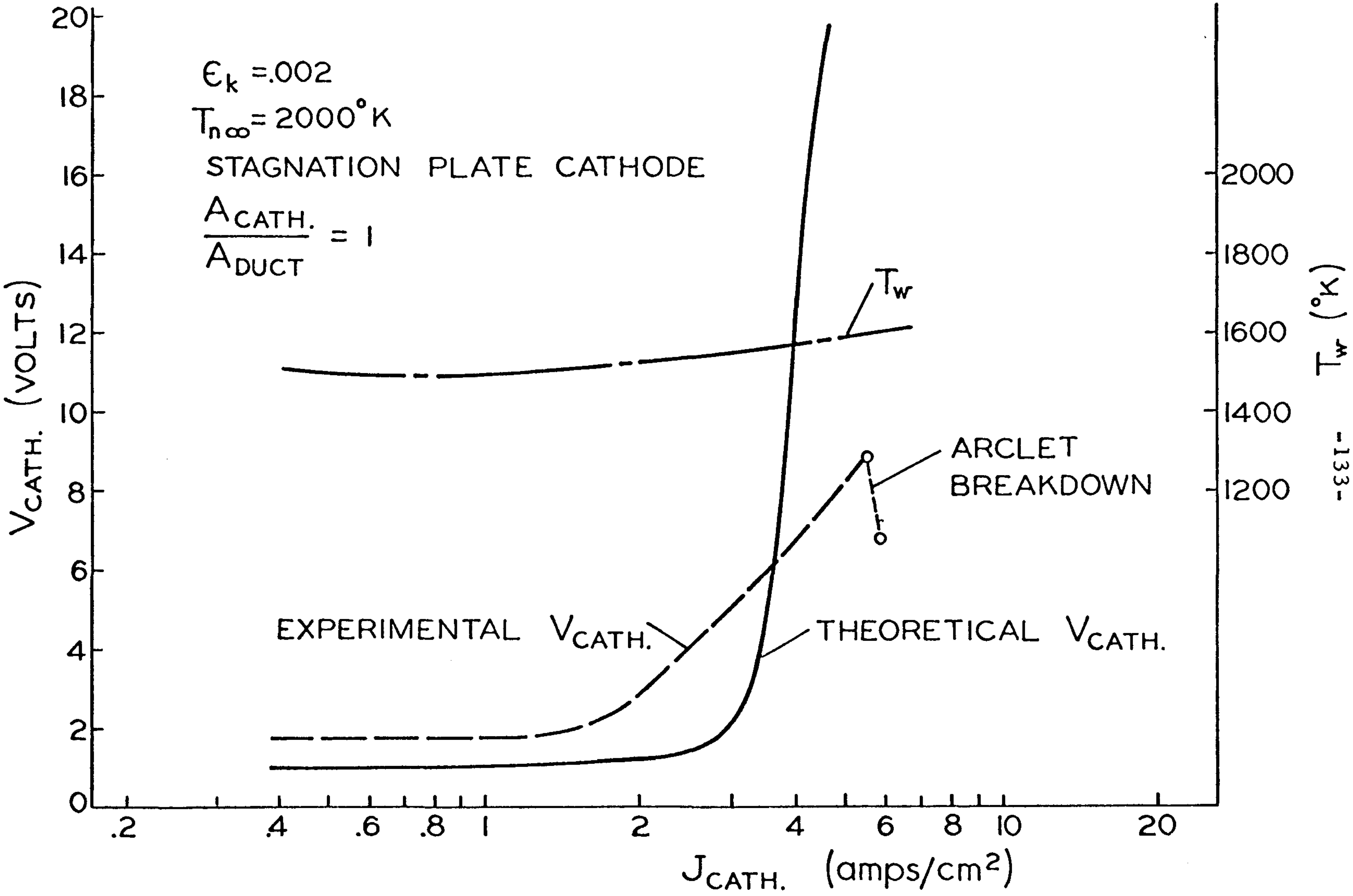

FIG. 46 COMPARISON OF CURRENT-VOLTAGE CHARACTERISTICS

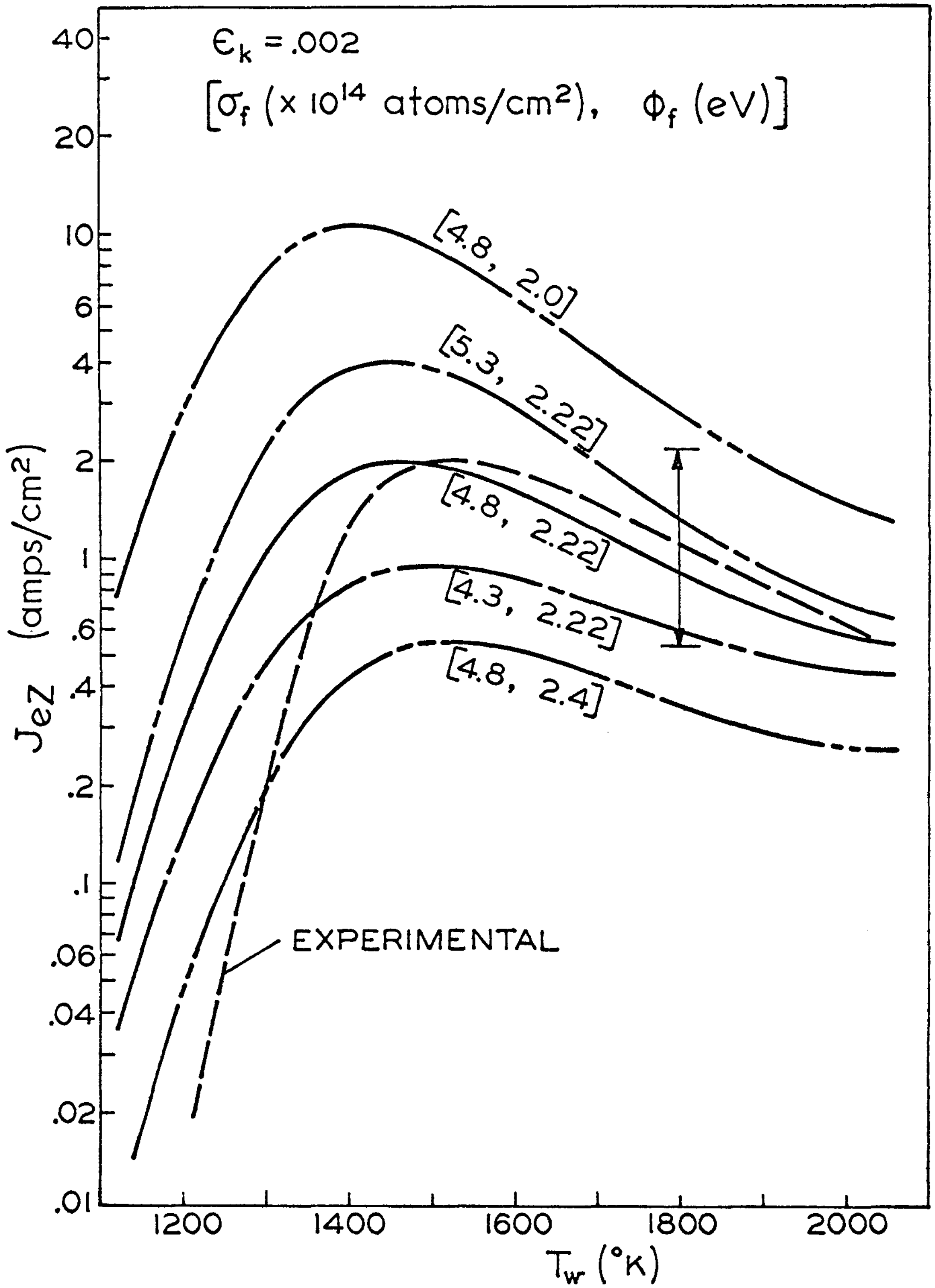

FIG. 47 COMPARISON OF SURFACE ELECTRON EMISSION

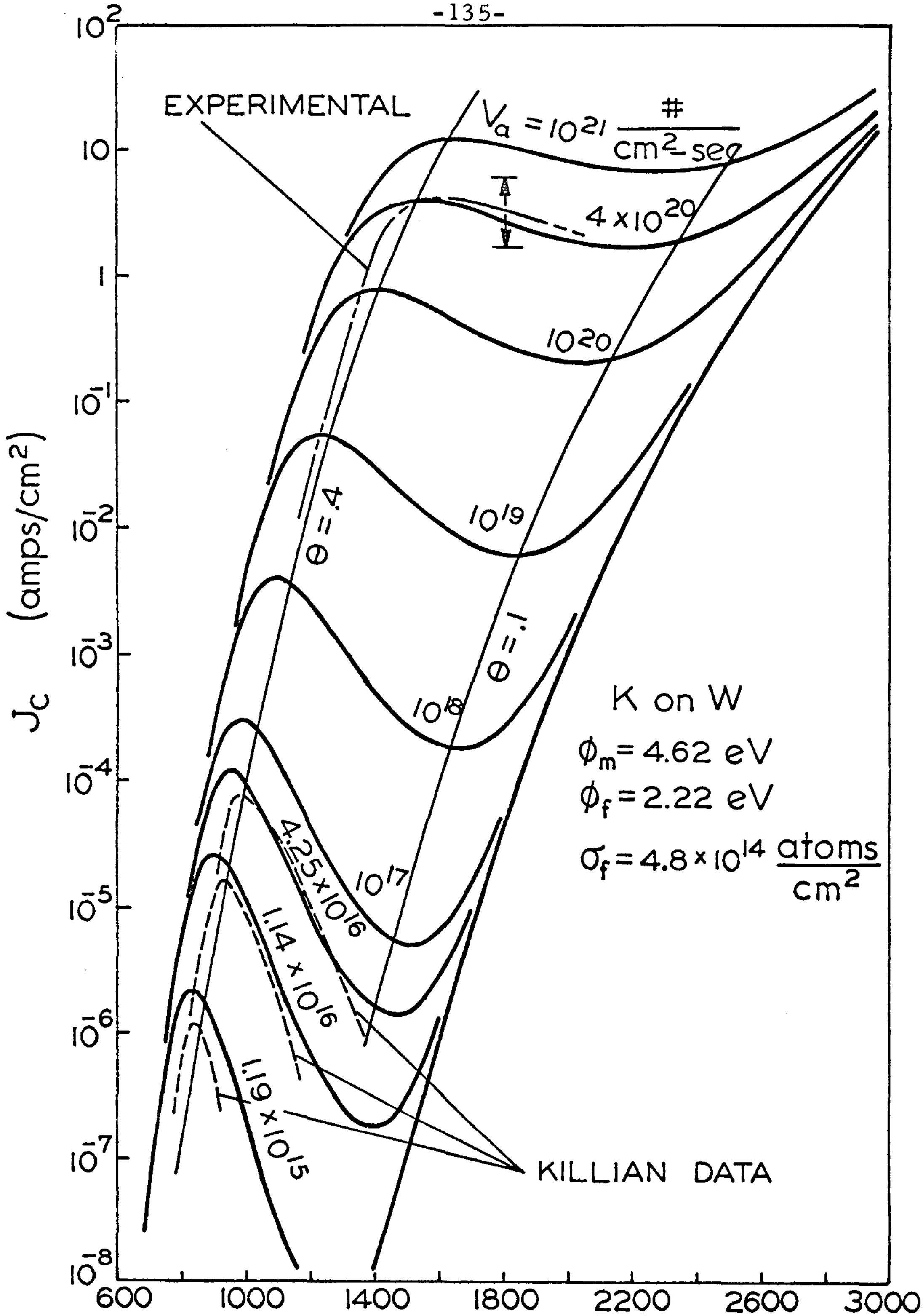

FIG.48 ELECTRON EMISSION
S-CURVES COMPARISON

NOMENCLATURE

a	stagnation flow constant
A	$= G_w + \varepsilon K_w$
A_t	$= \nu_e/\nu_{eZ}$, cathode augmentation ratio
A_E	Schottky augmentation ratio
B	$= G_w - K_w$
C_∞	matching constant
$\bar{C}_s$	average thermal speed of s species
D_p	diameter of voltage probe
D_s	mutual diffusion coefficient of s species
e	absolute value of electron charge
$\vec{E}$	electric field
f	velocity distribution function
F	scaled potential drop
g_s	statistical weight of ground state of s species
G	scaled electron number density
h	Planck's constant
$h_{e\infty}$	Debye length in bulk plasma
H	stagnation jet height
I	$\equiv \partial N/\partial\eta\|_{\eta=\eta_o}$
$\vec{j}_e$	electronic current density
J_{BK}	transition current density
J_{cath}	cathode current
J_{eZ}	$\equiv e\nu_{eZ}$
J_e	electron current density

J_i	ion current density
J_L	thermionic limiting current density
$J_L^{30\%}$	current density at which $A_E = 0.3$
J_t	total current density
k	Boltzmann's constant
K	scaled ion number density
L	characteristic length
m_s	particle mass of s species
n_s	particle number density of s species
$\dot{n}_s$	net production rate of s species per unit volume
n_{saha}	equilibrium electron number density
$\vec{n}$	unit vector normal to electrode surface
N_o	ambipolar matching number density
N_s	$= n_s / n_{e\infty}$
$\dot{N}$	$= \epsilon L^2 / (D_{io} n_{e\infty}) \, \dot{n}$
p	static pressure
P_s	$= \Gamma_{sw} / \nu_s$, species current fraction
Pr	Prandtl number
q_s	particle charge of s species
$\vec{q}_e$	electronic heat flux
Q_n^s	momentum transfer cross section for elastic collisions of s species with neutral species n
r	radial coordinate from stagnation electrode center
$\vec{r}$	position vector
R	electric Reynolds number or sum of covalent radii
R_{eL}	Reynolds number based on L

$\dot{R}$	radiative energy loss per unit volume
S	orbital strength
t	scaled sheath coordinate
T	absolute temperature
u_∞	characteristic velocity
$\vec{u}$	velocity field
v_d	drift velocity
$\vec{v}$	particle velocity
V	velocity normal to stagnation electrode
V_i	ionization potential of seed atom
$\vec{V}$	$= \vec{u}/u_\infty$
V_{am}	ambipolar voltage drop
V_{sh}	sheath voltage drop
V_t	$= V_{sh} + V_{am}$
V_{BK}	cathode voltage drop at transition
V_{cath}	cathode voltage drop
V_{anode}	anode voltage drop
V_E	electric field signal
V_I	current signal
V_C	cathode drop signal
W	scaled sheath electric field
X	sheath constant
y	vertical coordinate from stagnation electrode
y_P	$= yL$
α	$= h_{e\infty}/L$

β	$= D_{io}/(\varepsilon D_{eo})$ or ionization coefficient
γ	recombination coefficient
$\vec{\gamma}_s$	non-dimensional particle flux of s
$\vec{\Gamma}_s$	particle flux of s species
$\Delta\phi$	Schottky correction
δ	$\equiv 1/\sqrt{R+\omega}$
$\delta_{b\ell}$	electric boundary layer thickness
δ_{atom}	atom diffusion boundary layer thickness
δ_{vis}	viscous boundary layer thickness
δ_{ther}	thermal boundary layer thickness
ε	$= T_{io}/T_e$, temperature ratio
ε_o	permittivity of free space
ε_K	$= n_K/n_A$, seed fraction
η	electric boundary layer coordinate
η_o	ambipolar matching position
$\eta_{o_{eff}}$	$\equiv -N_o/I$, effective ambipolar matching position
θ	degree of coverage
λ	charged-neutral mean free path or electronic thermal conductivity
μ_s	flux of particles of s species moving towards surface
ν	kinematic viscosity or vibration frequency
ν_s	particle flux of s species emitted from surface
ν_{sj}	collision frequency for momentum transfer
σ	$= n_{e\infty}/n_{a\infty}$, seed degree of ionization
σ_e	electrical conductivity
σ_f	number of adsorption sites per unit area

σ_m	substrate surface density
τ	$= D_{io}/D_{ao}$
ϕ	electrical potential
ϕ_e	surface work function
ϕ_a	atom desorption energy
ϕ_i	ion desorption energy
ϕ_f	adsorbate work function
ϕ_m	substrate work function
ϕ'	heat of sublimation
ψ	$= -e\phi/kT_e$
ω	$= (\epsilon L^2 n_{e\infty}^2 \gamma)/D_{io}$
$\dot{\Omega}$	volumetric energy loss rate from free electrons due to elastic collisions

Subscripts

a	seed atom
am	ambipolar
A	argon
$b\ell$	electric boundary layer
c	carrier gas
e	electron
f	adsorbate
i	ion
K	potassium
m	substrate
n	neutrals
o	implies value in sheath

s	species identification
sh	sheath
t	implies electrode surface tangential component
w	at electrode surface
Z	implies $E_w = 0$ and $\Gamma_{iw} = 0$
∞	implies value in bulk plasma

Superscripts

$(\;)^*$	implies $E_w = 0$
$(\bar{\;})$	average quantity
$(\vec{\;})$	vector quantity
$(\tilde{\;})$	implies term non-dimensionalized by its value in the sheath

Miscellaneous

Erf	error function
Exp	exponential function
P	incomplete gamma function
O	on the order of
∇	differential vector operator
Σ	implies summation operation

REFERENCES

1. Cool, T.A. and Zukoski, E.E., "Recombination, Ionization, and Nonequilibrium Electrical Conductivity in Seeded Plasmas," Phys. of Fluids, Vol. 9 (1966), pp. 780-796.

2. Kerrebrock, J. L., "Nonequilibrium Ionization Due to Electron Heating: Part I. Theory," AIAA Journal, Vol. 2 (1964), pp. 1072-1080.

3. Curry, B.P., "Ionization and Recombination in Alkali-Seeded Collision-Dominated Plasmas," AEDC-TR-65-260, Arnold Engineering Development Center, Arnold Air Force Station, Tenn. (February 1966).

4. Cobine, J.D., Gaseous Conductors, Dover Publications, Inc., New York (1958), p. 36.

5. McDaniel, E. W., Collision Phenomena in Ionized Gases, John Wiley and Sons, Inc., New York (1964), p. 685.

6. Langmuir, I. and Taylor, J. B., "The Evaporation of Atoms, Ions, and Electrons from Cesium Films on Tungsten," Phys. Rev., Vol. 44 (1933), pp. 423-458.

7. Gyftopoulos, E.P. and Levine, J. D., "Work Function Variation of Metals Coated by Metallic Films," J. Appl. Phys., Vol. 33 (1962), pp. 67-73.

8. Levine, J. D. and Gyftopoulos, E.P., "Adsorption Physics of Metallic Surfaces Partially Covered by Metallic Particles. I. Atom and Ion Desorption Energies," Surface Science, Vol. 1 (1964), pp. 171-193.

9. Levine, J. D. and Gyftopoulos, E.P., "Adsorption Physics of Metals Partially Covered by Metallic Particles. II. Desorption Rates of Atoms and Ions," Surface Science, Vol. 1 (1964), pp. 225-241.

10. Levine, J. D. and Gyftopoulos, E.P., "Adsorption Physics of Metals Partially Covered by Metallic Particles. Part III: Equations of State and Electron Emission S-Curves," Surface Science, Vol. 1 (1964), pp. 349-360.

11. Nottingham, W. B. and Breitwieser, R., "Theoretical Background for Thermionic Conversion Including Space-Charge Theory, Schottky Theory, and the Isothermal Diode Sheath Theory," NASA TN D-3324 (1966).

12. Bienkowski, G. and Kalnavarns, J., "The Effect of Surface Emission on Continuum Electrostatic Probe Theory," AIAA Paper 68-167 (1968).

13. Sajben, M., "Boundary Conditions for Adsorbing-Emitting Electrodes in Contact with Seeded, Dense Plasmas," accepted for publication in the AIAA Journal (1970).

14. Kerrebrock, J. L., "Segmented Electrode Losses in MHD Generators with Nonequilibrium Ionization," AIAA Journal, Vol. 4 (1966), pp. 1938-1947.

15. Oliver, D. A. and Mitchner, M., "Nonuniform Electrical Conduction in MHD Channels," AIAA Journal, Vol. 5 (1967), pp. 1424-1432.

16. Lutz, M. A., "Radiation and Its Effect on the Nonequilibrium Properties of a Seeded Plasma," AIAA Journal, Vol. 5 (1967), pp. 1416-1423.

17. Su, C. H. and Lam, S. H., "The Continuum Theory of Spherical Electrostatic Probes," Phys. of Fluids, Vol. 6 (1963), pp. 1479-1491.

18. Cohen, I. M., "Asymptotic Theory of Spherical Electrostatic Probes in a Slightly Ionized, Collision Dominated Gas," Phys. of Fluids, Vol. 6 (1963), pp. 1492-1499.

19. Lam, S. H., "A General Theory for the Flow of Weakly Ionized Gases," AIAA Journal, Vol. 2 (1964), pp. 256-263.

20. Burke, A. F. and Lam, S. H., "A General Theory of Weakly Ionized Gas Flows Including Compressibility and Electron Energy Effects," AIAA Paper 67-100 (1967).

21. Schach, W., "Umlenkung eines Kreisförmigen Flüssigkeitsstrahles an einer eben Platte senkrecht zur Strömungsrichtung," Ingenieur-Archiv., Vol. 6 (1935), pp. 51-59.

22. Leclerc, A., "Déviation d'un Jet Liquide par une Plaque Normale à son Axe," La Honille Blanche, Vol. 5 (1950), pp. 816-821.

23. Shen, Y. C., "Theoretical Analysis of Jet-Ground Plane Interaction," IAS Paper 62-144 (June 1962).

24. Schlichting, H., Boundary Layer Theory, McGraw-Hill Book Co., New York (1960), pp. 81-83.

25. Kreith, F., Principles of Heat Transfer, International Textbook Co., Scranton (1962), p. 266.

26. Bird, R. B., Stewart, W. E., and Lightfoot, E. N., Transport Phenomena, John Wiley and Sons, Inc., New York (1960), pp. 504-513.

27. Brown, S. C., Basic Data of Plasma Physics, The Technology Press of the Massachusetts Institute of Technology and John Wiley and Sons, Inc., New York (1959), p. 33.

28. Cool, T. A., "Recombination, Ionization, and Nonequilibrium Electrical Conductivity in Seeded Plasmas," Ph. D. Thesis, California Institute of Technology (1965).

29. Handbook of the Physicochemical Properties of the Elements, G. V. Samsonov, Ed. (translated from Russian), Plenum Press, New York (1968), p. 354.

30. Handbook of Chemistry and Physics, 49th Edition, R. C. Weast, Ed., The Chemical Rubber Co., Cleveland (1968), p. E-71.

31. The Collected Works of Irving Langmuir, C. G. Suits, Ed., Pergamon Press, Inc., New York (1961), Vol. 3, p. xxvi.

32. Adams, R. C. and Robinson, E., "Electrode Processes in MHD Generators," Proc. of IEEE, Vol. 56 (1968), pp. 1519-1535.

33. Nichols, L. D. and Mantenieks, M. A., "Analytical and Experimental Studies of MHD Generator Cathodes Emitting in a 'Spot' Mode," NASA TN D-5414 (1969).

34. Killian, T. J., "Thermionic Phenomena Caused by Vapors of Rubidium and Potassium," Physical Review, Vol. 27 (1926), pp. 578-587.

APPENDIX A

Electron Temperature Assumption

The purpose of this appendix is to indicate the conditions under which the electron temperature is approximately constant throughout the bulk plasma and the electric boundary layer regions. The discussion here is limited to the one-dimensional case.

First, the appropriate boundary condition at the surface for the electron energy equation (4) must be specified. The surface condition is found by the same method as used in Section 2. 4 to specify the surface number densities; that is, a control volume for a Knudsen layer is used for a conservation of energy balance where the energy fluxes are found by averaging $\frac{1}{2}m_e\vec{v}\cdot\vec{v}$ over the assumed velocity distribution function. The energy flux from the electrons emitted from the electrode surface is computed by assuming a half-Maxwellian distribution function at the surface temperature. The integrations are straightforward and the resulting macroscopic energy flux at the surface is:

$$q_{ew} = \nu_e(2kT_w - 2kT_{e0}) + \Gamma_{ew}V_i + \Gamma_{ew}\frac{9}{4}kT_{e0} \quad . \qquad \text{(A. 1)}$$

Relating equation (A. 1) to the energy flux in terms of macroscopic gradients gives an expression for dT_e/dy at the surface:

$$\left.\frac{dT_e}{dy}\right|_w = -\frac{L}{\lambda}\left[\nu_e(2kT_w - 2kT_{e0}) - \frac{\Gamma_{ew}}{8}\,2kT_{e0}\right] \quad . \qquad \text{(A. 2)}$$

By transforming the energy equation (4) to the sheath coordinates given in Section 2. 5, the temperature profile in the sheath is found to be linear to $O\left((\alpha^2/\delta^2 I)^{1/3}\right)$ and hence the temperature change through the sheath region is on the order of $dT_e/dy|_w (\alpha^2 \delta / I)^{1/3} L$. Unless the electronic thermal conductivity is very small, the sheath temperature change is negligibly small. The transport of energy away from the sheath vicinity is studied by transforming the energy equation (4) to electric boundary layer coordinates and by finding an energy boundary condition for the plasma side of the sheath region by considering an energy balance for a control volume about the sheath region.

The volumetric energy production terms in the sheath control volume are negligible (due to the sheath thinness) with the exception of the Joule heating term (Ej_e); since the fluxes are constant through the sheath (see Section 2. 5) this volumetric term is transformed to a surface term (by a form of the divergence theorem) and the result of the energy balance is:

$$\left.\frac{dT_e}{dy}\right|_{sh} = \frac{-L}{\lambda}\left[\nu_e(2kT_w - 2kT_{e0}) - \frac{\Gamma_{ew}}{8}\, 2kT_{e0} + \Gamma_{ew} e V_{sh}\right] . \qquad (A.\ 3)$$

With the aid of the following non-dimensional variables:

$$\tilde{\lambda} = \frac{\lambda}{kD_{e0} n_{e\infty}} \qquad \tilde{V}_i = \frac{V_i}{kT_{e0}} \qquad \tilde{T}_e = \frac{T_e}{T_{e0}}$$

$$\tilde{\dot{\Omega}} = \dot{\Omega}\, \frac{L^2}{kT_{e0} D_{e0} n_{e\infty}} \qquad \tilde{\dot{R}} = \dot{R}\, \frac{L^2}{kT_{e0} D_{e0} n_{e\infty}} \qquad (A.\ 4)$$

the electron energy equation (4), in terms of the boundary layer coordinate (η), becomes:

$$-\tilde{\lambda}\frac{d^2\tilde{T}_e}{d\eta^2} = -(\tilde{I}+\frac{5}{2}\tilde{T}_e)\delta^2\omega N\frac{\gamma}{\gamma_\infty}\left(\frac{n^2_{saha}}{n^2_{e\infty}} - N^2\right) + \tilde{T}_e\beta R\delta V\frac{dN}{d\eta} - \delta^2(\tilde{\dot{\Omega}} - \tilde{\dot{R}})$$

$$+\delta\gamma_e\frac{d\psi}{d\eta} - \frac{d\tilde{T}_e}{d\eta}\left[\frac{3}{2}\beta R\delta VN + \frac{5}{2}\delta\gamma_e - \frac{d\tilde{\lambda}}{d\eta}\right] \qquad \text{(A. 5)}$$

where $d\Gamma_e/dy$ has been eliminated by the substitution of equation (2). Since ω and R are $O(\delta^{-2})$ and γ_e is $O(\delta^{-1})$, the majority of the terms in equation (A. 5) are of the same order, so that the electron temperature will vary over a region on the order of δL in thickness.

The energy added to the electrons in the sheath region is then conducted away from the sheath region to the ambipolar diffusion region, where it is removed by the processes of convection, radiation, elastic collisions with the heavies, and by ionization. The temperature increase in the sheath region depends on how fast the energy in this region is conducted away. Considering the case of a cathode nearing saturation so that $V_{sh} > kT_{e0}$ or kT_w, equation (A. 3) becomes:

$$\left.\frac{dT_e}{dy}\right|_{sh} \approx -\frac{L}{\lambda}(\Gamma_{ew}\, e\, V_{sh})$$

and $dT_e/dy|_{sh}$ is roughly $-(\Delta T_e)/\delta$ so that the temperature increase in the sheath is

$$\Delta T_e \approx \frac{\delta L}{\lambda}\Gamma_{ew}\, e\, V_{sh} \; . \qquad \text{(A. 6)}$$

The sheath voltage drop which causes a 10 percent increase in the sheath electron temperature is displayed as a function of current density in Figure A. 1. Note that for V_{sh} less than about 2 volts, the constant electron temperature assumption is justified here. However, for high sheath drops, the rise in electron temperature has an important effect on the thermionic limiting current for the case $\omega > R$; the production limited case is sensitive to electron temperature, so that a rise in T_e increases the ionization, which, as shown in Section 2.9, considerably augments the thermionic limit.

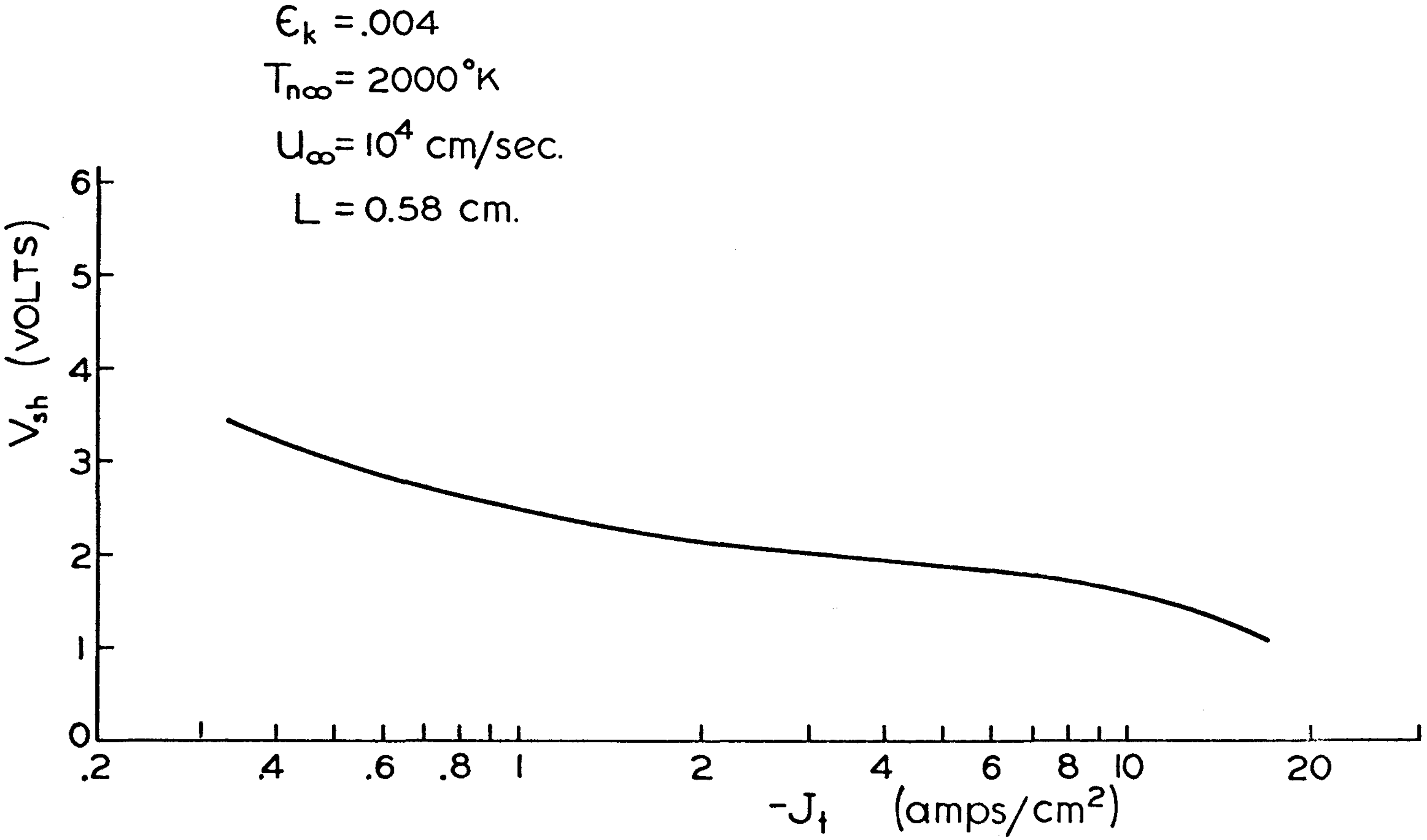

FIG. A.1 SHEATH VOLTAGE DROP WHICH INCREASES SHEATH ELECTRON TEMPERATURE BY 10 PER CENT

APPENDIX B

Approximate Sheath Drop Calculation

For sheath voltage drops greater than about 0.5 volts, the computer integration of the sheath equation (52) would not converge to the ambipolar limit ($W = X/t$) even though the initial value for W_w had been found by iteration to eight digits. For large sheath drops, the non-dimensionalized electric field at the wall (W_w) is correspondingly large, and since the solution curve for W must start from the boundary parabola given by equation (57), t_w is negative for the values of the surface parameter A, see equation (56), encountered here. The lack of convergence is due to the severe integration instability of equation (52) which prevents a numerical integration from the negative value of t_w to the ambipolar limit in the positive t half-plane.

Even though the solution curve for W does not converge, W_w is known to our desired degree of accuracy, and all the unknowns of the problem except the sheath drop can be found. The sheath drop is estimated by the following intuitive derivation, which is justified by comparison with known solutions.

On the W-t plane in Figure B. 1, the ambipolar limit ($W = X/t$), the boundary parabola ($W_w^2 = -2\{1+\epsilon\} t_w + 2A$), the exact computer solution, and the approximate solution discussed here are presented for conditions that correspond to a point near the saturation region on the current-voltage characteristic. In addition, a curve defined by the algebraic terms of equation (52)

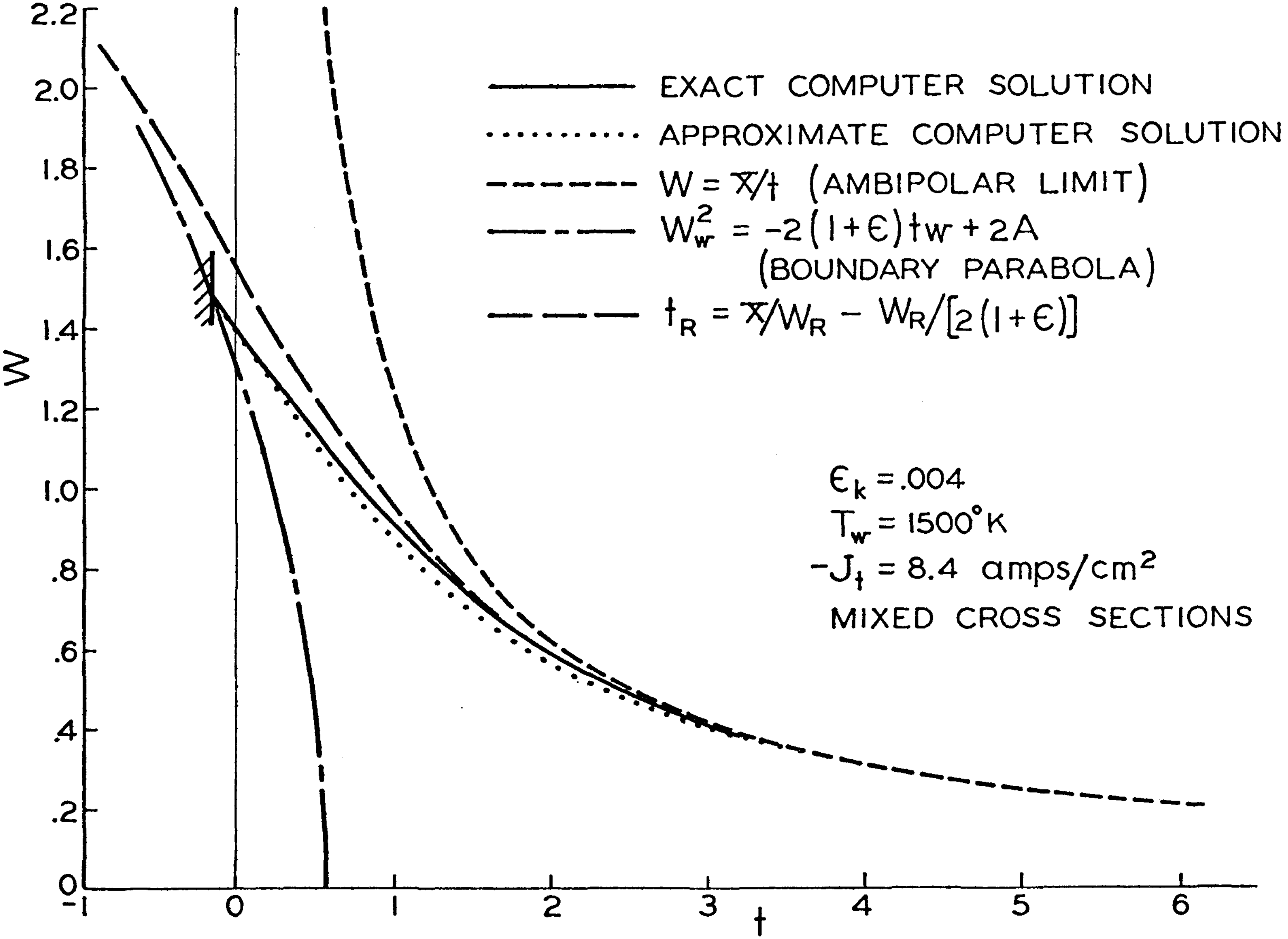

FIG. B.1 W-t PLANE WITH SHEATH SOLUTION

$$t_R = \frac{X}{W_R} - \frac{W_R^2}{2(1+\varepsilon)} \qquad \text{(B. 1)}$$

is shown. For dW/dt on the order of $dW/dt|_{t=t_w} = B$, equation (52) requires that for $W >> W_R$, $d^2W/dt^2 \sim W^3/2\varepsilon$, which prevents the convergence of the $W(t)$ solution curve to the ambipolar limit. For $W << W_R$, $d^2W/dt^2 \sim -|\frac{W^3}{2\varepsilon}|$ and convergence is impossible. Therefore, we expect the exact solution curve to lie near the $W_R(t_R)$ curve, and from Figure B. 1 this proximity is justified. Since $d^2W_R/dt_R^2 \sim (1+\varepsilon)^2/W^3$, the second derivative is small over much of the solution curve for saturation cases. The approximate solution for W is found by setting $d^2W/dt^2 = 0$ and estimating dW/dt by dW_R/dt_R, which gives

$$t_{ap} = \frac{X}{W_{ap}} - \frac{W_{ap}^2}{2(1+\varepsilon)} - \frac{(1-\varepsilon)W_{ap}^2}{W_{ap}^3 + X(1+\varepsilon)} \quad . \qquad \text{(B. 2)}$$

The approximate method of solution is to numerically integrate the full sheath equation (52) from the boundary parabola to the approximate solution curve given by equation (B. 2). The sheath voltage drop corresponding to $t_{ap}(W_{ap})$ is easily found by using equation (62) and equation (B. 2), which results in:

$$F_{sh} \approx X - tW + X\,\ell n\,\frac{W}{X} - \frac{W^3}{6(1+\varepsilon)} - \left(\frac{1-\varepsilon}{3}\right)\ell n\left|\frac{W^3+X(1+\varepsilon)}{W_z^3+X(1+\varepsilon)}\right| \qquad t < 0$$

where

$$W_Z = [2(1+\varepsilon)X]^{1/3}\left[1 - \frac{2(1-\varepsilon)}{9X}\right] \quad .$$

Note the good agreement of the approximate solution with the exact solution in Figure B. 1. The difference in F_{sh} calculated by the two methods is less than 6 per cent.

APPENDIX C

Listing of Computer Program

This appendix contains a listing of the two main computer programs (written in Fortran IV language) used for the numerical work of Section 2.9. The computation scheme (see Figure 7) was broken into two parts, indicated by the vertical dashed line on Figure 7. The first program listed (named AMBI) computed the left hand side of Figure 7, while the second program listed (called SHTH) calculated the right hand side. The flow chart channels crossing the dashed line on Figure 7 were carried out manually by using data cards. The double program method was just for economical reasons.

The subroutine called DEQ, which appears in both programs, is a standard integration subroutine which solves a system of ordinary differential equations (in the case here, for three dependent variables) by integrating from a given point starting with two initial values for each dependent variable.

The programs were run on the California Institute of Technology's IBM 75/50.

A translation list of the computer names of physical variables and parameters is given in Table C. 1.

TABLE C. 1

Translation of Computer Names

Computer Name	Symbol	Units	Computer Name	Symbol	Units
A	A		EPHY	E_w	v/cm
AK	k	eV/^oK	EPY	E	v/cm
ALFA	α		F	F	
B	B		FIA	ϕ_a	eV
BD	β		FIE	ϕ_e^*	eV
CE	$\bar{C}_e$	cm/sec	FIL	ϕ_f	eV
CHAR	e	coulombs	FIW	ϕ_e	eV
CK	$\bar{C}_a$	cm/sec	FIWI	ϕ_i	eV
DA	D_a	cm^2/sec	FLXE	Γ_e	#/cm^2-sec
DBYLE	$h_{e\infty}$	cm	FLXI	Γ_i	#/cm^2-sec
DE	D_e	cm^2/sec	FM	a	
DEL	δ		G	G	
DEO	D_{eo}	cm^2/sec	GB	G_w	
DIO	D_{i0}	cm^2/sec	HB	K_w	
EP	ϵ		JEW	J_{ew}	amps/cm^2

TABLE C. 1 (continued)

Computer Name	Symbol	Units	Computer Name	Symbol	Units
JT	J_t	amps/cm^2	RCMB	γ	cm^6/sec
LTH	L	cm	SAUG	A_E	
MET	ϕ_m	eV	SEED	ϵ_K	
NAW	N_{aw}		SIT	σ_f	10^{14}/cm^2
NAX	N_a		SHOT	$\Delta\phi$	eV
NENF	$n_{e\infty}$	#/cm^3	SLPI	I	
NEW	N_{ew}		SLPZ	I_o	
NIW	N_{iw}		T	t	
NK	n_a	#/cm^3	TB	t_w	
NUA	ν_a	#/cm^2-sec	TE	T_e	$^\circ$K
NUE	ν_e	#/cm^2-sec	TGAS	$T_{n\infty}$	$^\circ$K
NUI	ν_i	#/cm^2-sec	TIX	T_n	$^\circ$K
OMEG	ω		TSUR	T_w	$^\circ$K
QNC	K_1		U	u_∞	cm/sec
R	R		VIS	ν	cm^2/sec

TABLE C. 1 (continued)

Computer Name	Symbol	Units	Computer Name	Symbol	Units
VOLT	V_{sh}	volts	X	η	
VOLTA	V_{am}	volts	X	X	
W(1)	W		Y(1)	N	
W(2)	dW/dt		Y(2)	$dN/d\eta$	
W(3)	$-\psi$		Y(3)	ψ	
WB	W_w		YP	yL	cm
			Z	θ	

```
//AMBI   JOB   (21210,JQK,JPC),KOESTER,MSGLEVEL=1
//AMBI   EXEC  FORTGCLG,TIME.FORT=(,5),TIME.LKED=(,3),
//             REGION.GO=100K,TIME.GO=2
//FORT.SYSIN DD *
C  AMBIPOLAR DIFFUSION REGION
      DIMENSION Y(3), YDOT(3)
      REAL LTH,NKO,NK,NENF,NL,KL,JEW,JT,JET,NUA,NUX,NUE,MET,NAW,NAX,KERF
C   FUNCTIONS  DEFINED
      KERF(X) = 1. - EXP(-1.1198*X - .9*X**2)
      CK(X) = 2.3265E3*SQRT(X)
      DI(X)= (3.4808*X**2)/(CK(X)*(48.1 + 133. *SEED*(1. - NENF/NKO)))
      TI(X) = TGAS + (TSUR - TGAS)*EXP(-AUL*X*(1.536 + .358*AUL*X))
      VEL(X) = -2.*AVL*(AUL*X - .569 + .569*EXP(-AUL*X*(1.536 + .358*AUL
     1*X)))
      SPZ(X) = 1.239E4*TE**1.5/SQRT(X)
      DES(X) = 8.2417E10*TE**2.5/(ALOG(SPZ(X))*X)
      DEC(X) = 1.755E5*TE*X/(CE*(.7 + 400.*SEED*(1. - NENF/NKO)))
      DEM(X,Y) = DES(Y)*DEC(X)/(DES(Y) + DEC(X))
   30 READ(5, 200) TSUR, TE,JT ,NL
   31 TGAS = 2000.
       U = 1.E4
      FM = .4
      LTH = .58
      SEED = .004
C COMPUTE PLASMA PROPERTIES
      CHAR = 1.6021E-19
      EP = TSUR/TE
      NKO = (7.3404E21*SEED)/TGAS
       B = 2.4147E15*(TE**1.5)*EXP(-5.0357E4/TE)
      NENF = .5*(SQRT(B**2 + 4.*B*NKO) - B)
      AK = 8.6164E-5
      DBYLF = 6.9009*SQRT(TE/NENF)
      ALFA = DBYLE/ LTH
      CE = 6.2124E5*SQRT(TE)
      NK = NKO - NENF
      VIS = 3.46*((TGAS + TSUR)/4000.)**1.6495
```

```
      DIO = DI(TSUR)
      AUL = SQRT(FM*U*LTH/VIS)
      AVL = SQRT(FM*VIS/(U*LTH))
      RCMB = 1.256E-25 + .2519E-20*EXP(-2.98E-3*TE)
      R = EP*U*LTH/DIO
      OMEG = EP*LTH**2*NENF**2*RCMB/DIO
      DEL = 1./SQRT(R + OMEG)
      IF(NL*NENF .LT. 1.E10 )  DEO = DEC(TSUR)
      IF(NL*NENF .GE. 1.E10)  DEO = DEM(TSUR,NL*NENF)
      BD = DIO/(EP*DEO)
      DA = .629*((TGAS+ TSUR)/4000.)**1.72
      WRITE(6,305)TSUR,TE,NENF,ALFA,DIO,DEO,OMEG,R,DEL
      WRITE(6,309)
      CONV = .005
      ERROR = 1.E-5
      CB = .5
      MAX = 40
      UP = 1.
      N = 1
      ITER = 0
      SLPI = 1.
      SLPIL = 0.
C  START ITERATION FOR  I SLOPE
  105 IF(ITER .GT. MAX)  GO TO 30

C INITIAL CONDITIONS
      X = 0.
      Y(1) = NL
      Y(2) = SLPI
      ITER = ITER + 1
      Q = (1.- EP*BD -DEL*JT*LTH/(SLPI*DEO*NENF*CHAR))/(1. +BD)
      FLXI = -DIO*NENF*SLPI*(Q + EP)/(EP*LTH*DEL)
      SCL = DEL*SQRT(FM*U*LTH)*(.4287/(DA*SQRT(VIS)))**(1./3.)
      NAW = 1. - .89298*DEL*LTH*FLXI/(DA*SCL*NKO)
       CT =  .02
  109 CALL DEQ(K,2,X,Y,YDOT,CT,ERROR)
```

```
110 GO TO (112,120,120,150),K
112 TIX = TI(X*DEL)
    NAX = NAW + (1.- NAW)*KERF(SCL*X)
    IF(Y(1)*NENF .LT. 1.E10) DE = DEC(TIX)
    IF(Y(1)*NENF .GE. 1.E10) DE = DEM(TIX,Y(1)*NENF)
    YDOT(1) = Y(2)
    YDOT(2) = ((DE*DIO*TIX+BD*DEO*TSUR*DI(TIX))/(DE*DI(TIX)*(TSUR+EP*T
   1IX)))*(R*DEL*VEL(X*DEL)*Y(2)-DEL**2*OMEG*(Y(1)*NAX -Y(1)**3))
    CALL DEQ2(&110, &127)
120 IF(X .GT. 15.) GO TO 150
122 IF(Y(1) .GT. 1.) GO TO 170
    IF(Y(2) .LT. 0.) GO TO 180
121 IF(ABS(Y(1)-1.) .LT. CONV .AND. ABS(Y(2)) .LT. CONV) GO TO 190
125 CALL DEQ1 (&110)
127 GO TO 121
170 N= 2
    WRITE(6,310) ITER,SLPI,X,Y(1),Y(2)
    SLPIH = SLPI
    SLPI = .5*(SLPIH-SLPIL) + SLPIL
    GO TO 105
180 SLPIL = SLPI
    WRITE(6,310) ITER,SLPI,X,Y(1),Y(2)
    GO TO (181, 183), N
181 SLPI = SLPIL + CB*UP
    UP = 2.*UP
    GO TO 105
183 SLPI = .5*(SLPIH-SLPIL) + SLPIL
    GO TO 105
150 WRITE(6, 320) ITER,SLPI,X,Y,YDOT
    GO TO 30
190 WRITE(6, 330) ITER,NL,SLPI,X,Y(1),Y(2) ,NAW
    WRITE(6,339)
    RAI = (ALFA*SLPI/DEL)**(2./3.)
    CAC = X
    XAZ = (ALFA**2/(SLPI*DEL**2))**(1./3.)
    KL = NL/RAI
```

```
      JEW = -(JT + DIO*NENF*CHAR*(1.+EP)*SLPI/(LTH*DEL*EP))/(1.+BD)
C INITIAL CONDITIONS
      X = 0.
      Y(1) = NL
      Y(2) = SLPI
      Y(3) = 0.
      Q = (1.- EP*BD -DEL*JT*LTH/(SLPI*DEO*NENF*CHAR))/(1. +BD)
      FLXI = -DIO*NENF*SLPI*(Q + EP)/(EP*LTH*DEL)
      SCL = DEL*SQRT(FM*U*LTH)*(.4287/(DA*SQRT(VIS)))**(1./3.)
      NAW = 1. - .89298*DEL*LTH*FLXI/(DA*SCL*NKO)
  409 CALL DEQ(K,3,X,Y,YDOT,CT,ERROR)
  410 GO TO (412,420,420,150),K
  412 TIX = TI(X*DEL)
      NAX = NAW + (1.- NAW)*KERF(SCL*X)

      IF(Y(1)*NENF .LT. 1.E10) DE = DEC(TIX)
      IF(Y(1)*NENF .GE. 1.E10) DE = DEM(TIX,Y(1)*NENF)
      YDOT(1) = Y(2)
      YDOT(2) = ((DE*DIO*TIX+BD*DEO*TSUR*DI(TIX))/(DE*DI(TIX)*(TSUR+EP*T
     1IX)))*(R*DEL*VEL(X*DEL)*Y(2)-DEL**2*OMEG*(Y(1)*NAX -Y(1)**3))
      IF(NL .LE. RAI .AND. X .LT.XAZ) YDOT(3) = 0.
      IF(NL .GT. RAI .OR. X .GE. XAZ) YDOT(3) = (DEL*LTH*JT/(CHAR*NENF)
     1- (DE-DI(TIX))*Y(2))/(Y(1)*(DE + DI(TIX)*TE/TIX))
      CALL DEQ2(&410, &427)
  420 YP = X*DEL*LTH
      VA = -Y(3)*AK*TE
      EPY = AK*TE*YDOT(3)/(DEL*LTH)
      WRITE(6,340) X,Y(1),Y(2),Y(3),YP,VA, EPY, DE,NAX
  422 IF(X .GE. CAC) GO TO 430
  425 CALL DEQ1 (&410)
  427 GO TO 422
  430 VOLTA = -(AK*TE)*(Y(3)-DEL*CAC*JT*LTH/(NENF*CHAR*(DEM(TGAS,NENF) +
     1DI(TGAS)*TE/TGAS)))
      WRITE(6,350) KL,XAZ,JEW,JT,VOLTA
      GO TO 30
  200 FORMAT(4F10.0)
```

```
  305 FORMAT(48HOPROPERTIES TSUR TE NENF ALFA DIO DEO OMEG R DEL//1X,1P9
     1E13.5///)
  309 FORMAT(38HOITERATION TRIALS ITER SLPI Y N NPRIME///)
  310 FORMAT(1X,I4,1P4E14.6/)
  320 FORMAT(11H0150 RETURN//1X, I4, 1P6E14.6)
  330 FORMAT(47HOSOLUTION CONVERGES ITER NL SLPI Y N NPRIME NAW//1X,I4,1
     1P6E15.7////)
  339 FORMAT(47HOSOLUTION CURVES Y N NPRIME PSI YP VA EPY DE NA///)
  340 FORMAT(1X,1P9E13.5/)
  350 FORMAT(56HOAMBIPOLAR DIFFUSION CHARACTERISTICS KL XAZ JEW JT VOLTA
     1//1X,1P5E14.6////)
      END
```

```
//SHTH   JOB   (21210,JQK,JPC),KOESTER,MSGLEVEL=1
//SHTH   EXEC  FORTGCLG,TIME.FORT=(,9),TIME.LKED=(,5),
//             REGION.GO=100K,TIME.GO=2
//FORT.SYSIN DD *
C  SURFACE-SHEATH INTERACTION FOR TUNGSTEN IN K-SEEDED PLASMA
      REAL LTH,NKO,NK,NENF,NUA,NUX,NUI,NUE,NIW,NEW,JT, NL,NLP,MET
      DIMENSION W(3), WDOT(3), FBC(130), XTV(130)
C   FUNCTIONS  DEFINED
      FNC(X) = 1.1284*(-X)/SQRT(ALOG(-X/7.0898) -1.5*(1.- 293./X)*ALOG(A
     1LOG(-X/7.0898)))
```

```
      SPZ(X) = 1.239E4*TE**1.5/SQRT(X)
      DES(X) = 8.2417E10*TE**2.5/(ALOG(SPZ(X))*X)
      DEC(X) = 1.755E5*TE*X/(CE*(.7 + 400.*SEED*(1. - NENF/NKO)))
      DEM(X,Y) = DES(Y)*DEC(X)/(DES(Y) + DEC(X))
      DATA FBC / 0.0,.3761,.3891,.403,.4179,.434,.4513,.4701,.4906,.5129
     1,.5372,.5641,.5936,.6264,.663,.70397,.7501,.8024,.8619,.9302,1.009
     2,1.121,1.142,1.163,1.185,1.208,1.232,1.256,1.281,1.307,1.334,1.362
     3,1.391,1.421,1.452,1.485,1.518,1.553,1.588,1.626,1.664,1.704,1.746
     4,1.789,1.834,1.881,1.93,1.98,2.033,2.088,2.145,2.204,2.266,2.331,2
     5.398,2.469,2.542,2.618,2.698,2.782,2.87,2.96,3.056,3.155,3.26,3.36
     69,3.484,3.604,3.73,3.862,4.0,4.145,4.298,4.458,4.626,4.803,4.99,5.
     7185,5.392,5.609,5.837,6.078,6.332,6.601,6.883,7.182,7.498,7.831,8.
     8184,8.556,8.951,9.369,9.811,10.28,10.777,11.304,11.864,12.458,13.0
     989,13.759,14.472,15.231,16.038,16.898,17.814,18.791,19.832,20.944,
     122.13,23.398,24.752,26.2,27.75,29.409,31.186,33.09,35.131,37.32,39
     2.67,42.195,44.907,61.888,86.635,123.22,178.12,261.71,390.98,593.99
     3,917.88 /
      DATA XTV / 1.0,.9999995,.9999989,.9999978,.9999959,.9999923,.99998
     157,.9999739,.9999533,.9999176,.999857,.9997557,.9995886,.9993175,
     2.9988838,.9981995,.9971339,.9954953,.9930052,.9892629,.9836951,.97
     354887,.9734368,.9712237,.9688375,.9662653,.9634935,.9605073,.95729
     412,.9538282,.9501005,.9460886,.941772,.937129,.932135,.926766,.920
     5993,.914789,.908122,.900958,.89326,.8845,.87612,.8666,.85636,.8453
     67,.83358,.82093,.80735,.79278,.77714,.76036,.74237,.72306,.70235,.
     768013,.6563,.63074,.60331,.5739,.54235,.50851,.47221,.43327,.39149
     8,.34667,.29859,.24699,.19163,.13221,.068444,0.0,-.073473,-.15235,
     9-.23705,-.32801,-.42569,-.53063,-.64337,-.7645,-.8947,-1.0346,-1.1
     1851,-1.3469,-1.5209,-1.7081,-1.9095,-2.1263,-2.3596,-2.6109,-2.881
     25,-3.173,-3.4871,-3.8257,-4.1907,-4.5843,-5.009,-5.4672,-5.9618,
     3-6.4957,-7.0724,-7.6955,-8.3688,-9.0968,-9.884,-10.735,-11.657,-12
     4.655,-13.735,-14.906,-16.174,-17.549,-19.04,-20.658,-22.414,-24.32
     51,-26.392,-28.643,-31.09,-33.751,-36.646,-39.797,-60.331,-92.134,-
     6141.96,-220.99,-347.91,-554.39,-894.9,-1464.2 /
      TGAS = 2000.
      U = 1.E4
```

```
      LTH = .58
      SEED = .004
      FM = .4
      Z = .25
      GO TO 30
   28 WRITE(6,370)  FLXI
   29 WRITE(6,360) ARG
   30 READ(5,200) TSUR,TE,JT,SLPZ,QNC
      WB = 5.
C COMPUTE PLASMA PROPERTIES
      CHAR = 1.6021E-19
      AK = 8.6164E-5
      EP = TSUR/TE
      CK = 2.3265E3*SQRT(TSUR)
      CE = 6.2124E5*SQRT(TE)
      NKO = (7.3404E21*SEED)/TGAS

       C = 2.4147E15*(TE**1.5)*EXP(-5.0357E4/TE)
      NENF = .5*(SQRT(C**2 + 4.*C*NKO) - C)
      DIO= (3.4808*TSUR**2)/(CK*(48.1 + 133. *SEED*(1.-NENF/NKO)))
      DBYLE = 6.9009*SQRT(TE/NENF)
      ALFA = DBYLE/ LTH
      NK = (NKO - NENF)*TGAS/TSUR
      RCMB = 1.256E-25 + .2519E-20*EXP(-2.98E-3*TE)
      R = EP*U*LTH/DIO
      OMEG = EP*LTH**2*NENF**2*RCMB/DIO
      DEL = 1./SQRT(R + OMEG)
      DA = .629*((TGAS+ TSUR)/4000.)**1.72
      DEO = DEC(TSUR)
      VIS = 3.46*((TGAS + TSUR)/4000.)**1.6495
      WRITE(6,300) TE,TSUR,NENF,DIO,DEO,ALFA,DEL,EP
      SLPI = SLPZ
      NL = .1
      A = 0.
      CONV = .005
      ERROR = 1.E-5
```

```
      CB = .5
      MAX = 40
      L1 = 1
      UP = 1.
      DWN = 1.
      M = 1
      N = 1
      N2 = 1
      ITER = 0
  105 NLP = NL
      TB = (2.*A-WB**2)/(2.*(1.+EP))
      IF( TB .LE. 0.) NL = 0.
      IF(TB .GT. 0.) NL = TB*(ALFA*SLPI/DEL)**(2./3.)
      IF(NLP .EQ. 0.) GO TO 100
      IF(NL .GE. 1.) GO TO 400
      IF(NL*NENF .LT. 1.E10 )  DEO = DEC(TSUR)
      IF(NL*NENF .GE. 1.E10)  DEO = DEM(TSUR,NL*NENF)
      BD = DIO/(EP*DEO)
      SLPI = SLPZ - (SLPZ+ QNC)*NL + QNC*NL**2
      RAI = (ALFA*SLPI/DEL)**(2./3.)
      X = (1.- EP*BD -DEL*JT*LTH/(SLPI*DEO*NENF*CHAR))/(1. +BD)
      NTIME = 0
      FLXI = -DIO*NENF*SLPI*(X + EP)/(EP*LTH*DEL)
      FLXE = DEO*NENF*SLPI*(X - 1.)/(LTH*DEL)
      NUX = .25*NK*CK - FLXI*(.5+.296*CK*VIS**(1./6.)*SQRT(LTH/(FM*U))/
     1DA**(2./3.))
      IF( NUX .LT. 0.) GO TO 30
      MZ = 1
      NZ = 1
   35 NTIME = NTIME + 1
      IF( NTIME .GT. 40) GO TO 60
      IF( Z .LT. 0.)  Z = 0.
C COMPUTE SURFACE PROPERTIES
      MET = 4.62
      FIL = 2.22
      SIT = 4.8
```

```
      G = (1. + 2.*Z)*((1. - Z)**2)
      FIE = FIL + (MET- FIL)*G*(1. - .625*SQRT(1.- 1.1341/SIT)*SIT*Z/(1.
     1 + .0738*SIT*Z*SQRT(SIT*Z)))
      CC = .10384*(MET - FIL)*G
      FIA = CC*(FIE + .003934*CC) + 1.8829*SQRT(1. - CC**2)
      H = (Z/(SQRT(1. - Z)*(1. - SQRT(Z))))*EXP(.5*(SQRT(Z)/(1. - SQRT(Z
     1)) + Z/(1. - Z)))
      NUA = .2185E27*SIT*EXP(-1.1606E4*FIA/TSUR)*H*(SQRT(FIA))/SQRT(1.-
     11.1341/SIT)
      IF(ABS(1. - NUA/NUX) .LT. .0005)  GO TO 60
      IF( NUA .LT. NUX)  GO TO 40
      IF( NUA .GT. NUX)  GO TO 50
   40 NZ = 2
      ZL = Z
      GO TO (41, 43), MZ
   41 Z = Z + .05
      GO TO 35
   43 Z = ZL + .5*(ZH - ZL)
      GO TO 35
   50 MZ = 2
      ZH = Z
      GO TO (51, 53), NZ
   51 Z = Z - .05
      GO TO 35
   53 Z = ZL + .5*(ZH - ZL)
      GO TO 35
   60 WRITE(6, 385) NTIME, X, Z, NUA, NUX
      WRITE(6, 320)
C  START ITERATION OF E-FIELD AT WALL
C COMPUTE SCHOTTKY EFFECT
  100 EPHY = -(AK*TE*WB/LTH)*(SLPI/(DEL*ALFA**2))**(1./3.)
      SHOT = 0.
      IF( WB .LT. 0.)  SHOT = 3.7972E-4*SQRT(ABS(EPHY))
      FIWI = FIE - SHOT
      SHOT = 0.
```

```
      IF( WB .GT. 0.)  SHOT = 3.7972E-4*SQRT(ABS(EPHY))
      FIW = FIE - SHOT
C COMPUTE SURFACE EMISSION
      NUI = .5*NUA*EXP((FIWI- 4.339)/(AK*TSUR))
      NUE = 7.5005E20*TSUR**2*EXP(-FIW/(AK*TSUR))
C  COMPUTE BOUNDARY CONDITIONS
      ARG = FLXI/NUI
   80 IF(ARG .GT. 1.) GO TO  28
      I = 1
   82 IF( ARG .LE. XTV(I) .AND. ARG .GT. XTV( I +1)) GO TO 84
      I = I + 1
      IF (I .GT. 130) GO TO 86
      GO TO 82
   86 VAL = FNC(ARG)
      GO TO 88
   84 VAL = FBC(I) + (ARG- XTV(I))*(FBC(I +1)- FBC(I))/(XTV(I +1)- XTV(I
     1))
   88 NIW = NUI*VAL/(CK*NENF)
      ARG = FLXE/NUE
   90 IF(ARG .GT. 1.) ARG = 1.
      I = 1
   92 IF( ARG .LE. XTV(I) .AND. ARG .GT. XTV( I +1)) GO TO 94
      I = I + 1
      IF (I .GT. 130) GO TO 96
      GO TO 92
   96 VAL = FNC(ARG)
      GO TO 98
   94 VAL = FBC(I) + (ARG- XTV(I))*(FBC(I +1)- FBC(I))/(XTV(I +1)- XTV(I
     1))
   98 NEW =  NUE*VAL/(CE*NENF)
      HB = NIW/RAI
      GB = NEW/RAI

      A = GB + EP*HB
      B = GB - HB
      GO TO (108, 107), N2
```

```
  107 WRITE(6,305) ITER, WB, TB, A, B, T, W(1), W(2), W(3)
      IF(WB .EQ. WBO)  L1 = 2
  108 N2 = 2
      WBO = WB
      ITER = ITER + 1
      IF(ITER .GT. MAX)  GO TO 30
      TB = (2.*A-WB**2)/(2.*(1.+EP))
C INITIAL CONDITIONS
      T = TB
      W(1) = WB
      W(2) = B
      W(3) = 0.
      TC = TB + .1
      CT = .005
  109 CALL DEQ(K,3,T,W,WDOT,CT,ERROR)
  110 GO TO (112,120,120,150),K
  112 WDOT(1) = W(2)
      WDOT(2) = (EP-1.)*W(1)*W(2)/EP+(.5*W(1)**3)/EP+(1.+EP)*W(1)*T/EP-(
     11.+EP)*X/EP
      WDOT(3) = W(1)
      CALL DEQ2(&110, &127)
  120 IF( T .LT. TC)  GO TO 119
      IF ( T .GT.  TB+10.)  GO TO 150
      CT = .05
      IF(L1 .EQ. 2)  CT = .005
      TC = TC + 10.
      GO TO 109
  119 GO TO (121, 123), L1
  121 IF(W(2) .GT. ABS(B) + 5.)  GO TO 170
      IF( W(2) .LT.  -ABS(B) - 5.)  GO TO 180
  122 IF (T .LE. 0.) GO TO 123
      IF(ABS(W(1)-X/T) .LT. CONV .AND. ABS(W(2)+X/T**2) .LT. CONV)
     1GO TO 190
  123 GO TO (125, 124), L1
  124 TR = X/W(1)-W(1)**2/(2.*(1.+EP))-(1.-EP)*W(1)**2/(W(1)**3+X*(1.+EP
     1))
```

```
      IF(ABS(T-TR) .LE. .05   .OR.  W(2)*B .LE. 0. .OR. ABS(W(2)) .GT.
     1  ABS(B) )  GO TO 195
  125 CALL DEQ1 (&110)
  127 GO TO 119
  170 N= 2
      WBH = WB
      GO TO (171, 173), M
  171 WB = WBH-CB*DWN
      DWN = 2.*DWN
      GO TO 105
  173 WB = .5*(WBH-WBL) + WBL
      GO TO 105
  180 M= 2
      WBL = WB
      GO TO (181, 183), N
  181 WB = WBL + CB*UP
      UP = 2.*UP
      GO TO 105
  183 WB = .5*(WBH - WBL) + WBL
      GO TO 105
  150 WRITE(6, 307) ITER, WB, TB, A, B, T, W, WDOT
      GO TO 30
  190 IF( TB .LE. 1. ) F = W(3) -X*ALOG(T)
      IF (TB .GT. 1.) F = W(3) -X*ALOG(T/TB)
      WRITE(6, 310) ITER, WB, TB, A, B, T, W(1), W(2), W(3), F
      GO TO 199
  195 IF(TB .GT. 1.)  GO TO 194
      IF(T) 197,196,196
  194 F = W(3) - T*W(1) + X*T - W(1)**3/(6.*(1.+ EP))+ X*ALOG(ABS(W(1)*T
     1B/X))
      GO TO 198
  196 F = W(3) - T*W(1)+X -W(1)**3/(6.*(1.+EP))+ X*ALOG(ABS(W(1)/X))
      GO TO 198
  197 WO = (2.*(1.+EP)*X)**(1./3.)
      WZ = WO*(1. - 2.*(1.-EP)/(9.*X))
```

```
      F = W(3) - T*W(1)+X -W(1)**3/(6.*(1.+EP))+ X*ALOG(ABS(W(1)/X)) -
     1((1. -EP)/3.)*ALOG(ABS((W(1)**3+X*(1.+EP))/(WZ**3+X*(1.+EP))))
  198 WRITE(6, 315) ITER, WB, TB, A, B, T, W(1), W(2), W(3), TR, F
  199 VOLT = AK*TE*F
      SAUG = 1.
      IF( WB .GT. 0.)  SAUG = EXP(SHOT/(AK*TSUR))
      WRITE(6, 390) HB, GB, FIE,FIA,NUI,NUE,NIW,NEW,EPHY,Z,JT,VOLT,SAUG
     1,NL, SLPI,FLXI
      GO TO 30
  400 WRITE(6,350) NL
      GO TO 30
  200 FORMAT(5F10.0)
  300 FORMAT(15H1GAS PROPERTIES///1X,32HTE TSUR NENF DIO DEO ALFA DEL EP
     1//1X,1P8E13.5///)
  385 FORMAT(14H0NUA CONVERGES/9H0NTIME = ,I4,2X, 4HX = , F14.6,2X, 4HZ
     1= , F14.6, 2X, 6HNUA = , 1PE16.6,2X,6HNUX = , 1PE16.6////)
  320 FORMAT(126H0ITER     WB               TB               A               B
     1               T               W               W-PRIME          W-INTEG
     2RAL      ///)
  305 FORMAT(1X, I4, 1P8E15.7/)
  307 FORMAT(11H0150 RETURN//1X, I4, 1P8E15.7/1X, 1P3E18.7 )
  310 FORMAT(19H0SOLUTION CONVERGES//1X, I3, 1PE16.7, 1P7E15.7/5H0F = ,
     11PE16.7////)
  315 FORMAT(23H0APPROXIMATE F SOLUTION//1X, I3, 1PE16.7, 1P7E15.7/6H0TR
     1 = , 1PE15.7,5X, 4HF = , 1PE16.7////)
  390 FORMAT(24H0SHEATH-SURFACE SOLUTION//1X, 5HHB = , 1PE15.7, 2X, 5HGB
     1 = , 1PE15.7, 2X, 6HFIE = , 0PF8.4, 2X, 6HFIA = , F8.4, 2X, 6HNUI
     2= , 1PE14.6,2X, 6HNUE = , 1PE14.6/11H0NI-WALL = , 1PE14.6, 2X, 10H
     3NE-WALL = , 1PE14.6, 2X, 7HEPHY = , 1PE14.6/12H0COVERAGE = , 0PF14
     4.6,2X, 5HJT = , 1PE14.6,2X, 7HVOLT = , 1PE14.6,2X, 8HS-AUG = , 1PE
     514.6/6H0NL = ,1PE14.6,2X, 10HSLOPE-I = , 1PE14.6,2X,7HFLXI = ,1PE1
     64.6/////)
  350 FORMAT(6H0NL = ,1PE13.5///)
  360 FORMAT(7H0ARG = ,1PE13.5//)
  370 FORMAT(8H0FLXI = ,1PE13.5//)
       END
```

APPENDIX D

Potassium Boiler Procedures

Early in the experimental testing program, a black contaminate sporadically appeared on the cathode surfaces and inside and about the potassium boiler outlet tube which stopped the seed flow at times. The contaminate looked like black tar, but was a very hard substance like bakelite. The contaminate rapidly changed to a brown liquid with the addition of water. A contaminate with the above properties was reproduced by the following experiment on a piece of pure potassium metal.

A small lump ($\frac{1}{2}$ inch diameter) of potassium was placed on a metal plate which was heated from below. At first, the potassium melted and formed a smooth ball (like a piece of mercury) with a whitish, discolored surface. Upon further heating, a critical temperature was reached at which the potassium ball underwent a sudden transition; the surface of the potassium ball became very shiny (like a mirror), then the ball spread to all edges of the plate to form a thin layer. Even with no further heating, a reddish glow appeared at the center portion of the layer and spread to the edges. A black, sooty smoke left the region that was glowing. At the end of the transformation, the black contaminate covered the plate. The transition temperature was approximately determined (by a thermocouple) as $660^{\circ}K$. The above phenomena were independent of the plate material (brass, steel, or copper) or whether the potassium lump was initially rinsed in mineral oil or petroleum ether.

The revised potassium boiler procedure was to initially heat up the boiler to a temperature below the transition temperature of 660°K. Then the boiler was purged for one hour with the secondary flow of argon. Finally, the boiler was heated up to the normal operating temperature just prior to the experimental run. This procedure eliminated the formation of the black contaminate.